UNIVERSITÀ DEGLI STUDI DI MILANO

FACOLTÀ DI SCIENZE E TECNOLOGIE

Corso di Laurea Magistrale in Fisica

Sensitivity to ^{7}Be, *pep* and CNO solar neutrinos detection with the JUNO experiment

Relatore interno:
Dr. Alessandra Carlotta Re

Relatore esterno:
Prof. Dr. Livia Ludhova

Correlatore:
Dr. Davide Basilico

Elaborato di:
Anita Meraviglia
Matr. 955087
Codice P.A.C.S.:26.65.+t

Anno Accademico 2020-2021

Contents

Introduction **i**

1 Neutrino Physics **1**

1.1 Neutrinos in the Standard Model 1

1.2 Neutrino oscillation 3

1.2.1 The matter effect 8

1.3 Neutrino sources 10

1.4 The Standard Solar Model 13

1.4.1 The Solar Metallicity Problem 14

1.5 Processes powering the Sun 14

1.5.1 pp chain 16

1.5.2 CNO cycle 17

1.5.3 Solar neutrino fluxes 18

1.6 Solar neutrino experiments 19

1.6.1 The Solar Neutrino Problem and its solution 21

1.6.2 The Borexino experiment 23

2 The JUNO experiment **27**

2.1 JUNO physics goals 28

2.2 The detector design 31

2.2.1 Water Cherenkov Detector and Top Tracker 32

2.2.2 PMTs system 33

2.2.3 Central Detector 35

2.2.4 Liquid scintillator 35

2.3 The energy and position reconstruction 37

2.4 Background and methodology for its control 38

3 Solar neutrino signal and backgrounds 41

3.1 Solar neutrino signal 41

3.2 Intermediate energy solar neutrino backgrounds 42

3.2.1 Internal backgrounds 43

3.2.2 External backgrounds 48

3.2.3 Cosmogenic backgrounds 48

3.2.4 Background from reactor antineutrinos 51

3.2.5 Background from pileup events 52

4 Analysis strategy for ^{7}Be, *pep* and CNO solar neutrinos detection 53

4.1 Strategy steps 53

4.2 Monte Carlo simulation and events reconstruction framework 55

4.3 Monte Carlo campaign and PDF production 57

4.4 PDF smoothing 58

4.5 Toy dataset generation 58

4.6 Spectral fit: MUST and JUST 61

4.6.1 Fitting approach 61

5 Software tools for solar neutrinos analysis and sensitivity 65

5.1 JUST: a look under the hood 65

5.2 Validation procedure between MUST and JUST 67

5.2.1 Toy generator validation 67

5.2.2 Fitter validation 68

6 Results on ^{7}Be, *pep* and CNO neutrinos sensitivity 73

6.1 Standard fit configuration 73

6.2 Sensitivity results on ^{7}Be neutrinos 74

6.2.1 Impact of the exposure on ^{7}Be-ν sensitivity 74

6.2.2 Impact of ^{85}Kr background on ^{7}Be-ν sensitivity 77

6.2.3 Impact of ^{210}Po background on ^{7}Be-ν sensitivity 77
6.2.4 Impact of out-of-equilibrium ^{226}Ra background on ^{7}Be-ν sensitivity 78
6.3 Sensitivity results on *pep* neutrinos 79
6.3.1 Impact of the exposure on *pep*-ν sensitivity 80
6.3.2 Impact of a ^{210}Bi constraint on *pep*-ν sensitivity 82
6.3.3 Impact of ^{11}C background on *pep*-ν sensitivity 83
6.4 Sensitivity results on CNO neutrinos 85
6.4.1 Impact of the exposure on CNO-ν sensitivity 85
6.4.2 Impact of ^{11}C background on CNO-ν sensitivity 86
6.4.3 Impact of a *pep*-ν constraint on CNO-ν sensitivity 86
6.4.4 Sensitivity results on ^{15}O and ^{13}N neutrinos 86

Conclusions 93

Appendices 95

A JUST: Jülich nUsol Sensitivity Tool 97
A.1 JUST architecture 97
A.2 How to install and run JUST 99
A.3 Configuration files 100
A.3.1 `gen_opt.cfg` 101
A.3.2 `species_list.dat` 102
A.3.3 `toy_rates.dat` 104
A.4 JUST modules 106
A.4.1 Parser 106
A.4.2 DataReader 107
A.4.3 ToyDataGenerator 108
A.4.4 Fitter 109
A.4.5 FitResults 112
A.4.6 OutputManager 112

Introduction

Elementary particle physics and astrophysics have always been deeply connected to each other. Many discoveries of the intimate structure of matter broadened our understanding about the history of our Universe and the astrophysical objects it is composed of. At the same time, the study of stars, galaxies and of the large scale structure of the Universe provided us priceless clues to glean new properties of fundamental particles.

Within this framework, the study of neutrinos is a typical case and plays a primary role. Neutrinos are weakly interacting particles with a very small mass, constantly produced in processes involving radioactive decays.

The discovery of neutrino oscillations, the first experimental evidence that an extension of the Standard Model is needed, has been obtained through the detection of neutrinos coming from the atmosphere and the Sun. On the other side, the neutrino elusiveness make them attractive as regards astrophysics. Indeed, thanks to their tiny cross-section, neutrinos travel the cosmos almost undisturbed, carrying precious information on the astrophysical sources responsible for their production, included our own Earth and Sun.

Our Sun supplies the largest known flux of neutrinos at the Earth's surface. Every second approximately a hundred billion solar neutrinos cross every square centimeter on Earth. Solar neutrinos are produced in the fusion reactions occurring in the core of the Sun and represent the only direct probe of the deep interior of our nearest star. These nuclear reactions, which are responsible for the stellar energy production, are divided into two distinct sequences: the proton-proton (*pp*) fusion chain and the carbon-nitrogen-oxygen (CNO) cycle. The contribution from each of these processes depends *inter alia* on the mass, temperature and age of the star. Nowadays, in the Sun, the largest amount of the energy is produced by the *pp*-chain ($\approx$ 99 %), while the CNO cycle accounts for the remaining contribution ($\approx$ 1 %).

From the Seventies, solar neutrino experiments have proved to be sensitive to test both astrophysical and elementary particle physics models. Large detectors, typically hundreds or thousands of tons of active masses, are necessary to observe solar neutrinos. These detectors must be placed deep underground to avoid background interactions of cosmic rays that mimic the rare neutrino-induced events.

So far, solar neutrino experiments succeeded in detecting all types of neutrinos produced in the *pp*-chain (except for the very rare *hep* neutrinos) and only recently even those from the CNO cycle. Nonetheless, many open questions still exist. The so-called *solar metallicity problem*, which addresses the tension related to the abundance of metals in the core of Sun, represents an intriguing puzzle. Since the CNO cycle is catalyzed by elements heavier than helium, the corresponding neutrino flux is very sensitive to the chemical composition of the Sun's interior. Therefore, an accurate measurement of it would be helpful in shedding some light about this topic. Furthermore, up to now, only the sum of the fluxes of neutrinos produced in the CNO cycle has been measured. Nevertheless, assessing the single neutrino contributions would be groundbreaking for the evaluation of the nitrogen and oxygen amounts in the core of the Sun.

In the current astroparticle physics landascape, JUNO is an excellent candidate to address these questions. The Jiangmen Underground Neutrino Observatory (JUNO) is a multi-kton liquid scintillator detector under construction in China, which will be completed in 2023. Thanks to its large active mass and its unprecedented energy resolution, JUNO will have a unique potential to perform a real-time solar neutrinos spectroscopy.

My thesis work has been carried out within the JUNO collaboration, spending a six months traineeship period at Forschungzentrum Jülich (Germany) as an Erasmus+ student. This thesis is devoted to sensitivity studies to the so-called *intermediate energy solar neutrinos* (^{7}Be-ν, *pep*-ν and CNO-ν) fluxes.
The thesis layout is the following:

- Chapter 1: review of the main features of neutrino physics, focusing on solar neutrinos and on solar neutrino experiments.
- Chapter 2: summary of JUNO detector design and description of its experimental physics goals.
- Chapter 3: sketch of the solar neutrinos detection in JUNO and report of the possible background levels scenarios.
- Chapter 4: detailed portrait about the strategy of the analysis I have performed.
- Chapter 5: description of the validation procedure I have carried out between MUST and JUST, the two software tools developed for solar neutrino analysis.
- Chapter 6: presentation of my studies on the ^{7}Be-ν, *pep*-ν and CNO-ν fluxes sensitivity, with a focus on the impact of possible background levels.
- Appendix A: detailed description of JUST, a software tool for the solar neutrino analysis I have contributed to develop during the time I spent in Jülich.

CHAPTER 1

Neutrino Physics

1.1 Neutrinos in the Standard Model

The original idea of including a neutral and low-mass elementary particle - the *neutrino* - comes from a letter of W. Pauli during a physics conference at Tübingen in 1930. The introduction of this new particle could solve some anomalies observed in the studies of the continuous β spectrum of the neutron decay [1].

Neutrinos played a crucial role in the first theory of nuclear β decay proposed by E. Fermi in 1934 [2], who also suggested the term *neutrino* after the discovery of the neutron by J. Chadwick [3]. According to his theory, β decays were described as point-like interactions between four particles: a proton, a neutron, an electron and a neutrino.

From the second half of the XX century, neutrinos have been included in the Standard Model (SM) of particle physics, our current best understanding of how elementary particles and three of the fundamental interactions (strong, electromagnetic and weak) are related to each other. The Standard Model is a gauge theory based on the gauge group:

$$SU(3)_C \times SU(2)_L \times U(1)_Y \tag{1.1}$$

where $SU(3)_C$ is the group underlying the Quantum Chromodynamics (QCD) theory, describing the strong interactions, while $SU(2)_L \times U(1)_Y$ is the one being the basis of the Glashow-Weinberg-Salam theory of electroweak interactions. Since the weak interactions only involve the left-handed quantum fields, the Standard Model is a chiral theory.

In the Standard Model particles are firstly classified according to their spin: fermions, spin-1/2 particles, which are the fundamental components of ordinary matter, and bosons, spin-1 particles, called force carriers since they mediate the interactions.

A further classification divides the fermions into two categories: six quarks (up, down, charm, strange, top, bottom) and six leptons (electron, muon, tau and their respective neutrinos). In contrast to leptons which are only affected by the elec-

troweak sector, quarks have in addition a color charge, so that they are involved also in the strong interactions. Concerning bosons, the strong interactions are mediated by eight massless gluons, the weak interactions by three massive bosons (W^+ and W^- in *charged current* (CC) interactions and Z^0 in *neutral current* (NC) interactions) and the electromagnetic interactions by one massless photon.
The Higgs boson plays a special role. It is responsible for the bosons mass generation: without it, all the bosons would be massless. Also the fermions take advantage of the Higgs field to acquire mass thanks to the Yukawa mechanism. A summary of the Standard Model of particle physics is depicted in Fig. 1.1.

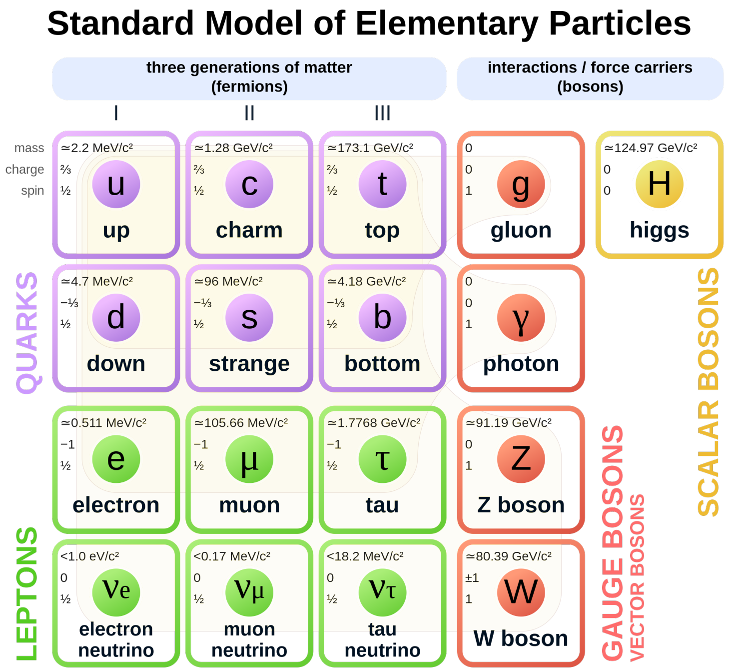

Figure 1.1: The Standard Model particles and their properties.

In this theoretical picture neutrinos are neutral and massless particles, included with their three flavors representations (ν_e, ν_μ, ν_τ and their corresponding antiparticles). The flavor of a neutrino is defined as the one of the charged lepton it couples with in a CC interaction (e, μ, τ)
Neutrinos interact only through the weak interaction, via the exchange of the W and Z bosons. The lagrangian of the CC term has the form:

$$\mathcal{L}_{CC} = -\frac{g}{2\sqrt{2}} \sum_{\ell=e,\mu,\tau} \overline{\nu}_\ell \gamma^\mu (1-\gamma^5)\ell W_\mu + h.c. \tag{1.2}$$

where g is the constant determining the strength of the coupling, γ^μ are the 4×4 Dirac matrices, γ^5 is the product of the four γ^μ and the W_μ fields represent the charged massive bosons. This interaction transforms the charged leptons ℓ into

neutrinos of the same flavor ν_ℓ and vice versa.
Concerning the NC term, the lagrangian is expressed as follow:

$$\mathcal{L}_{NC} = -\frac{g}{4\cos\theta_W}\sum_{\ell=e,\mu,\tau}\{\overline{\nu}_\ell\gamma^\mu(1-\gamma^5)\nu_\ell - (1-2\sin^2\theta_W)\overline{\ell}\gamma^\mu(1-\gamma^5)\ell + \\ + 2\sin^2\theta_W\overline{\ell}\gamma^\mu(1+\gamma^5)\ell\}Z_\mu + h.c. \tag{1.3}$$

where θ_W is the weak mixing angle and Z_μ the fields associated to the neutral charged boson. These two kind of processes - CC and NC - are schematically reported in terms of Feynman diagrams in Fig. 1.2

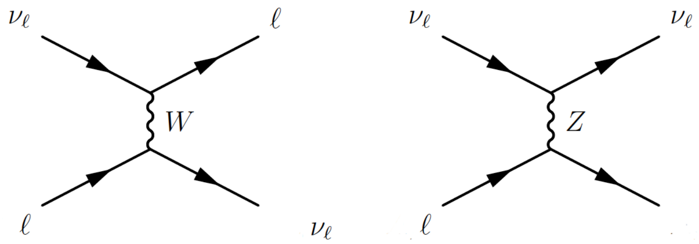

Figure 1.2: Feynman diagrams for ν_ℓ neutrino interactions with a generic lepton ℓ. Left: charged current (CC) interactions. Right: neutral current (NC) interactions.

Despite SM is a self-consistent theoretical framework describing many physical phenomena experimentally confirmed through the years, it is far from being complete and satisfying by itself. For example, every attempt to include the gravitational interaction, as described by general relativity, has failed as well as the prediction of any cold dark matter candidate. Furthermore, the introduction of a non-zero neutrino mass, crucial if neutrinos do oscillate, requires an extension of the SM.

1.2 Neutrino oscillation

By *neutrino oscillation* we mean the quantum mechanical phenomenon in which a neutrino created with a specific lepton flavor can be later measured with a different flavor. Neutrinos are only produced in weak interactions, namely in a flavor eigenstate and they have a nonzero probability to be found with a different flavor after traveling for a certain distance.

This mechanism was first suggested by B. Pontecorvo in 1957 [4] and takes place only if neutrinos have different masses. Its experimental confirmation is relatively recent (see Section 1.6) and its description needs an extension of the SM due to the non-zero neutrino mass.

If neutrinos are massive, the states of definite flavor (ν_e, ν_μ, ν_τ) may not coincide with states of definite mass (ν_1, ν_2, ν_3). The produced neutrino is therefore a superposition of different mass eigenstates: as the neutrino beam propagates, its components evolves in flight as free quantum states independently and differently from each other. By doing so, the probability of finding different flavor eigenstates in the same beam varies with distance.

In the following the expression of the oscillation probability [5] will be given firstly in the most general scenario and then in the specific case of the JUNO experiment. Finally, the relation for the two flavors neutrino approximation will be reported.
Let $|\nu_\alpha\rangle$ with $\alpha = e, \mu, \tau$ be the flavor eigenstate, while $|\nu_i\rangle$ with $i = 1, 2, 3$ the mass eigenstate. We have:

$$|\nu_\alpha\rangle = \sum_{i=1}^{3} U_{\alpha i} |\nu_i\rangle \tag{1.4}$$

where U is a 3×3 unitary matrix, analogous to the CKM matrix that describes the mixing between quarks. It is called *neutrino mixing matrix* or *Pontecorvo-Maki-Nakagawa-Sakata (PMNS) matrix* and it can be parametrized by combining three rotation matrixes and including a complex phase with a total of four independent parameters. A fourth matrix containing another two complex phases is added in order to taking into consideration our ignorance about Dirac or Majorana nature of neutrinos. Thus, the PMNS matrix is:

$$\begin{aligned} U = \begin{pmatrix} 1 & 0 & 0 \\ 0 & c_{23} & s_{23} \\ 0 & -s_{23} & c_{23} \end{pmatrix} \cdot \begin{pmatrix} c_{13} & 0 & s_{13}e^{-i\delta_{CP}} \\ 0 & 1 & 0 \\ -s_{13}e^{i\delta_{CP}} & 0 & c_{13} \end{pmatrix} \cdot \begin{pmatrix} c_{12} & s_{12} & 0 \\ -s_{12} & c_{12} & 0 \\ 0 & 0 & 1 \end{pmatrix} \\ \cdot \begin{pmatrix} e^{i\eta_1} & 0 & 0 \\ 0 & e^{i\eta_2} & 0 \\ 0 & 0 & 1 \end{pmatrix} \end{aligned} \tag{1.5}$$

where $c_{ij} = \cos\theta_{ij}$ and $s_{ij} = \sin\theta_{ij}$. The matrix U has a total of six independent parameters: θ_{12}, θ_{13} and θ_{23} are the three mixing angles; δ_{CP} is the CP-violation phase which accounts for a possible violation of the CP symmetry by the weak interaction in the lepton sector; η_1 and η_2 are the two Majorana phases which have physical meaning only if the neutrino is a Majorana particle[1] and play no role in neutrino oscillations. By doing the product, U takes the following form:

$$U = \begin{pmatrix} c_{12}c_{13} & s_{12}c_{13} & s_{13}e^{-i\delta_{CP}} \\ -s_{12}c_{23} - c_{12}s_{23}s_{13}e^{i\delta_{CP}} & c_{12}c_{23} - s_{12}s_{23}s_{13}e^{i\delta_{CP}} & s_{23}c_{13} \\ s_{12}s_{23} - c_{12}c_{23}s_{13}e^{i\delta_{CP}} & -c_{12}s_{23} - s_{12}c_{23}s_{13}e^{i\delta_{CP}} & c_{23}s_{13} \end{pmatrix} \tag{1.6}$$

In the case of Dirac neutrinos, the matrix U is unitary, hence satisfies the requirements:

---

[1] A fermion is a *Majorana particle* if it coincides with its own antiparticle.

$$U^\dagger U = \mathbb{1} \qquad \text{or} \qquad U^\dagger = U^{-1} = (U^*)^T \tag{1.7}$$

We can write the flavor α of a neutrino produced at the source $x_0 = (\mathbf{x}, t) = (0, 0)$ as a linear combination of the mass eigenstates:

$$|\nu_\alpha(0)\rangle = \sum_k U_{\alpha k} |\nu_k(0)\rangle \tag{1.8}$$

where U is the unitary mixing matrix expressed in equation 1.6.
The mass eigenstates propagate according to the "free-particle" Schrödinger equation:

$$i\frac{\partial}{\partial t} |\nu_k(x)\rangle = -\frac{1}{2m_k}\frac{\partial^2}{\partial x^2} |\nu_k(x)\rangle \tag{1.9}$$

The solution of this equation is a plane-wave function:

$$|\nu_k(x)\rangle = e^{-i(E_k t - \mathbf{p}_k \cdot \mathbf{x})} |\nu_k(0)\rangle = e^{-i\phi_k} |\nu_k(0)\rangle \tag{1.10}$$

where we define the phase ϕ_k as $\phi_k = p_k x$, with $p_k = (E_k, \mathbf{p}_k)$ the 4th-momentum of the neutrino mass state ν_k and $x = (t, \mathbf{x})$ the spacetime 4th-vector.

The temporal evolution of the initial state with flavor α is given by:

$$|\nu_\alpha(x)\rangle = \sum_k U_{\alpha k} |\nu_k(x)\rangle = \sum_k U_{\alpha k} e^{-i\phi_k} |\nu_k(0)\rangle \tag{1.11}$$

By inverting equation 1.8, we obtain the mass eigenstates as a linear combination of the flavor eigenstates:

$$|\nu_k(0)\rangle = \sum_\alpha U^*_{\alpha k} |\nu_\alpha(0)\rangle \tag{1.12}$$

By using equation 1.12, we can rewrite equation 1.11 by expressing the flavor state α at a spacetime point x in terms of the flavor eigenstates at the source:

$$|\nu_\alpha(x)\rangle = \sum_\gamma \sum_k U_{\alpha k} e^{-i\phi_k} U^*_{\gamma k} |\nu_\gamma(0)\rangle \tag{1.13}$$

We can finally write the transition amplitude $\mathcal{A}$ for the detection of a neutrino of flavor β at a distance L from the source, where a neutrino of flavor α was originally produced:

$$\mathcal{A}(\nu_\alpha(0) \to \nu_\beta(L)) = \langle \nu_\beta(L) \,|\, \nu_\alpha(0) \rangle = \sum_\gamma \sum_k U^*_{\beta k} e^{i\phi_k} U_{\gamma k} \langle \nu_\gamma(0) \,|\, \nu_\alpha(0) \rangle = \sum_k U^*_{\beta k} e^{i\phi_k} U_{\alpha k} \tag{1.14}$$

where we used the orthogonality of the flavor states $\langle \nu_\gamma(0) \,|\, \nu_\alpha(0) \rangle = \delta_{\gamma\alpha}$, where $\delta_{\gamma\alpha}$ is the Kronecker delta function, and the fact that the neutrinos can be considered as very relativistic particles, so that $t \simeq L$, assuming from now on $\hbar = c = 1$.

The oscillation probability is given by:

$$P(\nu_\alpha \to \nu_\beta) = |\mathcal{A}(\nu_\alpha(0) \to \nu_\beta(L))|^2 = \left|\sum_{k=1}^{3} U^*_{\beta k} e^{i\phi_k} U_{\alpha k}\right|^2 \tag{1.15}$$

Since neutrinos are relativistic particles, we can make the approximation $E_k, p_k \gg m_k$ so that the energy can be rewritten as:

$$E_k = \sqrt{p_k^2 + m_k^2} = p_k \sqrt{1 + \frac{m_k^2}{p_k^2}} \approx p_k \left(1 + \frac{m_k^2}{2p_k^2}\right) \approx p_k + \frac{m_k^2}{2E_k} \tag{1.16}$$

Now we can rewrite the phase ϕ_k by using eq. 1.16 and assuming $t \simeq x \simeq L$:

$$\phi_k = E_k t - p_k x \approx p_k L + \frac{m_k^2}{2E_k} L - p_k L = \frac{m_k^2}{2E_k} L \tag{1.17}$$

Taking advantage of the complex relation $|z_1 + z_2 + z_3|^2 = |z_1|^2 + |z_2|^2 + |z_3|^2 + 2\Re(z_1 z_2^* + z_1 z_3^* + z_2 z_3^*)$ and using eq. 1.17, we can manipulate eq. 1.15 to obtain the general expression of the oscillation probability for a neutrino of flavor α to be detected as a neutrino of flavor β after traveling a distance L:

$$P(\nu_\alpha \to \nu_\beta) = \delta_{\alpha\beta} - 4\sum_{k>j} \Re(U^*_{\alpha k} U_{\beta k} U_{\alpha j} U^*_{\beta j}) \sin^2(\Delta_{kj}) + 2\sum_{k>j} \Im(U^*_{\alpha k} U_{\beta k} U_{\alpha j} U^*_{\beta j}) \sin(2\Delta_{kj}) \tag{1.18}$$

where the argument of the trigonometric functions is:

$$\Delta_{kj} = \Delta m^2_{kj} \frac{L}{4E} = 1.27 \Delta m^2_{kj} \frac{L[\mathrm{m}]}{E[\mathrm{MeV}]} \qquad \text{for} \qquad k > j \tag{1.19}$$

The probability in eq. 1.18 depends on the mass-squared differences $\Delta m^2_{kj} = m_k^2 - m_j^2$, with $k > j$, which drive the oscillatory terms, the mixing angles θ_{jk}, hidden in the matrix elements, responsible for the amplitude of the oscillations, the phase δ_{CP} and the ratio L/E between the propagation distance (called *baseline*) and the neutrino energy. While the latter is determined by the experimental setup, the other parameters require an experimental measurement.

Experiments about neutrino oscillations can be divided into two categories: *appearance* and *disappearance* experiments. The former study the appearance of neutrinos of flavor β starting from a beam of α flavor neutrinos, thus measuring the probability in eq. 1.18 with $\beta \neq \alpha$. On the other hand, the latter, starting with a beam of α flavor neutrinos, study how many of them disappeared after traveling a distance L. Therefore, the disappearance experiments measure the probability in eq. 1.18 with $\alpha = \beta$, i.e. $P(\nu_\alpha \to \nu_\alpha)$, also called *survival probability*.

According to this classification, JUNO is a disappearance experiment: as I will describe more in detail in Chapter 2, the JUNO main goal is the spectroscopy of electron antineutrinos produced in nuclear reactors. Since we are interested in neutrinos of electronic flavor, $\alpha = \beta = e$, starting from eq. 1.18, we obtain:

$$\begin{aligned} P(\nu_e \to \nu_e) = 1 &- \cos^4(\theta_{13}) \sin^2(2\theta_{12}) \sin^2(\Delta_{21}) \\ &- \cos^2(\theta_{12}) \sin^2(2\theta_{13}) \sin^2(\Delta_{32}) \\ &- \sin^2(\theta_{12}) \sin^2(2\theta_{13}) \sin^2(\Delta_{32}) \end{aligned} \tag{1.20}$$

where Δ_{kj} are defined in eq. 1.19.

Finally, assuming the CPT invariance, we have $P(\overline{\nu}_e \to \overline{\nu}_e) = P(\nu_e \to \nu_e)$: so eq. 1.20 represents the survival probability for an electron antineutrino to be detected as an electron antineutrino at a distance L from the source. This formula is valid in disappearance experiments, like the JUNO experiment.

For convenience, we also report here a useful simplification concerning the calculation of the oscillation probability, called *two-neutrino scheme*. In fact, for a given L/E regime range, we can safely assume that the experimental setup is sensitive only to a sub-section of the U matrix only. According to this approximation, only two massive neutrinos and two flavor eigenstates can be considered. Thus, the mixing matrix U can be reduced to a 2×2 matrix, depending only on one free parameter, the mixing angle θ:

$$U^{2\nu} = \begin{pmatrix} \cos\theta & -\sin\theta \\ \sin\theta & \cos\theta \end{pmatrix} \tag{1.21}$$

The flavor transition probability is simply calculated as:

$$P^{2\nu}(\nu_\alpha \to \nu_\beta) = \sin^2(2\theta) \sin^2\left(\Delta m^2 \frac{L}{4E}\right) \tag{1.22}$$

where $\Delta m^2 = m_\beta^2 - m_\alpha^2$.

Currently, the value of the three mixing angles and the two square-mass differences have been measured with reasonable precision (see Table 1.1). Only two out of the three Δm_{kj}^2 are measured because only two of them are independent: in fact, they have to satisfy the relation $\Delta m_{21}^2 + \Delta m_{32}^2 + \Delta m_{13}^2 = 0$. From experiments studying neutrino oscillations, we know that $\Delta m_{21}^2 > 0$, while the sign of $\Delta m_{32/31}^2$ is still unknown. Consequently, there are two possible orderings for the spectrum of neutrino masses, shown in Fig. 1.3: *normal ordering* (NO) where $m_1 < m_2 < m_3$ and *inverted ordering* (IO) where $m_3 < m_1 < m_2$. The determination of the correct MO is one of the current open issues in neutrino physics.

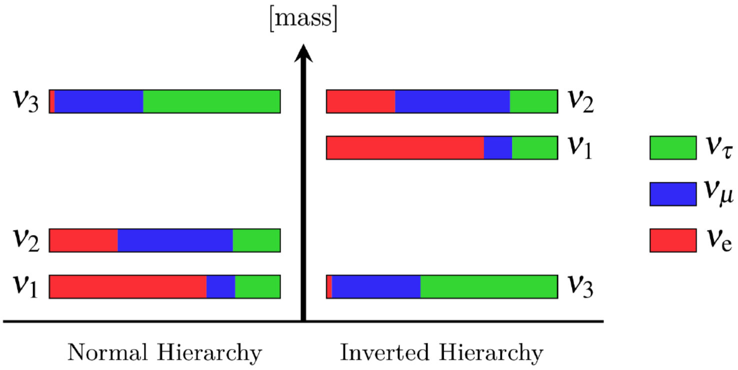

Figure 1.3: Illustration of mass spectra compatible with the data from neutrino oscillations. Left: normal hierarchy. Right: inverted hierarchy. The length of the colored bars is proportional to the flavor content of each mass state [6].

Parameter	Normal Ordering	Inverted Ordering
$\sin^2\theta_{12}$	$(3.10^{+0.13}_{-0.12})\cdot 10^{-1}$	
$\sin^2\theta_{23}$	$(5.58^{+0.20}_{-0.33})\cdot 10^{-1}$	$(5.63^{+0.19}_{-0.26})\cdot 10^{-1}$
$\sin^2\theta_{13}$	$(2.241^{+0.066}_{-0.065})\cdot 10^{-2}$	$(2.261^{+0.067}_{-0.064})\cdot 10^{-2}$
Δm^2_{21} [eV^2]	$(7.39^{+0.21}_{-0.20})\cdot 10^{-5}$	
Δm^2_{32} [eV^2]	$(2.449^{+0.032}_{-0.030})\cdot 10^{-3}$	$(-2.509^{+0.032}_{-0.032})\cdot 10^{-3}$

Table 1.1: This table summarizes the best-fit values of neutrino oscillation parameters. The results are taken from a global analysis of neutrino data, w/o SK-ATM [7]. Results are given both assuming normal and inverted ordering.

1.2.1 The matter effect

Until now, we have considered only neutrino oscillations in the vacuum. The oscillation probability change if neutrinos travel through matter and they interact differently according to their flavor eigenstate. This phenomenon is called *matter effect* and it depends on the energy of the traveling neutrino and the electron density of the traversed matter. When neutrinos travel through a dense medium (e.g. in the Sun or in the Earth), their propagation can be significantly modified by the coherent forward scattering by particles they encounter along the way. The matter effect stems from the fact that electron neutrinos (and antineutrinos) have different interactions with matter compared to other neutrinos flavors. In particular, ν_e can have both charged and neutral current elastic scattering with electrons, while ν_μ and ν_τ have only neutral current interactions with electrons.

In 1985, Mikheyev and Smirnov found out a very relevant feature of oscillation in matter: under particular conditions, the matter effect can lead to a resonant flavor transition. This mechanism is known as *Mikheyev-Smirnov-Wolfenstein (MSW)* *effect* and it is crucial to explain the solar neutrino flavor oscillation [8].

We will now describe the matter effect in the framework of oscillations between two families. The net effect of matter is the introduction of an extra-potential energy term for electron neutrinos:

$$V_e = \pm\sqrt{2}G_F N_e \tag{1.23}$$

where G_F is the Fermi constant, N_e the matter electron density and the positive (negative) sign applies to electron neutrinos (antineutrinos).
Therefore, the effective hamiltonian H_{eff}, which drives the neutrinos interaction in matter, is given by:

$$H_{\text{eff}} = H_{\text{vac}} + H_{\text{mat}} \tag{1.24}$$

where

$$H_{\text{vac}} = \frac{\Delta m^2}{4E}\begin{pmatrix} -\cos 2\theta & \sin 2\theta \\ \sin 2\theta & \cos 2\theta \end{pmatrix} \tag{1.25}$$

and

$$H_{\text{mat}} = \begin{pmatrix} V_e & 0 \\ 0 & 0 \end{pmatrix} \tag{1.26}$$

We can subtract from eq. 1.24 the following term:

$$\begin{pmatrix} V_e/2 & 0 \\ 0 & V_e/2 \end{pmatrix} \tag{1.27}$$

Therefore we obtain:

$$H_{\text{eff}} = \frac{\Delta m^2}{4E}\begin{pmatrix} -2\cos 2\theta + A & \sin 2\theta \\ \sin 2\theta & \cos 2\theta - A \end{pmatrix} \tag{1.28}$$

being E the neutrino energy and

$$A = \pm\frac{2\sqrt{2}G_F N_e E}{\Delta m^2} \tag{1.29}$$

If the matter density is constant, we diagonalise again H_{eff} to obtain the mixing matrix and the mass eigenstates in matter. By denoting with θ_m the effective mixing angle in matter and with Δm^2_m the effective difference of squared masses, we can write the effective hamiltonian using the same form as the vacuum one:

$$H_{\text{eff}} = \frac{\Delta m^2_m}{4E}\begin{pmatrix} -\cos 2\theta_m & \sin 2\theta_m \\ \sin 2\theta_m & \cos 2\theta_m \end{pmatrix} \tag{1.30}$$

which leads to the usual analytical dependence of the oscillation probability:

$$P_m^{2\nu}(\nu_\alpha \rightarrow \nu_\beta) = \sin^2(2\theta_m)\sin^2\left(\Delta m_m^2 \frac{L}{4E}\right) \tag{1.31}$$

By equaling eq. 1.28 and eq. 1.30, we can derive the expression for the effective mixing parameters in matter:

$$\Delta m_m^2 = \Delta m^2 \sqrt{(\cos 2\theta - A)^2 + \sin^2 2\theta} \qquad \sin 2\theta_m = \frac{\sin 2\theta}{\sqrt{(\cos 2\theta - A)^2 + \sin^2 2\theta}} \tag{1.32}$$

These formulas highlight the following important consequences of the matter effect:

- If $\sin 2\theta = 0$ then $\sin 2\theta_m = 0$, regardless of the potential. In order to have oscillations in matter, it is necessary to have the possibility of vacuum oscillations.
- If the matter is extremely dense, i.e. $N_E \rightarrow \infty$, then $\sin 2\theta_m = 0$: in very dense matter, oscillations cannot occur via matter effects.
- Under the resonant condition $\cos 2\theta = A$, oscillations can be significantly enhanced, no matter what the value of θ is.
- The resonant condition occurs if $A > 0$, which in turn depends on the sign of Δm^2. This dependence can be used to determine the neutrino mass hierarchy.
- Oscillation probabilities for neutrino and antineutrino can be different due to matter effects. Therefore this effect introduces an asymmetry between neutrinos and antineutrinos, called *fake CP violation*, simply due to the different interactions between ν and $\overline{\nu}$ with matter, that is composed by particles and not by antiparticles.

1.3 Neutrino sources

In our universe many different processes, both natural and anthropic, can lead to neutrinos production. Fig. 1.4 shows the neutrino fluxes from different sources as a function of their energy.

We can classify (anti-)neutrinos according to their production source. In order of growing energy there are:

- **Cosmological or relic neutrinos (μeV - meV)**: also known as *Cosmic Neutrino Background* (CNB), they represent the 1.9 K neutrino counterpart to the 2.7 K cosmic microwave background (CMB). While the latter disentangled from matter when the universe was about 379 000 years old, the CNB decoupled only 1 second after the Big Bang. Despite relic neutrinos represent the most

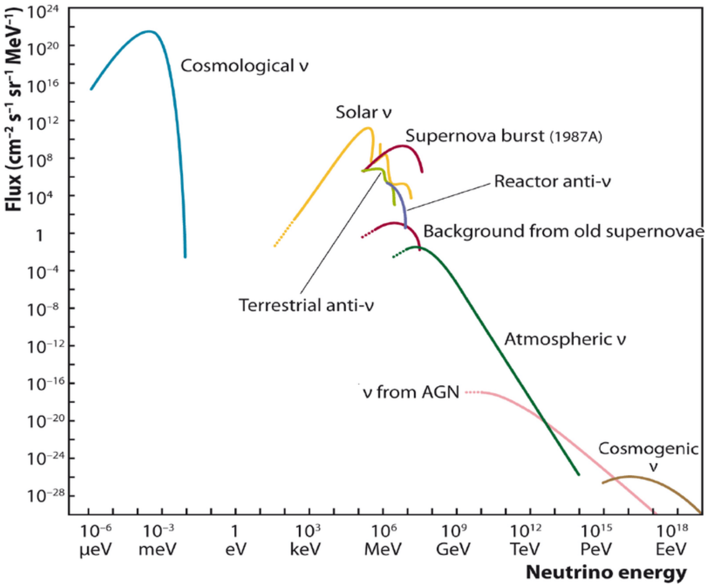

Figure 1.4: Neutrino and antineutrino fluxes from different sources as a function of their energy, in log-log scale [9].

abundant neutrino source, their extremely low energy makes them very difficult to detect. Due to it, they have not been measured so far, even if some proof of principles are going to catch on, like the PTOLEMY project [10].

- **Solar neutrinos (hundreds keV - MeV)**: stars are an important source of neutrinos. The nuclear reactions that take place in their core involve weak reactions which produce a large amount of neutrinos. In particular, neutrinos coming from the Sun offer a great opportunity to directly test the theory of stellar evolution and of nuclear energy generation. Since the goal of this thesis is precisely represented by solar neutrinos, I will describe them more in detail in the next sections.

- **Geo-neutrinos (MeV)**: they are electron antineutrinos ($\overline{\nu}_e$) produced in β decays of long-lived isotopes, which are naturally present in the interior of the Earth. Most of them originate from the β decays of ^{40}K and of isotopes of the ^{238}U and ^{232}Th chains.

- **Reactor neutrinos (MeV)**: nuclear reactors are the major human-generated antineutrino source. Antineutrinos are emitted in the β decays of neutron-rich daughter fragments in the fission processes from the ^{235}U, ^{239}Pu and ^{241}Pu chains [11, 12]. The produced neutrino flux covers the energy between 1 MeV and 10 MeV. On average, every fission cycle produces about 200 MeV of energy, of which roughly 4.5% is radiated away as antineutrinos. Hence, 1 GW thermal power corresponds to $\sim 2 \cdot 10^{20}\, \overline{\nu}_e/\mathrm{s}$.

  It was through reactors that neutrinos were detected for the first time in 1956, in the experiment designed by Cowan and Reines [13]. It exploited the inverse β decay reaction:

$$\overline{\nu}_e + p \rightarrow n + e^+ \tag{1.33}$$

Antineutrinos interact with protons of the water and gadolinium tank used as detector: the products are neutrons and positrons. After $\sim$ 10 μs from its emission, the neutron is captured by the gadolinium with the consequent production of a photon; the positron immediately annihilates with an electron, creating simultaneously two photons (eq. 1.34). Thanks to this double-signature, the background rejection is extremely powerful and allows a clear signal identification.

$$n + \text{Gd} \rightarrow \gamma \qquad e^+ + e^- \rightarrow \gamma + \gamma \tag{1.34}$$

- **Supernova neutrinos (MeV)**: a supernova is a rare astronomical event occurring during the last stellar evolutionary stages of a massive star life. Neutrinos are also an important product of Type Ib, Ic and II supernovae. When the nuclear reactions become insufficient to balance gravity, the stellar core collapses until matter density becomes extremely high ($\approx 10^{11} - 10^{15}$ g/cm^3). Also the cross section of electron capture of protons increases, leading to the production of a huge number of neutrons and electronic neutrinos. Furthermore, many neutrinos-antineutrinos pairs of all flavors are emitted by the residual neutron core. In fact, it dissipates its thermal energy ($10^{51} - 10^{53}$ erg) in about 10 seconds: $\sim$ 99% of it is emitted as a burst of neutrinos and the remaining $\sim$ 1% as photons.

- **Atmospheric neutrinos (GeV)**: they originate from the interaction of the cosmic ray flux with the Earth atmosphere. The collision between cosmic ray particles – mainly composed of protons and iron nuclei – and air molecules generates a cascade of secondary hadrons: kaons and especially pions. The dominant neutrino production mechanism is:

$$\pi^+ \rightarrow \nu_\mu + \mu^+ \qquad \mu^+ \rightarrow \overline{\nu}_\mu + e^+ + \nu_e \tag{1.35}$$

  and the energy of atmospheric neutrinos lies between 1 GeV and 100 GeV.

- **Accelerator neutrinos (GeV)**: neutrinos produced in accelerators are typically muon neutrinos and/or antineutrinos. To create the beam, it's common to start with protons, which are then accelerated close to the speed of light before they are smashed into a target, often made of beryllium or graphite. The collision creates new particles, kaons and pions. Particles of correct charge are selected and focused into a decay pipe where they decay into muons and muon neutrinos. After the decay pipe, an absorber removes the residual decay products while neutrinos proceed towards the detector. Neutrino beams can be used for two different kinds of experiments, distinguished by how far away the detectors are from where the neutrinos are created: *short-baseline* and *long-baseline experiments*. The different baseline allows them to investigate various range of neutrino oscillation parameters.

- **Galactic and extra-galactic high energy neutrinos ($>$ TeV)**: the highest energy neutrinos (in the energy range above 1 TeV) come from sources like supernova remnants, Gamma Ray Bursts, Active Galactic Nuclei or from interactions of ultra-energetic protons with the CMB. Their observation can provide insight into the long-standing problem of the origin and acceleration mechanisms of high-energy cosmic rays.

1.4 The Standard Solar Model

In this Section, I will briefly summarize the main concepts behind the formulation of the Standard Solar Model (SSM), necessary to better understand the solar neutrino production mechanisms. For more details see Ref. [14, 15, 16, 17, 18, 19].

This model is based on a set of equations, describing the stellar evolution and qualitatively summarised below:

- *Mass conservation*: the Sun is predicted to lose only $\sim 0.01\%$ of its initial mass during its expected main-sequence lifetime ($\sim 10^{10}$ y).
- *Energy conservation*: we can assume the conservation of energy between the energy released in the nuclear reactions, taking place in the core of the Sun, and the energy contributions used for the star expansion or contraction.
- *Hydrostatic equilibrium*: every layer of the star maintains a balance between the gravitational force and the pressure gradient resulting from nuclear fusion.
- *Energy transport*: in the innermost core of the Sun, energy is transported by radiation, while in the outermost regions by convection.
- *Solar composition*: initially the elements of the Sun were distributed homogeneously. Then, changes of elements abundance have occurred as a result of nuclear fusion reactions. Equivalence between solar core primordial abundances and contemporary surface abundances is assumed.

In addition, a set of experimentally measured boundary conditions are set: Sun current mass, age, radius and luminosity as well as the initial elemental abundances (the *metallicity*, see Section 1.4.1) and the nuclear reactions parameters. All these conditions are continuously updated to take into account the latest results of experimental observations.

By solving these equations with the appropriate boundary conditions, a dynamic model following the Sun evolution is given as output. Among the other quantities, the energy spectrum and fluxes of all the emitted neutrinos are given (see Section 1.5.3).

1.4.1 The Solar Metallicity Problem

The metallicity of the Sun, i.e. the abundance of elements heavier than He, is one of the most crucial parameters given in input to the SSM and it is inferred from the solar photospheric spectrum.

Historically, the adopted solar abundance was the one from the so-called *high metallicity* or *HZ* scenario, where the ratio between heavy elements and hydrogen abundance was $Z/X = 0.023$ (B16-GS98, [20]). Nevertheless, starting from 2001, new measurements of the elemental abundance of the Sun's surface suggested to reduce the amount of heavier elements, leading to a ratio of metal abundance equal to $Z/X = 0.0165$ (B16-AGSS09, [21]). This latter case is referred to the *low metallicity* or *LZ* scenario and it is about 33% lower than the previous case. As depicted in Section 1.5.3, by varying the input abundances the predictions of the neutrino fluxes change and their relevance depends on the neutrino source inside the Sun.

However, the so-called *solar metallicity problem* is due to the fact that, unfortunately, the LZ-SSM produces results in disagreement with helioseismology, the study of the propagation of acoustic pressure waves through the Sun. On the other hand, the Sun internal structure predicted by high metallicity models is in exceptional agreement with the helioseismology measurements.

Solar neutrinos are a priceless source of information helping us to relax this tension. In fact, the predicted solar neutrino fluxes depend on the metallicity input (see Section 1.5.3), especially for neutrinos from the CNO cycle reactions (see Section 1.5.2), for which the difference between the HZ and the LZ scenario is $\approx 28\%$, but also for ^{7}Be ($\approx 9\%$) and ^{8}B ($\approx 18\%$) neutrinos (see Section 1.5.1).

1.5 Processes powering the Sun

The Sun produces $\approx 3.8 \cdot 10^{26}$ W of luminosity thanks to two main branches of nuclear reactions taking place in its core [22]: the *pp* chain, which contributes for the $\approx$ 99% of its luminosity, and the CNO cycle, that involves carbon, nitrogen and oxygen and it is secondary in the Sun, providing only $\approx$ 1% of solar luminosity. The CNO cycle is more important in the energy balance of stars more massive − and so with a higher core temperature − than the Sun ($M > 1.5 M_\odot$). In fact, *pp* chain reactions start at temperatures around $4 \cdot 10^6$ K, while the CNO cycle needs higher temperatures. The physical reason behind this is that the Coulomb barrier for proton reactions with carbon and nitrogen is 6-7 times higher than for proton-proton reactions; therefore, the CNO cycle can only occur at relatively high temperatures, when additional thermal energy can increase the probability to penetrate the Coulomb barrier. The CNO cycle starts at approximately $1.5 \cdot 10^7$ K. Figure 1.5 shows the star luminosity in log scale as a function of the star core temperature. It is evident the supremacy of the *pp* chain for stars having a core temperature similar to the Sun one.

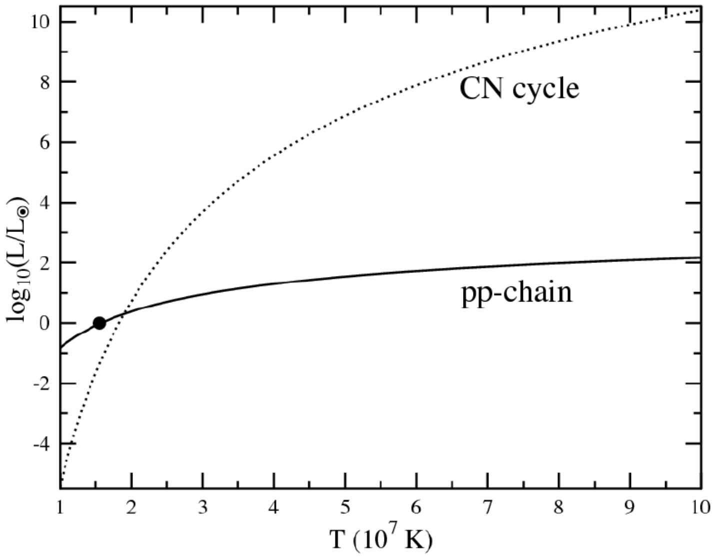

Figure 1.5: The star luminosity in log scale as a function of the core temperature for the *pp* chain (solid line) and the CNO cycle (dashed line) [23]. Luminosity is normalized to the *pp* chain energy production in the Sun central core $L_\odot$. The black dot refers to the Sun core: the predominance of *pp* chain with respect to CNO cycle is clear. The critical temperature equalizing the two mechanisms is $\approx 1.8 \cdot 10^7$ K.

The two mechanisms mentioned above share the net process, consisting in the conversion of four protons into a ^{4}He atom:

$$4p \rightarrow ^4\text{He} + 2e^+ + 2\nu_e + 26.731\,\text{MeV} \tag{1.36}$$

where two electron neutrinos are emitted. A sketch of these two mechanisms is given in Fig. 1.6, where the highlighted boxes contain the reactions in which solar neutrinos are emitted.

As better discussed in Sec. 1.5.1 and Sec. 1.5.2, electron neutrinos are produced in eight of the reactions occurring in the Sun (five in the *pp* chain and three in the CNO cycle). Solar neutrinos overall energy spectrum lies in the $0\,\text{MeV} < E_\nu < 18.8\,\text{MeV}$ range, depending on the involved nuclear reactions.

The very low neutrino cross section makes solar neutrinos an ideal tool to investigate the interior of the Sun. Considering a typical stellar density core of about 100 g/cm^3 and an average cross section of about $\langle\sigma\rangle \sim 10^{-43}\,\text{cm}^2$ at energy of 1 MeV, the ν_e mean free path is of the order of 10^{17} cm, which is much larger than the radius of the Sun. Thus, neutrinos are able to go through the solar matter almost undisturbed, reaching the Earth surface after eight minutes from their production

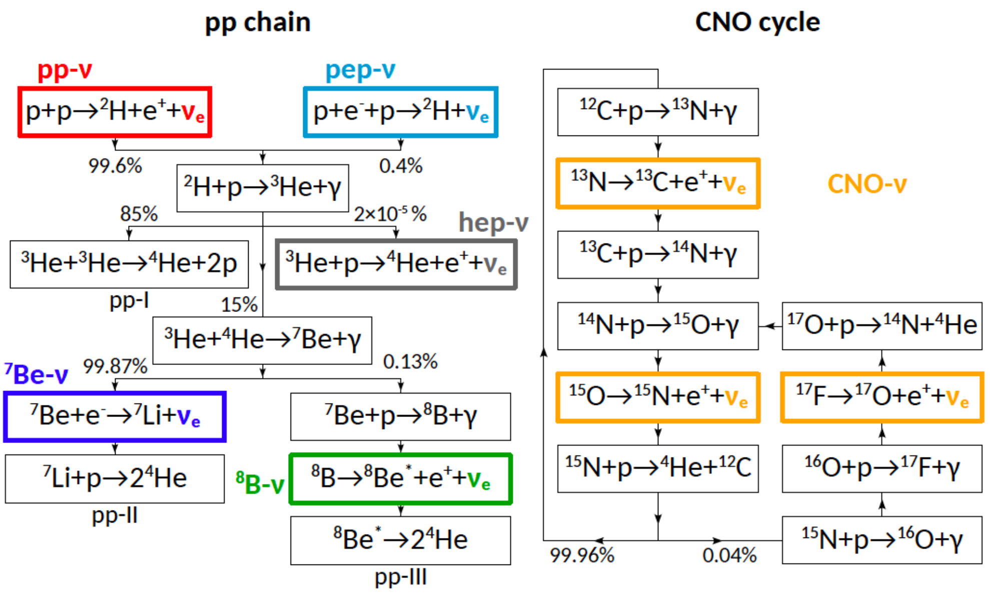

Figure 1.6: Scheme of the reactions from the pp chain (left) and CNO cycle (right).

in the solar core.

1.5.1 *pp* chain

The steps of the pp chain are schematically depicted in the left panel of Fig. 1.6. The first step of the pp chain is one of the following reactions, with the respective neutrinos' energies and branching ratios reported:

$$\textbf{pp}: \quad p+p \to {}^2\text{He}+e^+ +\nu_e \qquad Q = 0.42\,\text{MeV} \qquad B.R. = 99.77\% \tag{1.37a}$$

$$\textbf{pep}: \quad p+e^- +p \to {}^2\text{He}+\nu_e \qquad Q = 1.44\,\text{MeV} \qquad B.R. = 0.23\% \tag{1.37b}$$

The first step of the chain, being mediated by the weak force, is the slowest one of the process and it takes $\approx 1.4 \cdot 10^{10}$ y. The pp process is dominant and occurs 99.77% of times. pp neutrinos energy spectrum is continuum with an endpoint at about 0.42 MeV. On the other hand, the pep process, which gives birth to the 1.44 MeV monoenergetic pep neutrinos, is disfavored.
Regardless of the method by which the deuterium nucleus is formed, this will quickly capture a free proton:

$$^2\text{He}+p \to {}^3\text{He}+\gamma \qquad Q = 5.494\,\text{MeV} \tag{1.38}$$

This process, mediated by the strong force, is extremely fast ($\approx$ 6 s) if compared to the pp reaction. From now on, there are three possible paths to generate ^{4}He:

- The most frequent branch, called pp-I, involves the fusion of two ^{3}He:

$$\textbf{pp-I}: {}^3\text{He} + {}^3\text{He} \rightarrow {}^4\text{He} + 2p + \gamma \qquad Q = 12.86\,\text{MeV} \qquad B.R. = 84.92\% \tag{1.39}$$

- Another possibility is for a ^{3}He to find a ^{4}He produced by pp-I or hep (see later) branches:

$$^3\text{He} + {}^4\text{He} \rightarrow {}^7\text{Be} + \gamma \qquad Q = 1.59\,\text{MeV} \qquad B.R. = 15\% \tag{1.40}$$

  In this case, the production of ^{7}Be can be followed either by (99.9% of cases):

$$\textbf{pp-II}: {}^7\text{Be} + e^- \rightarrow {}^7\text{Li} + \nu_e \qquad Q = 0.862\,\text{MeV} \qquad \sim 90\%\text{ of cases} \tag{1.41a}$$
$$^7\text{Be} + e^- \rightarrow {}^7\text{Li} + \nu_e \qquad Q = 0.383\,\text{MeV} \qquad \sim 10\%\text{ of cases} \tag{1.41b}$$
$$^7\text{Li} + p \rightarrow {}^4\text{He} + {}^4\text{He} \qquad Q = 17.34\,\text{MeV} \tag{1.41c}$$

  or by the process (0.1% of cases):

$$\textbf{pp-III}: {}^7\text{Be} + p \rightarrow {}^8\text{B} + \gamma \qquad Q = 0.14\,\text{MeV} \tag{1.42a}$$
$$^8\text{B} \rightarrow {}^8\text{Be} + e^+ + \nu_e \qquad Q = 15\,\text{MeV} \tag{1.42b}$$
$$^8\text{Be} \rightarrow {}^4\text{He} + {}^4\text{He} \qquad Q = 0.14\,\text{MeV} \tag{1.42c}$$

  The two-body ^{7}Be electron capture 1.41a and 1.41b gives a monoenergetic neutrino. Approximately 90% of the neutrinos produced in this reaction carry an energy of 0.861 MeV, while the remaining $\sim$ 10% carry 0.383 MeV. The difference is whether the ^{7}Li produced is in the ground state or in an excited state, respectively.
  On the other hand, the ^{8}B decay gives a continuous neutrino distribution with an endpoint at about 15 MeV.

- The last possibility consists in a ^{3}He production via proton capture:

$$\textbf{hep}: {}^3\text{He} + p \rightarrow {}^4\text{He} + e^+ + \gamma \qquad Q = 18.9\,\text{MeV} \qquad B.R. \sim 10^{-5}\% \tag{1.43}$$

  Neutrinos produced in this reaction, the *hep* neutrinos, display a continuum spectrum and are characterized by the highest energies (until 18.8 MeV) among all the *pp* chain neutrinos. However, this interaction is very rare ($B.R \sim 10^{-5}\%$) and *hep* neutrinos have never been detected so far.

1.5.2 CNO cycle

When the core of the star contains elements heavier than hydrogen and helium, a series of fusion reaction different from the *pp* chain can occur. It is the case of the Carbon-Nitrogen-Oxygen cycle, the so-called *CNO cycle*. The net process of fusing four protons into a helium nucleus, two positrons and two neutrinos is still the same (see eq. 1.36) as well as the energy released: however, in this case, nuclei of carbon, nitrogen and oxygen participate as catalysts to aid the fusion process. The chain of reactions is shown in the right panel of Fig. 1.6.

The cycle begins with a ^{12}C nucleus capturing a free proton to form ^{13}N, which soon decays and produces a neutrino:

$$^{12}\mathrm{C} + p \rightarrow {}^{13}\mathrm{N} + \gamma \qquad Q = 1.94\,\mathrm{MeV} \tag{1.44a}$$

$$^{13}\mathrm{N} \rightarrow {}^{13}\mathrm{N} + e^{+} + \nu_e \qquad Q = 1.20\,\mathrm{MeV} \tag{1.44b}$$

The reaction continues with the decay of the ^{13}C:

$$^{13}\mathrm{C} \rightarrow {}^{14}\mathrm{N} + \gamma \qquad Q = 7.55\,\mathrm{MeV} \tag{1.45a}$$

$$^{14}\mathrm{N} + p \rightarrow {}^{15}\mathrm{O} + \gamma \qquad Q = 7.30\,\mathrm{MeV} \tag{1.45b}$$

$$^{15}\mathrm{O} \rightarrow {}^{15}\mathrm{N} + e^{+} + \nu_e \qquad Q = 1.732\,\mathrm{MeV} \tag{1.45c}$$

At this point, the ^{15}N can decay by one of two possible channels; the most probable one ($B.R. = 99.96\%$) proceeds via:

$$^{15}\mathrm{N} + p \rightarrow {}^{12}\mathrm{C} + {}^{4}\mathrm{He} \qquad Q = 4.97\,\mathrm{MeV} \tag{1.46}$$

The ^{12}C produced is now available to begin the chain again at reaction 1.44a. The other possible branch is much more rare ($B.R. = 0.04\%$) and it's the following:

$$^{15}\mathrm{N} + p \rightarrow {}^{16}\mathrm{O} + \gamma \qquad Q = 12.13\,\mathrm{MeV} \tag{1.47a}$$

$$^{16}\mathrm{O} + p \rightarrow {}^{17}\mathrm{F} + \gamma \qquad Q = 0.60\,\mathrm{MeV} \tag{1.47b}$$

$$^{17}\mathrm{F} \rightarrow {}^{17}\mathrm{O} + e^{+} + \nu_e \qquad Q = 1.74\,\mathrm{MeV} \tag{1.47c}$$

$$^{17}\mathrm{O} + p \rightarrow {}^{14}\mathrm{N} + {}^{4}\mathrm{He} \qquad Q = 1.2\,\mathrm{MeV} \tag{1.47d}$$

Only in the 0.04% of the cases the CNO cycle produces a neutrino from the decay of ^{17}F, thus the flux is much lower.
Within the CNO cycle, three solar neutrinos are produced, having continuous spectra with endpoints 1.2 MeV (^{13}N neutrinos), 1.73 MeV (^{15}O neutrinos) and 1.74 MeV (^{17}F neutrinos). In this work, I will refer to them as a whole, the so-called *CNO neutrinos*.

1.5.3 Solar neutrino fluxes

Solar neutrinos are generated in the same nuclear reactions that produce also photons we see as light. We can constrain the total neutrino flux by measuring the Sun's luminosity [24]:

$$\Phi \simeq \frac{L_\odot}{4\pi d^2 \cdot 1/2 \cdot 26.7\,\mathrm{MeV}} \simeq 6 \cdot 10^{10}\,\nu\,\mathrm{cm}^{-2}\,\mathrm{s}^{-1} \tag{1.48}$$

which is the so-called *solar luminosity constraint* where $L_\odot$ is the solar luminosity ($L_\odot = 4 \cdot 10^{33}$ erg/s), d is the average sun-to-earth distance ($d = 1.5 \cdot 10^{13}$ cm) and the factor 1/2 is due to the fact that the net reaction 1.36 produces two neutrinos. The relation 1.48 represents an approximate value: in fact, in order to obtain a precise estimation of the fluxes, a solar model depending by many factors, such as the solar temperature, the relative abundance of elements and the nuclear reaction rates, is needed.

With a complete calculation in the context of the SSM, the resulting neutrino fluxes on Earth, as a function of the neutrino energy, are illustrated in Fig. 1.7.

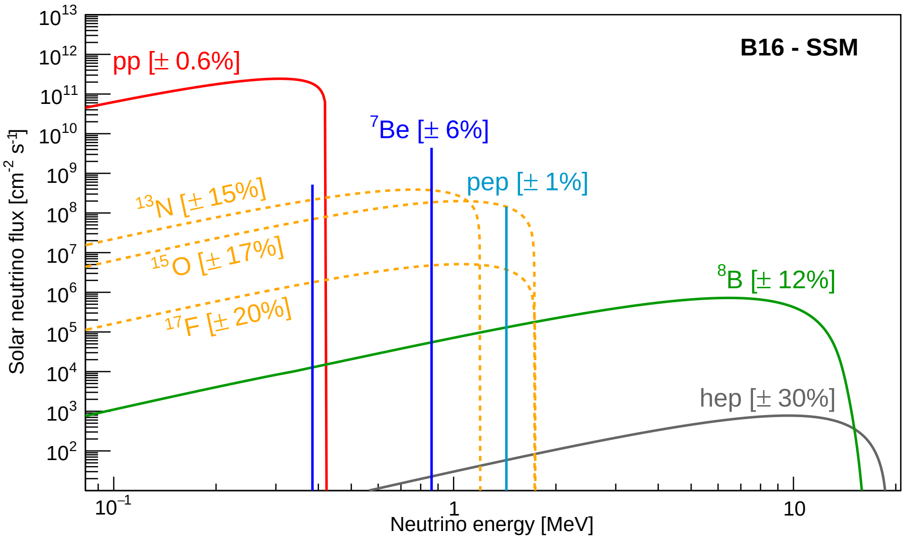

Figure 1.7: Solar neutrino fluxes on Earth predicted by the Solar Standard Model [16]. The flux is given in $\mathrm{cm}^{-2}\,\mathrm{s}^{-1}\,\mathrm{MeV}^{-1}$ units for continuum sources (*pp*, ^{8}B, CNO and *hep* neutrinos) and in $\mathrm{cm}^{-2}\,\mathrm{s}^{-1}$ units for monoenergetic sources (^{7}Be and *pep* neutrinos).

1.6 Solar neutrino experiments

Since the neutrino mass is negligible, the gravitational force can be neglected and we can assume neutrinos to interact only via the weak interaction. The typical weak cross sections are about $10^{-45} - 10^{-41}$ cm^2 at 1 MeV energy. As a consequence, neutrinos are characterized by an elusiveness that makes them difficult to detect. To maximize the number of interactions between neutrinos and the detector targets, it's necessary either to increase the neutrino fluxes or to have a high number of targets in the detector volume. Since solar neutrino fluxes are fixed by nature, for solar neutrinos to be efficiently detected huge detectors' masses (≈ hundreds of tons) are

Solar ν	Flux B16-GS98 (HZ) [$\mathrm{cm}^{-2}\,\mathrm{s}^{-1}$]	Flux B16-AGSS09 (LZ) [$\mathrm{cm}^{-2}\,\mathrm{s}^{-1}$]
pp	$5.98(1 \pm 0.006) \cdot 10^{10}$	$6.03(1 \pm 0.005) \cdot 10^{10}$
^{7}Be	$4.93(1 \pm 0.06) \cdot 10^{9}$	$4.50(1 \pm 0.06) \cdot 10^{10}$
pep	$1.44(1 \pm 0.01) \cdot 10^{8}$	$1.46(1 \pm 0.009) \cdot 10^{9}$
^{8}B	$5.46(1 \pm 0.12) \cdot 10^{6}$	$4.50(1 \pm 0.12) \cdot 10^{6}$
hep	$7.98(1 \pm 0.30) \cdot 10^{3}$	$8.25(1 \pm 0.30) \cdot 10^{3}$
^{13}N	$2.78(1 \pm 0.15) \cdot 10^{8}$	$2.04(1 \pm 0.14) \cdot 10^{8}$
^{15}O	$2.05(1 \pm 0.17) \cdot 10^{8}$	$1.44(1 \pm 0.16) \cdot 10^{8}$
^{17}F	$5.29(1 \pm 0.20) \cdot 10^{6}$	$3.26(1 \pm 0.18) \cdot 10^{6}$
All CNO	$4.88(1 \pm 0.16) \cdot 10^{8}$	$3.51(1 \pm 0.15) \cdot 10^{8}$

Table 1.2: The neutrino fluxes in $\mathrm{cm}^{-2}\,\mathrm{s}^{-1}$ units with their uncertainties as predicted by the B16-GS98 SSM (HZ) and the B16-AGSS09 SSM (LZ) [16].

required. Neutrino experiments are often built underground, to shield the detector from cosmic rays and make use of high radiopurity materials to minimize other possible background radiations, that could mimic the neutrino-induced signal in the detector. Since they are electrically neutral, neutrinos are not able to ionize the matter they are crossing and so they cannot be detected directly. What we observe are the secondary products coming from the interaction between the neutrinos and the detector targets.

Neutrino experiments can be classified into two categories, based on their detection technique: the *radiochemical experiments* and the *real-time experiments*.

- **Radiochemical experiments**: they are based on the neutrino capture reaction by an isotope X:

  $$\nu_e + {}^{A}_{Z}\mathrm{X} \rightarrow {}^{A}_{Z+1}\mathrm{Y} + e^- \tag{1.49}$$

  Chemical techniques are used to isolate and collect the reaction products Y, which are then counted with proportional counters. Due to that, the daughter nucleus Y must have a suitable lifetime.
  This method is sensitive only to electron neutrinos and allows to measure only the total rate of interactions in a specific volume and beyond an energy threshold. Several other information such as the neutrino direction of arrival, the position of interaction and the energy are lost.

- **Real-time experiments**: the advantage of these experiments is that they are able to provide information about the energy, the interaction position and, only for Cherenkov detectors and not for scintillators, the direction of neutrinos. They reveal neutrinos through their elastic scattering off the electrons of the target, or their reactions on the deuterium.

1.6.1 The Solar Neutrino Problem and its solution

The first experiment able to detect solar neutrinos was Homestake, a radiochemical detector designed by Davis in the late 1960s [25] and located in a gold mine in South Dakota (USA). It was filled with $\sim$ 600 t of C_2Cl_4 and neutrinos were detected through the reaction $\nu_e + {}^{37}\mathrm{Cl} \rightarrow {}^{37}\mathrm{Ar} + e^-$. The produced argon was then chemically extracted with the aid of helium; the event rate was $\sim$ 2 atoms of argon per day. Despite the 4000 mwe[2], the main background was due to cosmic muons, which produced argon after their interaction with chlorine. Since the threshold of the neutrino capture by ^{37}Cl is 0.814 MeV, Homestake was not sensitive to pp and part of ^{7}Be neutrinos (see Fig. 1.7). The final measured rate was $2.56 \pm 0.16 \pm 0.16$ SNU[3] [18], about a third of the SSM prediction of 9.3 SNU. This discrepancy between the measured and the predicted values was the first hint of the *solar neutrino problem*, consisting in the deficit of the neutrino interaction rate experimentally measured with respect to the predictions given by the SSM.

A lower energy threshold could be reached in radiochemical experiments that employed gallium and detected neutrinos thanks to the reaction $\nu_e + {}^{71}\mathrm{Ga} \rightarrow {}^{71}\mathrm{Ge} + e^-$. The threshold of this reaction is 0.233 MeV, thus allowing also the detection of pp neutrinos, which have the most abundant flux according to the SSM (see Fig. 1.7). Three experiments employed gallium: the SAGE experiment [26], in Baksan (Russia), with a shielding of 4700 mwe, used about 50 t of liquid metallic gallium as a target; the GALLEX experiment [27] and its successor GNO [28, 29], both at LNGS (Italy) under a 3800 mwe mountain shielding. GALLEX used a 30 t tank containing a solution of HCl and $GaCl_3$, while GNO exploited the same detector setup with an improved extraction equipment. All these experiments confirmed a lack in the solar neutrino fluxes, by observing almost half of the expected capture rate. In particular, the averaged solar neutrino interaction rate measured by SAGE, GALLEX and GNO was 68.3 ± 3.8 SNU, thus confirming the solar neutrino problem.

Therefore, either the SSM was wrong, although supported by helioseismology observations, or "something was happening" to the neutrinos while traveling from the production point inside the Sun to the Earth.

Super-Kamiokande

Super-Kamiokande (SK) is a 50 kton pure mass water Cherenkov detector with more than 11 000 inward-facing 50-cm diameter PMTs, located in the Kamioka mine (Japan), under 2500 mwe [30] and still taking data. It is the successor of

---

[2] The *meter water equivalent (mwe)* is a standard measure of cosmic rays attenuation in underground laboratories. One mwe of material is defined as the thickness of that material providing a shielding equivalent to one meter of water.

[3] A *Solar Neutrino Unit (SNU)* corresponds to a rate of 10^{-36} captures/atom/s.

Kamiokande [31], the first real-time experiment consisting of a 3 kton mass water Cherenkov detector. In both these experiments, neutrinos are detected through the elastic scattering (ES) off water electrons. This reaction does not have an intrinsic threshold, but an energy threshold is anyway imposed by the radioactive background, that dominates the low energy range. The ultimate threshold of SK was 3.5 MeV, thus making it able only to detect ^{8}B neutrinos. The most recent ^{8}B neutrino flux measured by SK is $(2.308 \pm 0.020 \pm 0.040) \cdot 10^6 \mathrm{cm}^2\,\mathrm{s}^{-1}$ [32], which is approximately 0.4 times the SSM predicted flux, thus providing a confirmation of the results from the radiochemical experiments. It's worth emphasizing the fact that both Kamiokande and Super-Kamiokande showed for the first time that the detected electron neutrinos did come from the Sun, thanks to the directional information provided by the Cherenkov detection.

Despite the beginning of real-time experiments era, the solar neutrino problem was still an open issue. A first hint towards its solution lay with the fact that all the experiments considered so far were unable to observe the solar neutrino flux independently of the neutrino flavor. This innovative approach was first performed by the SNO experiment.

SNO

The Sudbury Neutrino Observatory (SNO) [33] was a real-time water Cherenkov experiment located in Canada, at a depth of 6010 mwe. It consisted of 1 kton of pure heavy water (D_2O) limited by a 18 m diameter stainless sphere, with approximately 10 000 inward-facing PMTs. This inner structure is surrounded by an ultrapure H_2O shield in order to limit the amount of background events coming from the adjacent rock and from the PMTs themselves. The heavy water dictates an intrinsic energy threshold of 6 MeV, thus letting SNO reveal only ^{8}B neutrinos, like Super-Kamiokande did.

The advantage of using deuterium lies in the fact that SNO was able to detect solar neutrinos via three different interactions:

- Elastic scattering (ES) off an electron

  $$\nu_x + e^- \to \nu_x + e^- \tag{1.50}$$

  via both charged and neutral current interactions, like in SuperK, thus measuring a combined flux of all flavors: $\phi_{\mathrm{ES}} = \phi(\nu_e) + 0.18(\phi(\nu_\mu) + \phi(\nu_\tau))$.

- Charged current (CC) interaction with the deuterium:

  $$\nu_e + d \to p + p + e^- \tag{1.51}$$

  Only electron neutrinos can be detected through this channel, thus providing a measurement of the electronic component of the flux: $\phi_{\mathrm{CC}} = \phi(\nu_e)$.

- Neutral current (NC) interaction with the deuterium:

$$\nu_x + d \rightarrow p + n + \nu_x \tag{1.52}$$

The reaction is sensitive to all neutrino flavors with equal cross section, thus providing a measurement of the total flux: $\phi_{\mathrm{NC}} = \phi(\nu_e) + \phi(\nu_\mu) + \phi(\nu_\tau)$.

The total flux of ^{8}B neutrinos measured by SNO, $\phi_{\mathrm{NC}} = 5.25 \cdot 10^6\ \mathrm{cm}^{-2}\ \mathrm{s}^{-1}$ [34], was finally in agreement with the SSM prediction, thus suggesting the solution of the solar neutrino problem.

SNO results pointed to the existence of a non-ν_e component in the solar neutrino flux and provided an explanation for the low measured rate in the previous experiments: some of the ν_e produced inside the Sun oscillate into ν_μ or ν_τ before reaching the Earth. The solution to the solar neutrino problem is given by neutrino oscillations.

1.6.2 The Borexino experiment

Borexino is a real-time 300 tons ultra-pure liquid scintillator (LS) detector located at LNGS (Italy), at a depth of 3800 mwe, that exploits the Gran Sasso mountain as a passive shielding against the cosmic muon radiation, which is suppressed by a factor of $\sim 10^6$.

The Borexino detector has an onion-like structure with the radiopurity of materials increasing towards the center [35] and detects neutrinos of all flavors via the electron-neutrino elastic scattering. The main neutrino target, located in the core of the detector, is 280 tons of LS - pseudocumene (PC) as a solvent and PPO as a solute. The scintillator is contained in a thin spherical nylon inner vessel (IV) with a radius of 4.25 m and it is surrounded by a non-scintillating buffer liquid. The buffer region is held by a nylon outer vessel (OV) with a radius of 5.50 m, followed by a second outer buffer region, which in turn is surrounded by a stainless steel sphere (SSS) with a radius of 6.85 m, which holds 2218 photomultiplier tubes, facing inwards. The buffer regions shield the inner volume against external radioactivity from the PMTs and the SSS. The SSS is enclosed in a cylindrical tank filled with high-purity water, additionally endowed with 208 external PMTs. This water tank serves as an extra shielding against external gammas and neutrons, and as an active Cherenkov veto for residual cosmic muons passing through the detector.

Results on *pp*, *pep*, ^{7}Be and ^{8}B neutrinos

The interaction rates of the *pp*, *pep* and ^{7}Be neutrinos were obtained through a spectral fit in the so-called *LER (Low-Energy Region)*, below 3 MeV. Due to a strong correlation between the spectral shapes of *pep*, CNO and ^{210}Bi, which is a significant contaminant of the LS, the CNO rate was constrained in the fit to the SSM prediction. The fit results in terms of interaction rates of solar neutrinos in counts per day per 100 ton (cpd/100ton) are given in Table 1.3, including systematic errors. The analysis was repeated for both HZ-SSM and LZ-SSM with the expected CNO rate of 4.92 ± 0.55 cpd/100 ton and 3.52 ± 0.37 cpd/100 ton, respectively. This fact influences only the resulting *pep* neutrino rate and is thus given separately with the label HZ and LZ.

On the other hand, the measurement of ^{8}B neutrinos was performed in the so-called *HER (High-Energy Region)*, above 3.2 MeV and below 16 MeV, and the related results are also reported in Table 1.3.

Solar ν	Rate [cpd/100ton]	Flux [cm^{-2} s^{-1}]	SSM Flux [cm^{-2} s^{-1}]
pp	$134 \pm 10^{+6}_{-10}$	$6.1 \pm 0.5^{+0.3}_{-0.5}$	$5.98(1 \pm 0.006)$ (HZ) $6.03(1 \pm 0.005)$ (LZ)
^{7}Be	$48.3 \pm 1.1^{+0.4}_{-0.7}$	$4.99 \pm 0.11^{+0.06}_{-0.08}$	$4.93(1 \pm 0.06)$ (HZ) $4.50(1 \pm 0.06)$ (LZ)
pep (HZ)	$2.43 \pm 0.36^{+0.15}_{-0.22}$	$1.27 \pm 0.19^{+0.08}_{-0.12}$	$1.44(1 \pm 0.01)$ (HZ) $1.46(1 \pm 0.009)$ (LZ)
pep (LZ)	$2.65 \pm 0.36^{+0.15}_{-0.24}$	$1.39 \pm 0.19^{+0.08}_{-0.13}$	$1.44(1 \pm 0.01)$ (HZ) $1.46(1 \pm 0.009)$ (LZ)
^{8}B	$0.223^{+0.015+0.006}_{-0.016-0.006}$	$5.68^{+0.39+0.03}_{-0.41-0.03}$	$5.46(1 \pm 0.12)$ (HZ) $4.50(1 \pm 0.12)$ (LZ)

Table 1.3: Results of the *pp*-chain solar neutrino analysis [36]. The first error is statistical, the second is the systematic. The last column shows the fluxes as predicted by the HZ- and LZ-SSM (see Table 1.2). The fluxes of *pp*, ^{7}Be, *pep* and ^{8}B neutrinos are normalized to 10^{10}, 10^9, 10^8 and 10^8, respectively. The results on *pep* neutrino rate are given separately with the labels HZ and LZ since the fit has been repeated with the CNO rate constrained to HZ- and LZ-SSM predictions.

Results on CNO neutrinos

Borexino also provided the first experimental confirmation of the existence of the CNO fusion in the Sun [37]. To extract the CNO neutrino interaction rate from data, a multivariate analysis has been performed. The main difference between this analysis and the *pp* chain ones consists in the introduction of the constraints on *pep* neutrinos, supplied by the SSM, and the ^{210}Bi background. The latter was obtained through an independent measurement achieved after the thermalization of the detector. The best fit value is $R_{\text{CNO}} = 7.2 \pm 3.0$ cpd/100 ton (68% confidence interval), including systematic uncertainties: the inferred flux of CNO neutrinos at Earth is $\Phi_{\text{CNO}} = (7.0 \pm 3.0) \cdot 10^8$ cm^{-2} s^{-1} (68% confidence interval). As depicted in Fig. 1.8, the observed CNO rate is compatible with both SSM-HZ and SSM-LZ predictions, such that we cannot distinguish between the two different models: the statistical compatibility for HZ is 0.5σ and for LZ is 1.3σ.

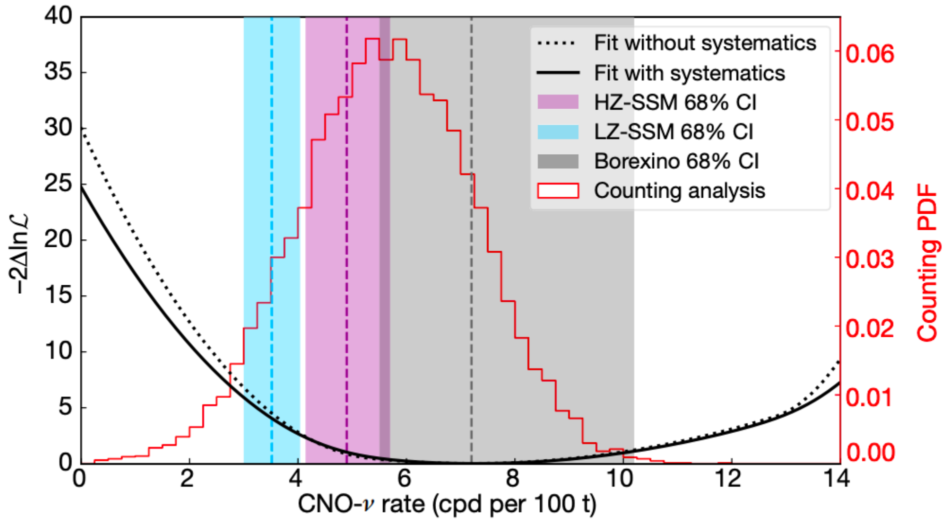

Figure 1.8: CNO neutrino rate negative log-likelihood ($\ln\mathcal{L}$) profile obtained directly from the multivariate fit (dashed black line) and after folding in the systematic uncertainties (black solid line). The histogram in red shows the CNO-neutrino rate obtained from the counting analysis. The blue, violet and grey vertical bands show 68% confidence intervals (CI) for the SSM-LZ and SSM-HZ predictions, while the Borexino result (corresponding to the black solid-line log-likelihood profile), respectively [37].

CHAPTER 2

The JUNO experiment

The Jiangmen Underground Neutrino Observatory (JUNO) is a 20 kton multi-purpose underground liquid scintillator detector. Its main physics goal is the determination of the neutrino mass ordering (NMO) by detecting reactor antineutrinos [38]. JUNO is located in Jiangmen city, Guandong province (Southern China), in an underground laboratory with a total shielding corresponding to $\approx$ 1800 mwe (see Fig. 2.1). By taking the surveyed mountain profile into account, the simulations predict a muon rate of 4 $\mathrm{mHz/m^2}$ [39], approximately 60 times higher than in Borexino. The site location was chosen in order to optimize the sensitivity for the NMO measurement. Moreover, to avoid de-phasing effects in the detected antineutrino spectrum, the distances to the nearby Yangjiang and Taishan nuclear power plants (NPP) are both $\approx$ 53 km, with a total thermal power of $\approx$ 36 GW. The end of JUNO construction is scheduled for 2022.

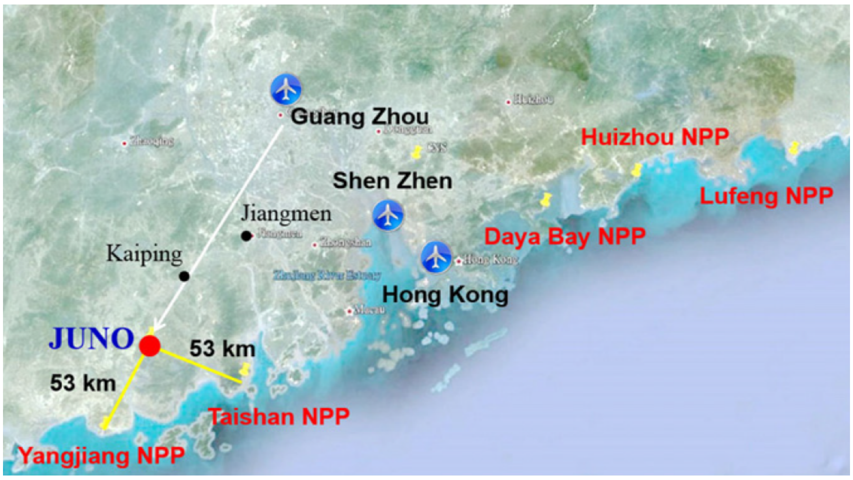

Figure 2.1: Location of the JUNO site. The distances to the nearby Yangjiang and Taishan NPPs are both $\approx$ 53 km. The Daya Bay complex, $\approx$ 215 km far away, is also shown [38].

2.1 JUNO physics goals

The large size and the unprecedented effective energy resolution of $\lesssim 3\%/\sqrt{\text{E [MeV]}}$ will allow JUNO to be a unique tool for addressing several physics questions. Besides being designed to study the NMO, the JUNO experiment is able to contribute significantly to a broad range of topics in astroparticle and fundamental physics.

Neutrino mass ordering (NMO) determination

As pointed out in Chapter 1, there are two different NMO – normal and inverted – and the determination of the correct one is still an open issue. Different NMO lead to different energy spectra, as illustrated in Fig. 2.2. Particularly, it's immediately clear the discrepancy between the unrealistic hypothesis of no oscillations versus the oscillation case. In the latter we can observe both the oscillations driven by the smaller mass splitting Δm^2_{21}, the so-called *slow oscillations*, and the large mass splittings (Δm^2_{31} and Δm^2_{32}), the so-called *fast oscillations*. Moreover, there is a further discrepancy between the normal NMO energy spectrum (blue line) and the inverted one (red line). With a baseline of 53 km (medium baseline), JUNO will be the first experiment optimized for measure both the slow and the fast oscillations.

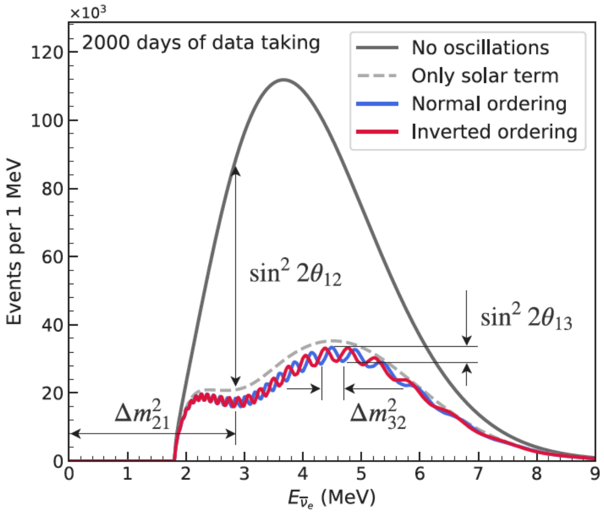

Figure 2.2: The expected antineutrino energy spectrum without oscillation (black line) and with oscillation for normal NMO (blue line) and inverted NMO (red line), assuming 2000 days (≈ 6 years) of data-taking at the JUNO experiment. The dependence on the four oscillation parameters is shown [39].

In JUNO, the NMO information will be extracted from the spectral shape of the prompt electron coming from the inverse beta-decay (IBD) reaction:

$$\overline{\nu}_e + p \rightarrow e^+ + n \tag{2.1}$$

Antineutrinos produced in the nuclear power plants interact with protons of the liquid scintillator, producing a positron and a neutron. The positron loses its kinetic energy in a short length and then annihilates with an electron, thus generating a prompt signal within few ns, given by two 0.511 MeV γ-rays. The neutron is captured with a typical delay of a few hundred seconds and produces a delayed signal of 2.2 MeV. The spatial, temporal and energetic coincidence typical of this *golden channel* will allow to significantly reduce backgrounds.

Since the JUNO NMO sensitivity from atmospheric neutrinos is complementary to the reactor antineutrinos one, also the spectrum of atmospheric neutrinos will be analyzed. It covers a broad range in baseline (15 km $-$ 13000 km) and in energy (0.1 GeV $-$ 10 TeV). The baseline of an atmospheric neutrino is described by the zenith angle of its direction, which can be resolved via tracking algorithms of the secondary particles. The large ranges mentioned above allow to investigate a wide range of the neutrino oscillation parameters with respect to antineutrinos reactors thus enhancing the sensitivity.

Solar neutrinos

JUNO will be the perfect candidate detector to perform a precision spectroscopy of solar neutrinos. In fact, despite its overburden is relatively shallow compared to other underground experiments, such as Borexino or Super-Kamiokande, by combining its large volume and high light yield, JUNO has the potential to make significant contributions to the understanding of solar neutrinos.

The solar neutrinos analysis requires extremely low levels of radiopurity (see Chapter 3) whereby a big effort is being made, as discussed in Section 2.4. Two distinct and separated analysis are carried on about this topic: the ^{8}B and the intermediate energy (*pep*, ^{7}Be and CNO neutrinos) solar neutrinos ones; the latter being extensively described in the following. The low energy region of *pp* neutrinos is instead not addressed due to additional complications.

For what concerns the sensitivity to the measurement of ^{8}B solar neutrinos [40], the expected signal and background spectra are shown in Fig. 2.3, assuming a 10^{-17} g/g level for the intrinsic ^{238}U and ^{232}Th contamination. In ten years of data taking, after all cuts are applied, about 60 000 signal events and 30 000 background events are expected in the energy range above 2 MeV.

Geoneutrinos

Geoneutrinos are a unique tool to study our planet. The inverse beta decay on protons with 1.8 MeV threshold makes possible to measure geoneutrinos from the ^{238}U and ^{232}Th decay chains. Only two experiments have measured geoneutrinos so far: KamLAND [41, 42, 43] and Borexino [44, 45, 46, 47]. However, with its detector being at least 20 times larger than the existing ones, JUNO will join the family of geoneutrino experiments and will represent a fantastic opportunity to measure geoneutrinos. Within the first year of running, JUNO will record more geoneutrino

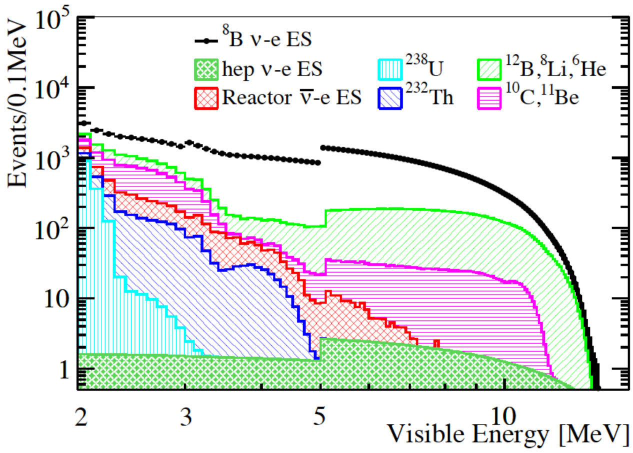

Figure 2.3: Expected signal and background spectra in the $\nu - e$ elastic scattering channel in ten years of data taking, with all selection cuts and muon veto methods applied. The energy-dependent fiducial volumes account for the discontinuities at 3 MeV and 5 MeV due to some selection cuts which removes 20% of signals in the energy range of 3 to 5 MeV, and less than 2% in other energy ranges [40].

events than all other detectors will have accumulated to that time.

Supernova neutrinos

The rare occurrence of a core-collapse supernova in our galaxy would flush JUNO with all flavors of neutrinos and antineutrinos, triggering a whole bunch of detection channels. JUNO will have an excellent capability of detecting all flavors of the postshock neutrinos [48]. The detection channels are mainly the IBD one, $\overline{\nu}_e + p \to e^+ + n$, the elastic neutrino-electron scattering, $\nu_x + e^- \to \nu_x + e^-$, and the elastic neutrino-proton scattering, $\nu_x + p \to \nu_x + p$. The charged current ν_e and $\overline{\nu}_e$ interactions on ^{12}C nuclei are also observable, as well as the neutral current interactions $\nu_x + {}^{12}\mathrm{C} \to \nu_x + {}^{12}\mathrm{C}^*$, where in the above formulas the x subscript stands for $x = e, \mu, \tau$. The less abundant ^{13}C atoms in the LS are also considered as a target and both their CC and NC interactions are taken into account. For a supernova at a distance of 10 kpc, JUNO will overall register about 10^4 events.

Diffuse supernova neutrino background (DSNB)

The so-called *diffuse supernova neutrino background* (DSNB), a low isotropic flux of neutrinos on the level of $\sim 10\,\nu\,\mathrm{cm}^{-2}\,\mathrm{s}^{-1}$ expected from the cumulated supernova rate in our universe, has never been detected yet. Thanks to its large target mass, JUNO could detect between two and four DSNB events per year as IBDs in the energy range above 10 MeV, under which the high event rates of reactor antineutrinos dominate, and below 30 MeV, over which the CC interactions from atmospheric neutrinos are dominant [39].

Exotic physics

Finally, JUNO has the potential to investigate exotic physics beyond the SM. Some examples are the search for sterile neutrinos at the eV mass scale, the nucleon decays and the neutrinos from dark matter annihilation in the Sun [38].

2.2 The detector design

The JUNO detector consists of a Central Detector (CD), a Water Cherenkov Detector (WCD) and a Top Tracker (TT). A schematic view of the whole structure is shown in Fig. 2.4.

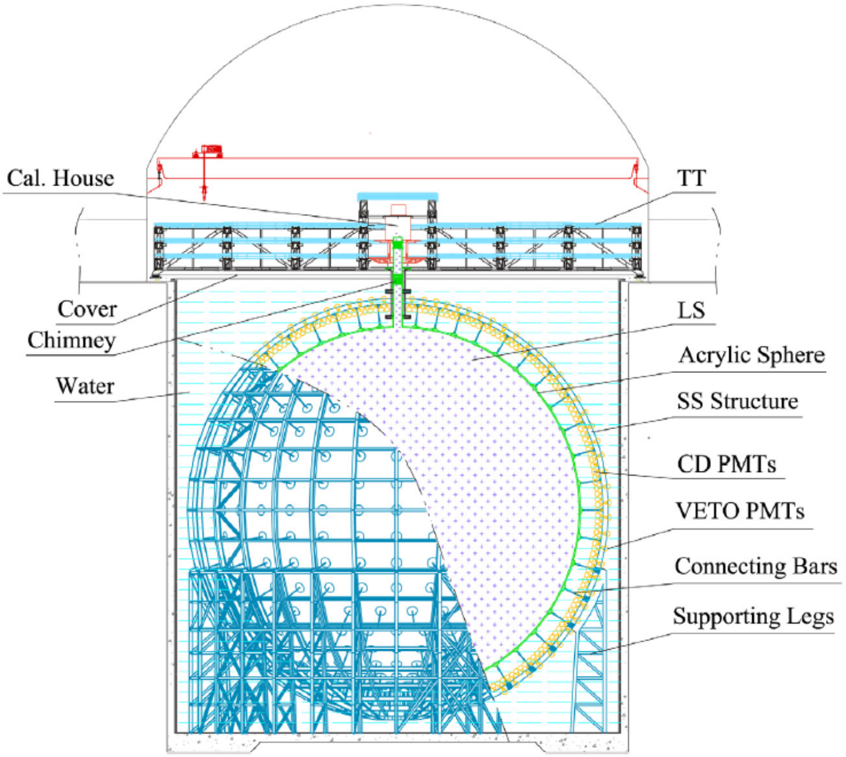

Figure 2.4: Schematic layout of the JUNO detector [39].

The CD contains 20 kton of liquid scintillator (LS) in a spherical acrylic vessel, supported by a stainless steel (SS) structure via connecting bars. An array of PMTs, which are installed on the inner surface of the SS structure, looks at the light emitted by the LS. The CD is submerged in a cylindrical WCD. Thanks to another system of PMTs, mounted on the SS structure, the WCD provides sufficient buffer in all directions to both protect the LS from the surrounding rock radioactivity and act as Cherenkov veto for cosmic muons. In order to accurately measure the muon tracks, on top of the WCD there is a plastic scintillator array, the TT. Finally, a chimney for the calibration operations is connected to the top of the acrylic vessel.

2.2.1 Water Cherenkov Detector and Top Tracker

Given the extremely precise measurements that JUNO is going to address, the background control is fundamental. The muon background is of the order of several Hz in the CD and has to be compared with the 60 events/day from IBD and even less event rates for other neutrino sources, like solars or geoneutrinos. A high efficiency muon veto system is therefore necessary to monitor this background.

The Water Cherenkov Detector (WCD) is a cylinder of 43.5 m diameter and 44 m height and it is filled with 35 kton of ultrapure water. The Cherenkov light produced in the water is detected by 2400 LPMTs, mounted outwardly on the spherical SS structure. To increase the light collection efficiency, some reflective foils provide a coating for the pool walls and the SS support structure [49].

To improve the reconstruction of the cosmic muons direction, a plastic scintillator strips tracker is placed on top of the WCD. It is inherited from the decommissioned target tracker of the OPERA experiment [50]. As shown in Fig. 2.5, the TT is composed of 63 walls with a sensitive area of 6.7 m × 6.7 m each. The TT walls are distributed on a 3 × 7 horizontal grid and grouped in 3 horizontal layers. The three walls in the center of the TT are moved up to leave enough space for the calibration house and the CD chimney. The distance between two layers is 1.5 m, which is reduced for the section above the chimney. The TT covers ≈ 25% of the area of the top surface of the WCD.

Each TT wall is made using a total of 512 strips of plastic scintillator. In every strip, wavelength-shifting fibers are placed; these are read from both sides by 64-channel multi-anode photomultipliers.

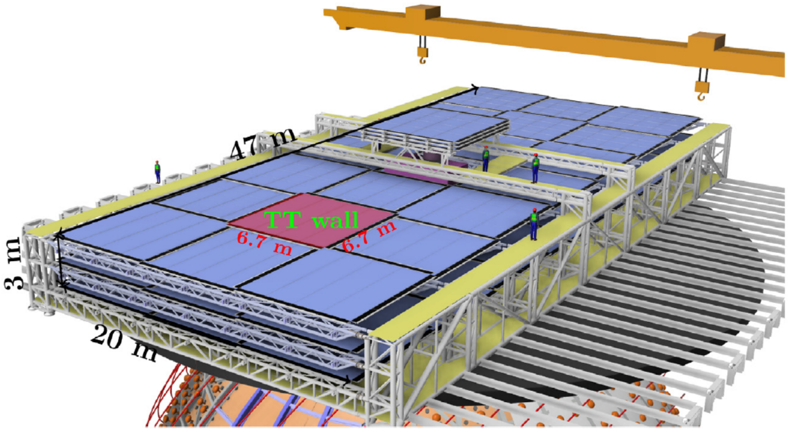

Figure 2.5: The JUNO Top Tracker [39].

2.2.2 PMTs system

The light produced by the LS molecules is converted into an electrical signal by means of photomultiplier tubes (PMTs).

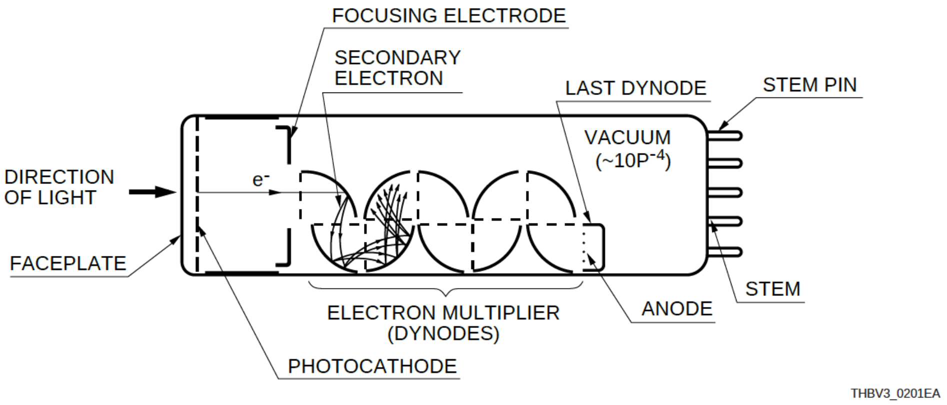

Figure 2.6: Scheme of the working principle of a PMT. From [51].

Fig. 2.6 shows an exemplary scheme of the PMT detection principles. An incoming photon hits the photocathode behind the PMT surface glass and may emit a so-called *photoelectron (p.e.)* via the photoelectric effect. This electron is accelerated to the first dynode to knock more electrons out from the dynode itself. For the electrons' acceleration to take place, the PMT is connected to a high voltage generator. Then, by using multiple dynode stages, a multiplication process starts and a cascade of electrons is produced. Finally, these secondary electrons reach the anode to form a detectable electrical signal, which is then processed. In most PMTs, the charge amplification is a linear process, so that the output pulse at the anode is proportional to the initial number of photoelectrons over a wide range of amplitudes.

The PMT properties are characterized by several parameters, the most important being the *photon detection efficiency (PDE)* and the *dark counts rate (DCR)*. The PDE is the product of the *quantum efficiency (QE)* and the *collection efficiency (CE)*. The QE is the ratio of the emitted photoelectrons and the number of incident photons, and depends mainly on the photocathode material and on the wavelength of the incident photons. On the other hand, the CE is the ratio between the number of electrons reaching the useful area of the first dynode and the total number of electrons emitted by the photocathode. Hence, the PDE represents the probability of measuring a signal after a photon hit the PMT.

Furthermore, even in total darkness, a current can still be measured at the anode of a PMT, mostly due to the thermionic emission of electrons from the photocathode or the dynodes. These "false signals" are called dark counts, from which we have the DCR.

To achieve the planned energy resolution, a series of design requirements concerning the PMTs system have been established: a PMT geometry coverage of the CD sphere ⩾ 75% and a PMT photocathode quantum efficiency ⩾ 35% [38]. The JUNO PMTs array consists of a double system of 17612 20-inch PMTs (referred to as large PMTs or LPMTs) and 25600 3-inch PMTs (referred to as small PMTs or SPMTs), arranged on the CD sphere.

The LPMTs are produced by two different companies: there are 5000 dynode photomultipliers from Hamamatsu Photonics [52] and 12612 microchannel plate photomultipliers by Northern Night Vision Technology (NNVT) [53]. The LPMT system has been designed to maximize the photon collection and thus obtain a high energy resolution. The high coverage of the LPMT system allows to detect a large number of photoelectrons for neutrino events, with a yield estimated at ≈ 1500 p.e./MeV. However, for the events close to the CD edge, a large fraction of the charge is collected by few PMTs, which can undergo saturation in their acquisition. Even if the range of LPMTs is wide, the systematic errors associated with the charge integration, such as the non-linearity, can be significant.

The SPMTs, produced by HZC Photonics [54], are distributed uniformly on the sphere and placed in the spaces between the LPMTs themselves, as shown in Fig. 2.7. The SPMT system operates in single-photon counting regime within a wide energy range and it is designed to increase the detector performances at high energy and to reduce the systematic errors associated to the LPMTs.

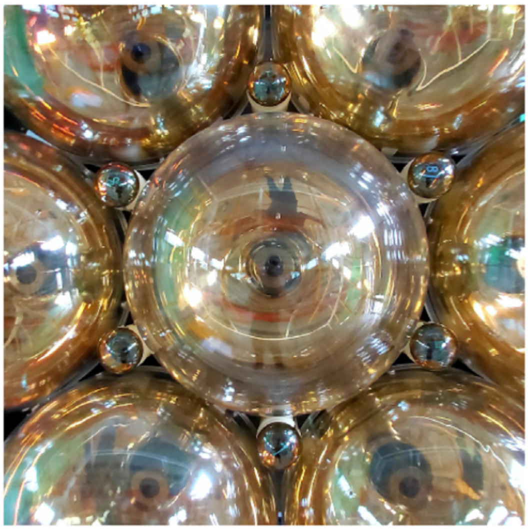

Figure 2.7: A real size mock-up of SPMTs interlaced with the LPMTs. From [39].

The SPMTs also contribute in the reconstruction of high energy events, such as cosmic muons. Thanks to their better timing, they also improve the muon tracking, which is particularly relevant for keeping the backgrounds produced by cosmic-ray muons under control.

2.2.3 Central Detector

Given its huge size, the CD design has been one of the most challenging parts of JUNO. Its core is filled with the liquid scintillator, described in Section 2.2.4. The LS is contained in a spherical acrylic vessel with an inner diameter of 35.4 m and a thickness of 120 mm. This is supported via 590 connecting bars by a spherical SS structure with an inner diameter of 40.1 m. This structure sits on a shock absorber consisting of 30 pairs of supporting legs, rooted on the concrete floor of the WCD. A depiction of the CD is illustrated in Fig. 2.8.

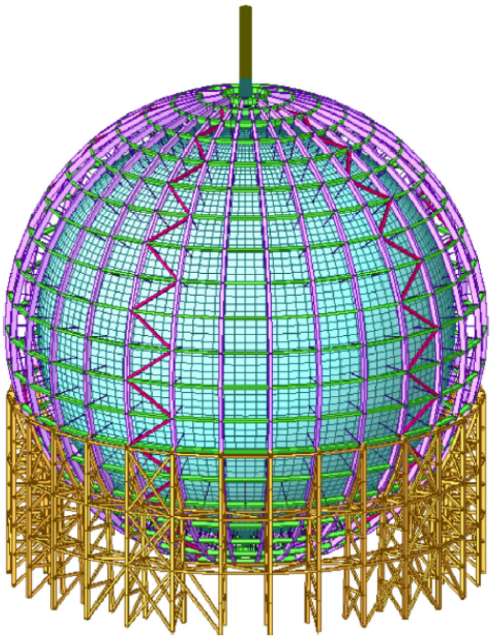

Figure 2.8: Scheme of the JUNO Central Detector (CD). The SS truss is visible, together with the supporting pillars. PMTs are not displayed [39].

The light emitted by the LS is watched by a system of PMTs installed on the SS structure and pointing inward. A water buffer of 1.42 m thickness between the acrylic vessel and the PMT surface protects the LS from the PMT glass' radioactivity.

2.2.4 Liquid scintillator

Scintillation is one of the detection methods used in particle physics for particle detection [55]. When a charged particle passes through a scintillator, it deposits its kinetic energy within the target, which is then converted into light. The emitted light is subsequently collected by photomultipliers tubes, coupled to the scintillators, which finally convert the photon signal into a readable electrical output. To have a good light collection, the scintillator should be transparent to its own emitted light. A *wavelenght shifter* is often used to achieve this point: it absorbs light and re-emits it with a longer wavelength. Together with these kinds of light emission, there might be other radiationless de-excitation modes due to impurities in the scintillating material, the so-called *quenching* processes.

A good scintillator should maximize the amount of incident energy that is converted into prompt fluorescence and minimize the other contributions. Ideally, it should also guarantee a high *scintillation efficiency*, i.e. the fraction of the incident particle energy which is converted into optical photons and high *light yield (LY)*, i.e. the amount of light emitted per unit energy, which usually expressed as the number of photons per 1 MeV of deposited energy. A high light yield contributes to a high energy resolution. It is also very important that the conversion from the deposited energy to photons is linear; quenching is one of the causes of the non-linear response.

Scintillating materials can be divided into two main categories, *organic* and *inorganic*, depending on the mechanism responsible for the emission of light.
Organic scintillators, like the one employed in JUNO, are composed of aromatic hydrocarbon structures and are faster than inorganic ones, with a typical emission time of $\approx$ 2 ns; by contrast, they have a lower light yield. In this kind of scintillators, the energy level structure of molecules is the only one responsible for the light emission and both the electronic levels and the vibrational states of the organic molecule are involved in the process. Since they can be easily provided in considerable amounts in liquid form, organic scintillators are often employed in large volume detectors for rare processes, like JUNO itself does.

The core of the JUNO detector is composed by 20 kton of an organic liquid scintillator, with a density of 0.859 g/ml, contained in the inner vessel. The LS needs to have a good light yield and, due to the large size of the detector, an excellent transparency. In order to achieve this, linear alkylbenzene (LAB), which constitutes more than 98% of the LS, is used as the solvent due to its exceptional transparency and good light yield ($\approx 10^4$ γ/MeV). The solute is a two-component system of the flour 2,5-Diphenyloxazole (PPO) and the wavelength shifter 1,4-Bis(2-methylstyryl)benzene (Bis-MSB), added to LAB with concentrations equal to 2.5 g/l and 3 mg/l, respectively [56].

Besides the chemical composition of the LS mixture, its cleanliness and radiopurity are important. The minimum requirements on the ^{238}U/^{232}Th chains radiopurity of the LS are 10^{-15} g/g for reactor neutrino studies and 10^{-17} g/g for solar neutrino studies (see Section 3.2). To ensure these, a purification plant is planned in situ at the underground laboratory of the JUNO experiment [57]. The functionality of the JUNO purification plant is being tested at one of the detectors of the Daya Bay experiment. Moreover, OSIRIS (Online Scintillator Internal Radioactivity Investigation System), a LS 20 tons stand-alone detector, is planned to monitor the radiopurity of the LS before it enters the JUNO detector, in order to confirm the proper operations of the purification plant.

2.3 The energy and position reconstruction

In JUNO, the energy and position of each event will be determined respectively from the number of photons collected by the PMTs and by their arrival time on them.

The energy reconstruction is crucial to disentangle the signal from the backgrounds. In principle, the energy deposited by a particle interacting in a liquid scintillator is proportional to the number of photons collected by the PMTs. An electron with kinetic energy of 1 MeV is expected to produce approximately 1500 photoelectrons in the JUNO detector. However, the ionization quenching effect [58] introduces an intrinsic non-linear relation between the deposited energy E and the number of emitted photons Y_p^{ph}:

$$Y_p^{ph} = Y_0 \cdot E \cdot Q_p(E) \tag{2.2}$$

where $Q_p(E) < 1$ is called quenching factor. The suffix p recalls that $Q_p(E)$ and Y_p^{ph} depend on the particle type (α, β, γ) for a fixed energy. Y_0, equals to about 10^4 photons/MeV, is the scintillation light yield in absence of quenching (i.e. $Q_p(E) = 1$). The $Q_p(E)$ trend can be described by the Birks formula [58], but the values of its parameters need to be determined experimentally. Due to it, calibrations will be fundamental to compare the known internal source energies with the correspondent measured ones in photoelectrons. The quenching factor $Q_\beta(E)$ for β decay electrons or positrons can be obtained as:

$$Q_\beta(E) = \frac{1}{E}\int_0^E \frac{dE}{1 + kB \cdot \frac{dE}{dx}} \tag{2.3}$$

where $\frac{dE}{dx}$ is the specific energy loss and kB is the Birks quenching parameter, depending on the scintillator considered. The non-linear effect is more and more relevant as long as the energy deposit is below a few hundreds keV. The quenching effect for α particles with a few MeV of energy is higher, and consequently the amount of emitted light is reduced, by a factor of the order of ten with respect to an electron with the same energy.

On the other hand, the position reconstruction is used to define events inside a fiducial volume, which selects a region of the scintillator where the external background is minimized. Moreover, a good position reconstruction is crucial to take into account the light non-uniformities. These take place because, for a constant energy released in the scintillator, the expected amount of detected photons varies with the emission point of the photons themselves, due to the optical self absorption of the scintillator itself. The idea at the basis of the position reconstruction algorithms exploits the time distributions of the collected photons. Particularly, the positions are reconstructed with a photon time-of-flight method, where the coordinates $\vec{r}_0$ and t_0 of the event are obtained by maximizing the likelihood:

$$\mathcal{L}(\vec{r}_0, t_0|\vec{r}_i, t_i) = \prod_i \text{pdf}\left(t_i - t_0 - \frac{|\vec{r}_i - \vec{r}_0|}{v_g}\right) \tag{2.4}$$

where the index i runs over the triggered PMTs, t_i is the time of arrival of the photoelectron on the electronic channel and $\vec{r}_i$ is the position of the hit PMT and v_g is the group velocity of the wave packet emitted in the scintillation event. The pdf considered here is the probability density function for the time of transit of photons from the emission to the detection point.

To address the complex topic of both energy and position reconstruction, a common effort from the JUNO collaboration is being carried on to develop several and varied ideas about the variables to implement.

2.4 Background and methodology for its control

JUNO is affected by many sources of backgrounds, which in first approximation can be divided into two main categories: the cosmogenic backgrounds and the natural radioactivity. The former is caused by muons coming from cosmic rays and it is related to the experimental site location. Conversely, the natural radioactivity appears in all the materials and in the environment surrounding the detector and requires a careful plan to be minimized. Among the natural radioactivity it's important to distinguish between the *internal background*, coming from the LS itself, and the *external background*, coming from the other parts of the JUNO detector. The main radioactive contaminants are the following:

- Natural long-lived radionuclides ^{238}U and ^{232}Th (with their decay chains supposed to be at secular equilibrium) and ^{40}K;
- Natural medium-lived radionuclides ^{226}Ra, ^{210}Pb/^{210}Bi, ^{210}Po when secular equilibrium is broken in the ^{238}U chain;
- Natural gaseous radionuclide ^{222}Rn;
- Anthropogenic radionuclide ^{60}Co.

To achieve the JUNO physics goals, high levels of radiopurity are required. As an example, the maximum concentrations allowed for the ^{238}U and ^{232}Th chains to detect IBD are 10^{-15} g/g, but even stricter ones are necessary for other analysis, such as the solar neutrinos one (see Chapter 3).

Much effort is being made by the JUNO collaboration to reduce the backgrounds and increase the radiopurity of the detector [59]: a careful materials selection, environmental control and purification campaigns. The onion-like JUNO experimental design represents itself a way to reduce the cosmogenic and the external background, which can be further decreased through some software-based fiducial volume cuts. On the other hand, since the internal background is uniformly distributed in the LS, only a series of purifications of the LS itself can lead to a reduction of it. Particularly, the purification of LS will be performed with a system combining mainly distillation, water extraction and steam (or N_2 gas) stripping [57]. The distillation is used to remove form the raw LAB the heaviest impurities (mainly ^{238}U, ^{232}Th and ^{40}K) and the process is based on the heat and mass transfer between a liquid and a gas stream. Afterwards, the LS is processed through water extraction and stripping plants. The gas stripping is a separation process in which, one or more dissolved gases are removed from the liquid phase and transferred to the gas phase. For example, radioactive gases (mainly ^{85}Kr, ^{39}Ar and ^{222}Rn) and oxygen can be removed from the scintillator mixture by stripping it with a variable mixture of superheated steam and nitrogen.

CHAPTER 3

Solar neutrino signal and backgrounds

3.1 Solar neutrino signal

JUNO will detect solar neutrinos of all flavors by means of elastic scattering off LS electrons:

$$\nu_x + e^- \rightarrow \nu_x + e^- \qquad x = e, \mu, \tau \tag{3.1}$$

However, since ν_e interacts via both CC and NC, the scattering cross section for ν_e is ≈ 6 times larger than that for ν_μ and ν_τ. In this process, only a fraction of the neutrino energy is transferred to the electron, which recoils and transfers the gained kinetic energy to the LS. The visible energy ranges from zero to a fraction of the neutrino energy, equal to T_e^{max}, given by:

$$T_e^{max} = \frac{E_\nu}{1 + \frac{m_e c^2}{2E_\nu}} \tag{3.2}$$

The expected reconstructed energy spectra for ^{7}Be, *pep* and CNO neutrinos are shown in Fig. 3.1: even for monoenergetic neutrino sources, as ^{7}Be and *pep* neutrinos, the electron recoil spectrum is continuous.

The elastic scattering process has no intrinsic energy threshold. The expected interaction rate R for the reaction 3.1 in a given target is calculated as the product of the incoming neutrino flux Φ, the number of electrons in the target $N_e = 3.38 \cdot 10^{32}\,\mathrm{e^-/kton}$ [40], and the cross section σ_x for the elastic scattering, taking into account the survival probability P_{ee} of the electron neutrino. Mathematically, the rate is given by:

$$R = N_e \int \mathrm{d}E_\nu \frac{\mathrm{d}\Phi}{\mathrm{d}E_\nu} \int \mathrm{d}T \left[\frac{\mathrm{d}\sigma_e}{\mathrm{d}T} P_{ee}(E_\nu) + \frac{\mathrm{d}\sigma_{\mu,\tau}}{\mathrm{d}T} \left(1 - P_{ee}(E_\nu)\right) \right] \tag{3.3}$$

where E_ν is the neutrino energy and T is the energy of the scattered electron. The expected interaction rates (in cpd/kton) in JUNO for the neutrinos we are interested in, i.e. ^{7}Be, *pep* and CNO neutrinos, are reported in Table 3.1, while their spectra are shown in Fig. 3.1

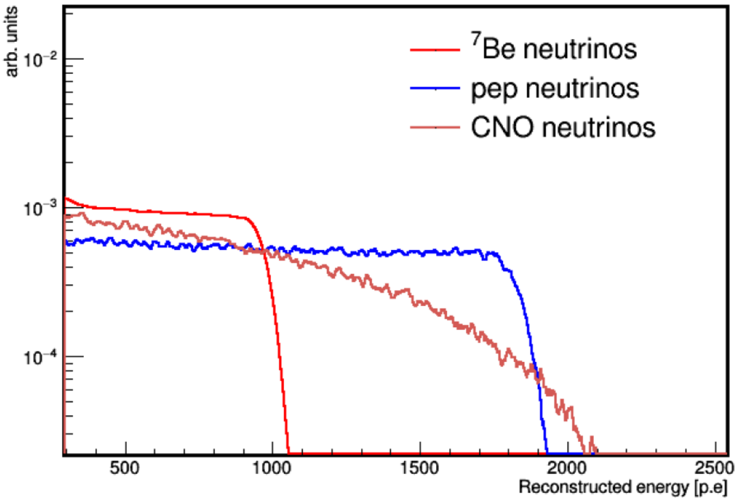

Figure 3.1: The expected reconstructed energy spectrum (in photoelectrons, p.e.) of recoiled electrons scattered off by solar neutrinos of intermediate energy (^{7}Be, *pep* and CNO) in JUNO. The spectrum of each solar neutrino is the probability density function from the Monte Carlo simulations. Other solar neutrino components are not shown as they are not of interest within this analysis.

Solar ν	R [cpd/kton]	
	HZ-SSM	LZ-SSM
^{7}Be	489.6 ± 28.6	446.65 ± 25.6
pep	28.0 ± 0.4	28.41 ± 0.4
CNO	50.29 ± 7.97	35.98 ± 5.31

Table 3.1: ^{7}Be, *pep* and CNO solar neutrino expected interaction rates in JUNO. Both HZ-SSM and LZ-SSM predictions are reported.

3.2 Intermediate energy solar neutrino backgrounds

The content of this section is widely based on Technote Ref. [60].

The scintillation events produced by both neutrinos and backgrounds cannot be disentangled on an event-by-event basis: the neutrino signature is intrinsically indistinguishable from β and γ radiation. Therefore, a high radiopurity is essential in order to make the measurement of intermediate energy solar neutrinos possible. As described more in detail in Chapter 4, the range of interest of our analysis is $0.4\,\text{MeV} < E_{vis} < 1.7\,\text{MeV}$ corresponding to 650 p.e. $-$ 2400 p.e..The backgrounds are divided into three categories: *internal*, *external* and *cosmogenic*. We will treat in a separate section the background from reactor antineutrinos.

Since the civil construction of the JUNO experiment has not been completed yet, we cannot know the actual and final contamination of the different isotopes. For the internal backgrounds, following the classification introduced in Ref. [38], we have conceived four different radiopurity scenarios: the *Borexino-like*, the *ideal*, the *baseline* and the *IBD*, in order of decreasing levels of radiopurity (see Section 3.2.1). The assumptions for the external background are taken from Ref. [40], while the cosmogenic ones originate from a scaling of rates from previous experiments, namely KamLAND and Borexino.

3.2.1 Internal backgrounds

By *internal backgrounds* we mean the presence of radioactive isotopes which contaminate the LS: they can be classified in three kinds of emitters: α, β and γ. As already mentioned above, we have four different scenarios for the concentration of the different isotopes.

The *IBD* scenario corresponds to the minimum radiopurity requirements set by the JUNO collaboration for a successful NMO determination [38]: in this case, the ^{238}U/^{232}Th contamination is $\approx 10^{-15}$ g/g, the ^{40}K contamination is $\approx 10^{-16}$ g/g, while ^{210}Pb is assumed to be out of equililbrium with respect to the ^{238}U chain, with a contamination at the level of $\approx 5 \cdot 10^{-23}$ g/g. The count rate of ^{85}Kr is assumed to be 5000 cpd/kton. The *baseline* scenario corresponds to a factor 10 of improvement for all isotopes with respect to the IBD. The *ideal* scenario corresponds to a factor 10 of improvement with respect to the baseline scenario for all the isotopes, except for ^{210}Pb and ^{85}Kr for which the improvement is only of a factor 5. Finally, the *Borexino-like* scenario represents a combination of BX-Phase II and BX-Phase III internal backgrounds contaminations [61, 36, 37].

The expected decay rates relevant for this analysis are quoted in Table 3.2. For most of the internal backgrounds of interest, the interaction rate R, expressed in counts per day per kilo-tonne of scintillator (cpd/kton), can be directly calculated as:

$$R\left[\frac{\text{cpd}}{\text{kton}}\right] = \frac{c \cdot N_A}{\tau \cdot M} \cdot 86400\,\frac{\text{s}}{\text{day}} \cdot 10^9\,\frac{\text{g}}{\text{kton}}, \tag{3.4}$$

where c [g/g] and $\tau = \tau_{1/2}/\ln 2$ [s] are the radioactive isotopic abundance per g of LS, and the mean lifetime, respectively. M is the element's molar mass [g/mol] while $N_A = 6.022 \times 10^{23}\,\text{mol}^{-1}$ is the Avogadro number.

In the following a list of the involved elements is made. It is worth pointing out that the low energy background associated to ^{14}C β decay is not considered here, since it doesn't enter into the analysis region of interest.

^{40}K

The ^{40}K isotope (β^- decay or EC, $\tau = 1.85 \times 10^9$ y) is a primordial nuclide with a natural abundance of 0.012%. In addition to the dominant pure β decay (B.R. = 89% and 1310 keV end–point, eq. 3.5a), there is a 10.7% probability for electron capture

Isotope	*Borexino-like*		*Ideal*		*Baseline*		*IBD*	
	c [g/g]	R [cpd/kton]	c [g/g]	R [cpd/kton]	c [g/g]	R [cpd/kton]	c [g/g]	R [cpd/kton]
^{40}K	–	4.20	$1 \cdot 10^{-18}$	23	$1 \cdot 10^{-17}$	229	$1 \cdot 10^{-16}$	2289
^{85}Kr	–	100	–	100	–	500	–	5000
^{232}Th chain	$5.7 \cdot 10^{-19}$	2.0	$1 \cdot 10^{-17}$	35	$1 \cdot 10^{-16}$	351	$1 \cdot 10^{-15}$	3508
^{238}U chain	$9.4 \cdot 10^{-20}$	1.414	$1 \cdot 10^{-17}$	150	$1 \cdot 10^{-16}$	1505	$1 \cdot 10^{-15}$	15047
^{210}Pb chain ‡	–	232	$1 \cdot 10^{-24}$	727	$5 \cdot 10^{-24}$	3626	$5 \cdot 10^{-23}$	36310

‡ Additional contribution assumed out-of-secular-equilibrium from the ^{238}U decay chain and identified as ^{210}Pb sub-chain: ^{210}Pb → ^{210}Bi → ^{210}Po.

Table 3.2: Expected internal background contributions for the intermediate energy solar neutrinos analysis. The ^{232}Th-chain and ^{238}U-chain contributions include the rate of every decay-chain daughters [60].

to an excited state of ^{40}Ar (eq. 3.5b), resulting in the emission of a monoenergetic 1460 keV γ ray (eq. 3.5c), which helps to distinguish the ^{40}K energy spectrum from the other β spectra. In JUNO, this isotope comes from several sources [38]: the rock around the detector hall, the SS sphere, the PMTs glass, LS and water buffer contaminations and the acrylic sphere.

$$\begin{aligned}
&{}^{40}\mathrm{K} \rightarrow {}^{40}\mathrm{Ca} + e^- + \overline{\nu}_e && \beta^- : \quad Q = 1.32\,\mathrm{MeV},\ \mathrm{B.R.} = 89.3\% && (3.5a)\\
&{}^{40}\mathrm{K} + \mathrm{e}^- \rightarrow {}^{40}\mathrm{Ar}^* + \nu_e && \mathrm{EC} : \quad Q = 1.50\,\mathrm{MeV},\ \mathrm{B.R.} = 10.7\% && (3.5b)\\
&{}^{40}\mathrm{K} + e^- \rightarrow {}^{40}\mathrm{Ar}^* \rightarrow {}^{40}\mathrm{Ar} + \gamma && \gamma : \quad E_\gamma = 1.46\,\mathrm{MeV} && (3.5c)
\end{aligned}$$

^{85}Kr

^{85}Kr is a β-emitter with a 687 keV end–point energy (99.57% B.R.) and a mean lifetime of 15.4 years. Since the distribution of the ^{85}Kr emitted electrons covers an energy range similar to the ^{7}Be neutrinos recoil electrons, ^{85}Kr is one of the most important backgrounds for the analysis presented in this work. We can find its presence of traces in the atmosphere, with an average concentration of $\sim 1\,\mathrm{Bq/m^3}$, mostly because of past nuclear explosions. Thus, even small air exposures of the LS during the detector-filling operations would yield significant contamination.

^{232}Th

The primordial isotope ^{232}Th has a mean lifetime of 2.03×10^{10} y and a natural abundance of 100%. As shown in Table 3.3, the ^{232}Th decay chain contains six α and four β decays and ends with the stable ^{212}Po.

While the ^{232}Th decay rate is also computed using eq. 3.4, the total ^{232}Th-chain decay rate is given by $10 \times R(^{232}\mathrm{Th})$. This assumes that the daughter isotopes of the ^{232}Th are in secular equilibrium with their respective parent.

^{238}U

^{238}U is a primordial radioactive isotope with a mean lifetime of 6.45×10^{9} y. It is the most common isotope of uranium, with a natural abundance of 99.3%. As shown in Table 3.4, the ^{238}U decay chain contains eight α and six β isotopes and ends with ^{206}Pb. Using the same argumentation as for ^{232}Th, the ^{238}U-chain decay rate is calculated to be $14 \times R(^{238}\mathrm{U})$.

Some of the isotopes of the radioactive ^{238}U chain can be also found out of equilibrium. In particular, the ^{210}Pb isotope, which can be absorbed by metal and plastic surfaces, gives rise to an additional out-of-equilibrium sub-chain, addressed in the following paragraph.

Isotope	Mean Lifetime	Energy [KeV]	Decay
^{232}Th	2.03×10^{10} y	4010	α
^{228}Ra	8.31 y	46	$\beta^-\ \gamma$
^{228}Ac	8.84 hrs	2140	$\beta^-\ \gamma$
^{228}Th	2.76 y	5520	α
^{224}Ra	5.28 days	5690	α
^{220}Rn	80.2 s	6290	α
^{216}Po	209 ms	6780	α
^{212}Pb	15.3 hrs	573	$\beta^-\ \gamma$
^{212}Bi(64%)	87.4 min	2250	α
^{212}Bi(36%)	87.4 min	6050	α
^{212}Po	431 ns	8780	α
^{208}Tl	4.40 min	4990	$\beta^-\ \gamma$

Table 3.3: The ^{232}Th decay chain showing isotope, lifetimes, maximum released energies and type of decay.

^{210}Pb sub-chain: ^{210}Pb – ^{210}Bi – ^{210}Po

^{210}Pb is a β-emitter nuclide in the ^{238}U decay chain. Due to its long mean lifetime (32 years) and its tendency to grab at surfaces, it is often found out of secular equilibrium with the ^{222}Rn section of the chain [61].
While the additional ^{210}Pb contribution is not a problem, since its end–point energy (Q = 63.5 keV) is well below the region of interest for solar neutrinos, its daughters ^{210}Bi and ^{210}Po represent a major source of background.

In this case, we can consider the additional ^{210}Pb as the parent of the following decay sub-chain:

$$^{210}\text{Pb} \xrightarrow[Q=63.5\,\text{keV}]{\tau\approx 32\,\text{y}} {}^{210}\text{Bi} \xrightarrow[Q=1160\,\text{keV}]{\tau=7.23\,\text{d}} {}^{210}\text{Po} \xrightarrow[Q=5.4\,\text{MeV}]{\tau=199.1\,\text{d}} {}^{206}\text{Pb} \tag{3.6}$$

- ^{210}Bi is a β-emitting nuclide with a mean lifetime of 7.23 days and a Q–value of 1160 keV. In JUNO, the ^{210}Bi energy shape doesn't have any prominent structure but a smooth featureless profile instead, similar to the one of CNO and *pep* neutrinos.

- ^{210}Po is a 5.3 MeV α emitter. Because of quenching effects, its reconstructed energy is found around 510 keV electron equivalent energy, and therefore its spectrum extends in the typical ^{7}Be neutrino energy region. It will be clearly visible in the JUNO energy spectrum thanks to its peak-shape.

Provided that we know that there is an out-of-secular-equilibrium ^{210}Pb component, its rate can be computed via eq. 3.4. Because of its mean lifetime ($\tau_{\text{Bi}} = 7.23$ d)

Isotope	Mean Lifetime	Energy [keV]	Decay
^{238}U	6.45×10^9 y	4200	α
^{234}Th	34.8 days	199	β^-
^{234m}Pa	1.70 min	2290	β^-
^{234}U	3.53×10^5 y	4770	α
^{230}Th	1.15×10^5 y	4690	α
^{226}Ra	2.30×10^3 y	4790	α
^{222}Rn	5.51 days	5490	α
^{218}Po	4.40 min	6000	α
^{214}Pb	38.7 min	1020	$\beta^-\ \gamma$
^{214}Bi	28.4 min	3270	$\beta^-\ \gamma$
^{214}Po	236 s	7690	α
^{210}Pb	32.2 y	63	$\beta^-\ \gamma$
^{210}Bi	7.23 days	1160	$\beta^-\ \gamma$
^{210}Po	200 days	5419	α
^{206}Pb	stable	–	–

Table 3.4: The ^{238}U decay chain showing isotope, lifetimes, maximum released energies and type of decay.

small with respect to the one of ^{210}Pb ($\tau_{\text{Pb}} = 32\,\text{y}$), the ^{210}Bi activity goes almost immediately in equilibrium with the ^{210}Pb one, while ^{210}Po reaches equilibrium after $\sim 2\,\text{y}$. Once the equilibrium is reached, the following relation between the rates of the three isotopes holds:

$$\tau_{\text{Pb}} \gg \tau_{\text{Bi}} \qquad \tau_{\text{Pb}} \gg \tau_{\text{Po}} \quad \overset{t/\tau_{\text{Po}} \gg 1}{\Longrightarrow} \quad \frac{R_{\text{Po}}}{R_{\text{Bi}}} = \frac{R_{\text{Po}}}{R_{\text{Pb}}} = \frac{\tau_{\text{Pb}}}{\tau_{\text{Pb}} - \tau_{\text{Po}}} \approx 1.015 \tag{3.7}$$

Out-of-secular-equilibrium ^{210}Po

From the Borexino experience, we know that it is possible that a certain amount of ^{210}Po out-of-secular-equilibrium with respect to both the ^{238}U and the ^{210}Pb chains appears in the LS. From now on, we will call it *unsupported ^{210}Po*. In Borexino LS, a large amount of unsupported ^{210}Po was found immediately after the filling [61, 36], probably because it was washed out from the pipes' surface while the scintillator was flowing into them. In Borexino, another source of unsupported ^{210}Po was the nylon vessel containing the scintillator: ^{210}Po produced by ^{210}Pb, implanted on the surface, was cleaned and carried into the fiducial volume by convective currents triggered by temperature changes [37]. Currently, we cannot estimate the amount of unsupported ^{210}Po which will be present in the JUNO scintillator – if any – once the experiment will be working. Hence, we will set its value to zero and we will investigate the impact of different contaminations in the Chapter **??**.

3.2.2 External backgrounds

The main source of external background is the radioactivity of the materials surrounding the LS, mainly the ^{208}Tl, ^{214}Bi, and ^{40}K isotopes coming from the PMTs glass. Only the emitted γ rays have a high enough mean free path to reach the inner parts of the scintillator and their typical energy belongs to the 1 MeV to 3 MeV range. We assume that the external γ background can be removed with an offline fiducial volume cut. Since the JUNO scintillator volume is extremely large, one can demonstrate that it's always possible to implement strict enough cuts into the cleanest region of the detector; therefore, the external background need not to be considered in our analysis. In fact, as Fig. 3.2 illustrates, the Monte Carlo simulations of the external γ's deposited energy spectrum in the LS show that a $r \lesssim 15\,\text{m}$ spherical FV would be large enough to completely suppress the external γ contributions.

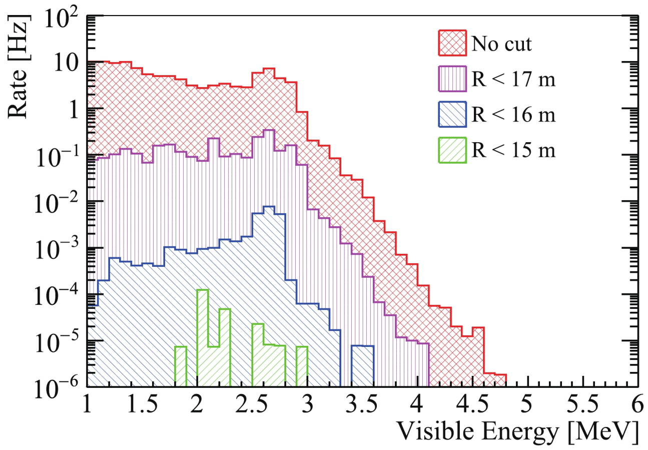

Figure 3.2: Deposited energy spectra in LS by external γ's after different FV cuts. The plot is generated by the simulation with measured radioactivity values of all external components [40].

3.2.3 Cosmogenic backgrounds

Cosmogenic isotopes are created by spallation of atmospheric muons on carbon atoms inside the LS. Many of them are short-lived isotopes and can be efficiently removed by a simple veto cut around the muon track; others are long-lived (with mean lifetimes $\approx$ s, min) and their decays represent an additional constant source of background.

For the intermediate energy solar neutrinos analysis in JUNO, the four relevant cosmogenic isotopes are ^{11}C, ^{10}C, ^{6}He and ^{11}Be: they decay with non-negligible rates in the energy region of interest [62, 63]. Let's now describe them more in detail.

- ^{11}C is a β^+ emitter (Q = 1.98 MeV) with a mean lifetime of 29.4 min. It is by far the most abundant and relevant μ-induced nuclide for our analysis, representing the main background for the *pep* and CNO neutrino rates determination. Typically, it is produced along with one neutron from the interaction of a cosmic muon with a carbon atom:

  $$\mu + {}^{12}\mathrm{C} \rightarrow \mu + {}^{11}\mathrm{C} + n \tag{3.8}$$

  Then, it undergoes a β^+ decay, producing ^{11}B atoms:

  $${}^{11}\mathrm{C} \rightarrow {}^{11}\mathrm{B} + e^+ + \nu_e \tag{3.9}$$

  The resulting ^{11}C energy spectrum is found to be in the same energy range of *pep* and CNO neutrino spectra, making this background crucial for our analysis.

- ^{10}C is a β^+ emitter (Q = 3.65 MeV) with a mean lifetime of 27.8 s. Its energy spectrum lies in the region above 1.4 MeV, thus its contribution is marginal in the region of interest of intermediate energy solar neutrinos.

- ^{6}He is a β^- emitter (Q = 3.51 MeV) with a mean lifetime of 1.1 s. As shown in Table 3.5, its low expected rate makes its contribution negligible with respect to ^{11}C.

- ^{11}Be is a β^- emitter (Q = 11.5 MeV) with a mean lifetime of 19.9 s. Since its spectrum lies mostly in the higher energy range, it is only relevant to ^{8}B and *hep* neutrino analysis [40, 64]. Additionally its production rate is expected to be much lower than the other isotopes.

Isotope	Rate [cpd/kton]
^{11}C	1916 ± 157
^{10}C	37.1 ± 5.3
^{6}He	27.8 ± 4.8
^{11}Be	2.45 ± 0.61

Table 3.5: Expected interaction rates of cosmogenic backgrounds in JUNO [60].

The spallation reaction allows us to exploit the so-called *Three-Fold-Coincidence* (TFC) [65] algorithms to highly reduce the background. However, the remaining cosmogenic rate – primarily from ^{11}C – is still high enough to significantly affect the analysis. TFC algorithms and their performances will be discussed in Chapter 4. The JUNO expected cosmogenic rates are reported in Table 3.5.

The TFC algorithm

^{11}C isotope is the most important muon-induced cosmogenic background in JUNO. Whilst it is not so problematic for the determination of ^{7}Be neutrinos flux since the two energy spectra don't overlap, it represents a major background for the measurement of the interaction rate of *pep* and CNO neutrinos. In fact, the higher energy portion of the signal induced by *pep* and CNO neutrinos largely superimposes with its spectrum and its rate is $\approx$ 35 and $\approx$ 68 times higher than the CNO and *pep* ones, respectively.

Since new ^{11}C atoms are continuously created by the spallation processes of cosmic-ray muons on carbon atoms from the scintillator, the ^{11}C concentration cannot be reduced through purification campaigns, as it is allowed for other backgrounds. Fortunately, both its production and decay involve the emission of a neutron and a positron, respectively (see eq. 3.8 and eq. 3.9). It is therefore possible to exploit the spatial and time coincidence of those reactions, and identify the ^{11}C events through a *Three-Fold-Coincidence* (TFC) tagging technique. This technique has been developed and successfully used in all Borexino analysis [65, 36] and it would be even more crucial for JUNO, since the latter is subjected to a higher cosmic-muons rate than Borexino. Nonetheless, up to now, no methods devoted to ^{11}C-tagging have been yet developed specifically for the JUNO experiment. Our analysis is built on the assumption that the TFC algorithm will be implemented before the beginning of the data acquisition and that its performance will be comparable to the Borexino ones.

In the following, I will give an outline of the hypothetical TFC major steps. The mean life of ^{11}C ($\tau_{^{11}\mathrm{C}} \approx 27$ min) is too long to apply a veto on the whole detector for every muon passes through it. Therefore, the ^{11}C contamination has to be removed with a more sophisticated approach. The TFC algorithm idea is to veto space-time regions of the detector after the coincidences between the neutron capture and the parent muon, in order to exclude the subsequent ^{11}C decay. The vetoed spatial regions could be either spherical or cylindrical depending on the details of the algorithm implementation. A schematic depiction of the TFC algorithm vetoed regions implemented as in Borexino is shown in Fig. 3.3. The reconstruction of the interaction positions of the γ-rays from neutron capture and the tracks of parent muons are crucial for the success of the TFC technique. The guiding principle for the determination of the most appropriate parameters is the search for the optimal compromise between ^{11}C rejection and preservation of the residual exposure after the veto cuts.

The performances of a possible algorithm can be summarized in an effective way by two parameters:

- *Tagging Power* (TP), defined as the fraction of correctly identified ^{11}C events;

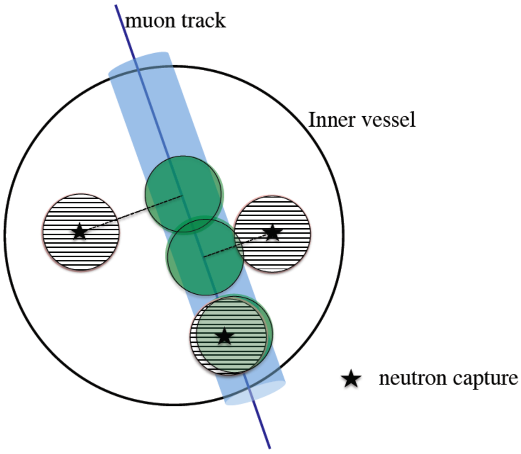

Figure 3.3: The spatial regions vetoed in Borexino TFC algorithm: a cylinder around the muon track (blue) and some examples of spheres centered around the point where the neutron capture is reconstructed (areas with horizontal lines around the stars) and their projections along the muon track (green areas) [65].

TP = 1.0 means that all the ^{11}C events are properly determined.

- *Subtracted dataset exposure* (SE), representing the remaining exposure in the TFC-subtracted dataset after the application of TFC; SE = 1.0 means that the whole exposure belongs to the TFC-subtracted dataset, while the TFC-tagged one is empty.

Since no preliminary studies about this topic are available for JUNO, in our analysis reasonable values of these two parameters (TP = 0.90 and SE = 0.70) have been chosen as default working values based on Borexino experience [36].

3.2.4 Background from reactor antineutrinos

Reactor antineutrinos that interact through the elastic scattering off electrons contribute as a background in the intermediate energy region of solar neutrinos.

In order to estimate their interaction rate, the $\overline{\nu}_e$ spectrum from Ref. [66] is used. Then, considering 36 GW of reactors thermal power and a baseline of 53 km, the flux of reactor antineutrinos in the JUNO detector is calculated to be $\approx 2 \times 10^7\,\mathrm{cm}^{-2}\mathrm{s}^{-1}$. Considering the antineutrinos cross section for the elastic scattering off electrons [40] and the survival probability of reactor antineutrinos [38] with oscillation parameters [7], the rate of background events induced by antineutrinos is calculated to be 1.86 cpd/kton in the entire energy range and 1.7 cpd/kton for visible energy $\mathrm{E}_{\mathrm{vis}} < 2\,\mathrm{MeV}$.

When comparing this rate with the expected rate of solar neutrinos (Sec.3.1) and the radioactive and cosmogenic backgrounds, the contribution from antineutrinos can be considered negligible. Therefore, we will not include it in our sensitivity studies.

3.2.5 Background from pileup events

A so-called *pileup* event takes place when two or more events occur so close in time that a clustering algorithm cannot disentangle them. Pileup events represent a critical background for the low energy analysis, typically in the energy range of *pp* neutrinos, and should be studied carefully. However, in principle, the pileup events could affect also the intermediate energy region: a scrupulous analysis of its effect is described in the Technote Ref. [60]. The results reported in [60] prove that pileup events are mostly negligible, so that we can safely neglect it in the intermediate energy analysis.

To get more into the details, the following pileup scenarios have been studied. First of all, since ^{14}C is the most abundant isotope in liquid scintillator detectors, the pileup of two, three or four ^{14}C events (*double* ^{14}C pileup, *triple* ^{14}C pileup and *quadruple* ^{14}C pileup, respectively) has been considered. Furthermore, because of ^{210}Po is one of the most abundant isotope expected in the lowest part of the energy spectrum of this analysis, a possible pileup of ^{14}C and ^{210}Po events has also been studied. The results obtained are summarized below.

- *Double ^{14}C pileup*: it is not present in the region of interest of the intermediate energy solar neutrinos analysis.
- *Triple ^{14}C pileup*: only a fraction of events of $\approx 2 \cdot 10^{-6}$ % contributes within the energy region of interest.
- *Quadruple ^{14}C pileup*: it doesn't impact on *pep-ν* sensitivity, while it worsens the ^{7}Be-ν sensitivity of $\approx 1\,\% - 1.5\,\%$. However, if constrained in the fit (see Chapter 4), its impact is negligible.
- *^{14}C + ^{210}Po pileup*: it doesn't impact on *pep-ν* sensitivity, while it worsens the ^{7}Be-ν sensitivity of $\approx 1\,\% - 1.13\,\%$. As in the previous case, if constrained in the fit, its impact is negligible.

CHAPTER 4

Analysis strategy for ^{7}Be, *pep* and CNO solar neutrinos detection

Thanks to its exceptional energy resolution and its large active mass, JUNO represents an excellent candidate to investigate solar neutrinos. Particularly, in this thesis work I will focus on its potentiality to detect ^{7}Be, *pep* and CNO solar neutrinos, the so-called intermediate energy solar neutrinos.

Since JUNO has not started yet to take data, the purpose of the analysis I am going to illustrate is to evaluate its sensitivity to solar neutrinos. To perform as comprehensive sensitivity studies as possible, the results have been obtained as a function of different radiopurity concentrations and different exposures; this allows us to optimize the analysis before the data-taking starts.

In liquid scintillator detectors, the signal induced by solar neutrinos which scatter on electrons is generally indistinguishable on an event-by-event basis from the one produced by radioactive backgrounds. However, it's possible to extract the neutrino signal by means of a fit to the energy distribution of all events. To achieve this, it's necessary to know the expected reconstructed energy distributions of each signal and background component, giving them in input to the fit. These distributions can be attained only if the detector energy response is known very precisely and can be simulated via the JUNO Monte Carlo software. Then, the fit returns in output the corresponding contributing amplitude for each species, i.e. the number of events whereby each contributes to the total events.

4.1 Strategy steps

The main steps of the analysis strategy are sketched in Fig. 4.1 and are summarized hereafter:

1. **Monte Carlo production.** Monte Carlo simulations of neutrino signals and backgrounds are performed with the JUNO offline software framework, called SNiPER and described in Section 4.2.

2. **PDF production.** As a first step, for each of the species of interest, a *Probability Density Function* (PDF) for the reconstructed energy variable can be built directly from the corresponding Monte Carlo sample, as explained in Sec. 4.3.

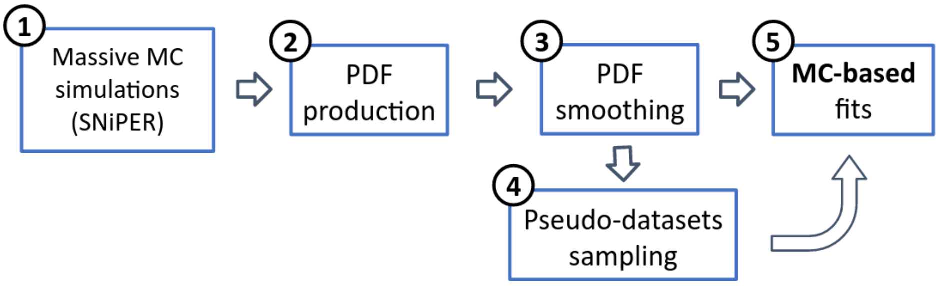

Figure 4.1: Flow chart describing the steps of the sensitivity analysis on intermediate energy solar neutrinos.

These PDFs, both for neutrinos and backgrounds, will be used as the model against which the pseudo-dataset will be both sampled and fitted.

3. **PDF smoothing.** Given the JUNO exposure with respect to previous experiments, e.g. Borexino, a groundbreaking amount of statistic is expected once data will start to be collected. Because of obvious limited computational resources, the generated PDFs, which in principle should be produced with greater statistics than the expected data, cannot actually afford it. In the fitting process this would lead to the phenomenon of oversampling, i.e. we would artificially reproduce the PDFs statistical fluctuations, amplifying them on datasets. This issue, addressed in Sec. 4.4, is solved by applying a Savitzky Golay filter [67] on the PDFs – thereby suppressing high-frequency fluctuations in the PDFs and reducing bias on the results.

4. **Pseudo-datasets generation.** These PDFs are then used to create all the necessary pseudo-datasets, created by randomly sampling from the PDFs. For each dataset, a random number is generated according to the mean expected number of events for each species, following a Poisson distribution. The samples from each PDF are then combined into one histogram: the pseudo-dataset. Sec. 4.5 explains this more thoroughly.

5. **MC based multivariate fit.** Since the cosmogenic isotope ^{11}C is characterized by a high rate in the detector and shares the energy region with *pep* and CNO neutrinos, it's of utmost importance to adopt techniques dedicated to its identification. We embraced the *Three-Fold-Coincidence* (TFC) tagging algorithm, described in Chapter 3. Thanks to it, we can split the JUNO solar neutrino dataset into two distinct data samples, simultaneously fitted: one enriched in ^{11}C (*TFC-tagged*) and the complementary one depleted in ^{11}C (*TFC-subtracted*), whose benefit will be discussed in Section 4.6. The fit approach requires the optimization of a binned Poisson likelihood function, to extract the interaction rates of each background and neutrino signal, assuming the same detector response function for data and model. In order to perform the fit, two fitting tools have been developed independently from each

other: MUST (Milano nUsol Sensitivity Tool) and JUST (Jülich nUsol Sensitivity Tool), described more in detail in Section 4.6.

6. **Fit of a large number of pseudo-datasets**. In order to extract the sensitivity of JUNO to intermediate energy solar neutrinos, for each defined experimental conditions, the fit must be performed on a large number of pseudo-datasets ($\approx 10^4$). From these ones, we then determine the average extracted rates for signal and background and the corresponding average uncertainty.

4.2 Monte Carlo simulation and events reconstruction framework

For the simulations and the analysis of the events, the JUNO experiment uses a software based on the *Software for Non-collider Physics expERiments* (SNiPER) framework [68], which in turn makes use of the Geant4 [69] and the ROOT [70] libraries. The Python language is used for the implementation of a user-interface which then calls C++ plug-ins. As the development of the JUNO software is ongoing, some technical details of the simulation are expected to evolve in time.

The event handling of the JUNO software is based on a multi-staged approach. The main steps of the SNiPER Monte Carlo procedure are sketched in Fig. 4.2 and described henceforward.

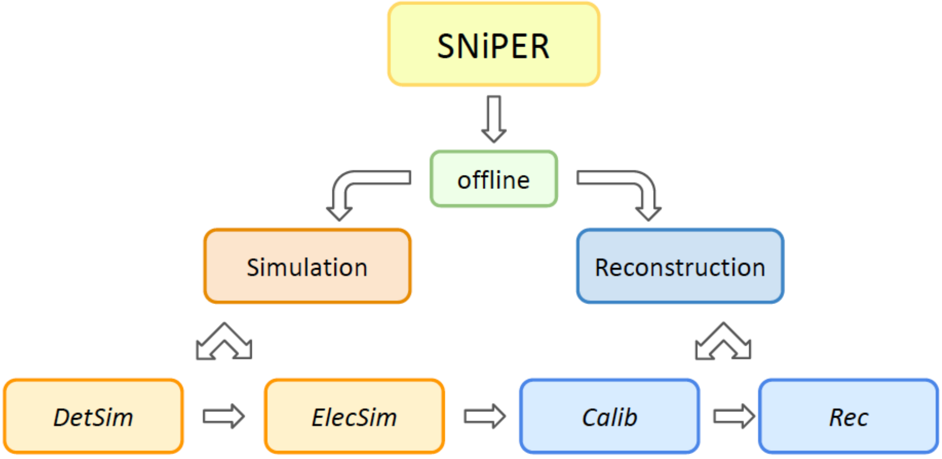

Figure 4.2: Schematic depiction of the Monte Carlo simulations main steps.

The offline JUNO Monte Carlo is an *ab initio* framework which simulates all the physical processes that can happen when a particle interact with the detector itself. After this first *simulation* part, the *reconstruction* part takes care of the analysis of the PMTs outputs and the reconstruction of the physical quantities of interest, such as the energy or the vertex interaction of the events. More in detail, as Fig. 4.2 shows, we have a total of four input-output chain modules: two concerning the simulation

– the so-called *DetSim* and *ElecSim* – and two related to the reconstruction one, the so-called *Calib* and *Rec*.

1. *DetSim* produces the list of the particles to be simulated and reproduces the detector;
2. *ElecSim* reproduces the electronics simulation and mimics the behaviour of the PMT readout electronics. Its output consists in the so-called *waveforms*, i.e. the time evolution of the detected PMT signals;
3. *Calib* reconstructs the charge and the time from each PMT waveform, through a de-convolution of them.
4. *Rec* takes the PMT charge and hit times as inputs and estimates the basic physical quantities associated to the event, such as the event vertex interaction, its energy or the particle identity.

The event energy reconstruction is carried out by using the OMILREC [71] (Optical Model Independent Likelihood REConstruction) algorithm, which implements a charge and time based Maximum Likelihood Estimation (QTMLE). The energy variable of interest for our analysis, named m_{NQE}, is the total number of charge in each PMT, expressed as the number of photoelectrons (p.e.), subtracted by the mean dark noise hits expected, and after an effective correction taking into account the non-uniformity of the detector energy response. Fig. 4.3 shows, as an example, the relation between m_{NQE} and the true deposited energy in MeV (left panel) and between m_{NQE} and the radius (right panel). Both the plots have been obtained by simulated 4000 events of 1 MeV electron homogeneously distributed in the detector within a radius of 15 m. As expected, 1 MeV approximately corresponds to 1500 p.e..

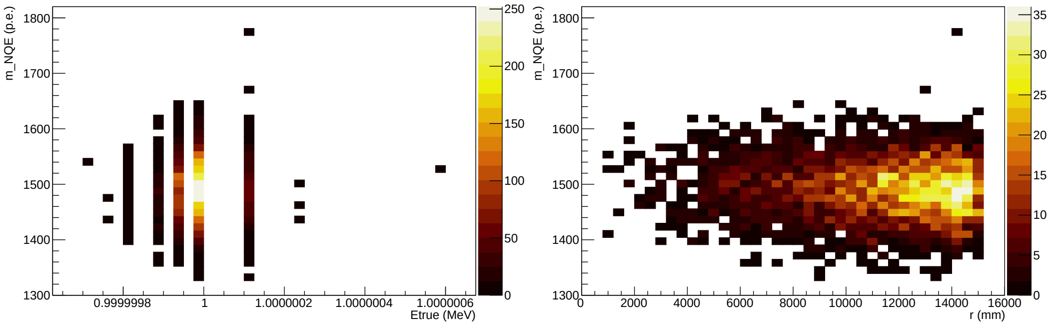

Figure 4.3: The m_{NQE} energy variable in p.e. versus the true deposited energy in MeV (left panel) and versus the radius in mm (right panel).

The non-uniformity effects happen mainly due to the optical self-absorption within the scintillator. In fact, if an event takes place near the detector edges, some of its scintillation photons cross the entire diameter of the acrylic sphere. By doing so, they are on average attenuated by the scintillator more than photons emitted to an event occurred in the centre of the detector, since these latter ones travel a shorter distance within the scintillator whose attenuation lenght is about 430 nm [72]. As a consequence, if the non-uniformity corrections weren't taken into account, then in the first example the reconstructed energy would be inferior with respect to the true deposited one. Because of that, an accurate reconstruction of the position of the event is crucial to correct for these non-uniformities.

The position reconstruction is based on the RecTimeLikeAlg [73] algorithm, which mainly uses the time information to reconstruct the time and the vertex for point-like events. The basic principles underlying these algorithm are described in Chapter 2.3.

4.3 Monte Carlo campaign and PDF production

In order to perform our sensitivity studies, a dedicated and extensive Monte Carlo simulation campaign is required. In particular, we need to generate the PDFs for all the species − both neutrinos and backgrounds − involved in the analysis.

The creation of the PDFs follows different steps, described hereafter. First of all, for each species of interest, for a given *i*-th species we simulate a number of events N_i^{gen} given by:

$$N_i^{\text{gen}} = R_i\,\mathcal{E} \qquad\qquad \mathcal{E} = m_{\text{FV}}\,\Delta t = \frac{4}{3}\pi r_{\text{FV}}^3\,\rho_{\text{LAB}}\,\Delta t \tag{4.1}$$

where R_i is the *i*-th species simulated rate (based on HZ-SSM predictions for neutrinos, and on baseline scenario for internal backgrounds), $\mathcal{E}$ is the exposure for a sphere with radius $r = 15.0\,\text{m}$ in a $\Delta t = 1\,\text{y}$ data taking with 100% duty cycle, and $\rho_{\text{LAB}} = 0.859\,\text{g/ml}$ is the scintillator density. All the species have been simulated uniformly within a $r_{\text{sim}} < 15.0\,\text{m}$ sphere, while the fiducial volume employed for this sensitivity analysis is a $r_{\text{FV}} < 14.0\,\text{m}$. As an example, assuming a $r_{\text{FV}} < 14\,\text{m}$ FV and 1 year of data-taking, JUNO is expected to detect $\sim 2 \times 10^6$ ^{7}Be neutrino events and $\sim 7 \times 10^6$ ^{11}C events. The value of r_{sim} has been chosen to avoid border effect in the position reconstruction of events. Since the radial coordinate resolution is $\sigma_r \sim 15\,\text{cm}$ for events with the lowest energy of interest for our analysis (650 p.e.), the probability that an event generated in $r > r_{\text{sim}}$ region is reconstructed inside the FV is negligible.

Afterwards, the histograms of the reconstructed energy are created in the m_{NQE} variable and the normalization stage is carried out, according to the considered fiducial volume and the detection efficiency for the given species. In light of that, the normalization factor $\mathscr{N}$ is computed as:

$$\mathscr{N} = \frac{N_i^{\text{rec}}(r < 14\,\text{m})}{N_i^{\text{gen}}(r < 14\,\text{m})} = \frac{N_i^{\text{rec}}(r < 14\,\text{m})}{N_i^{\text{gen}}(r < 15\,\text{m})} \cdot \left(\frac{15}{14}\right)^3 \tag{4.2}$$

where N_i^{rec} is the number of reconstructed events in a given spherical volume for a given species.

4.4 PDF smoothing

JUNO will benefit from an unprecedented target mass, consequently the data-taking exposure and the number of signal and background events will be extremely large. Currently, due to the disk storage and CPU time limits, it's unfeasible to simulate more than $\sim 1 \times 10^6$ Monte Carlo events for each species. Consequently, the number of simulated events is lower with respect to what expected for a real dataset. This could cause a bias in the fit result, due to the statistical fluctuations in the PDFs. For a realistic dataset, the following relation should be valid:

$$\lambda_{i+1} - \lambda_i \lesssim \sqrt{\lambda_i} \tag{4.3}$$

where λ_i is the expected number of events for the i-th reconstructed energy bin. To solve this issue and to verify eq. 4.3, an optimized low-pass filter, the so-called *Savitzky Golay (SG) filter* [67], is applied on the generated PDFs, thereby suppressing as possible the spectral high-frequency fluctuations without distorting the spectral features. The core of the SG filter is the fit of successive sub-sets of adjacent data points with a low-degree polynomial, by the method of linear least squares. The input parameters are the smoothing window length and the interpolating polynomial degree. The algorithm weakens the fluctuations of a factor 10-20 with respect to the starting PDFs[1].

The initial PDFs (left panel) and the ones after the smoothing (right panel) are displayed in Fig. 4.4.

4.5 Toy dataset generation

After the PDFs smoothing, the pseudo-datasets can be built by summing the contributions of each of the neutrino and background species. The reconstructed energy of the events is sampled from the PDFs and distributed in two different reconstructed energy spectra: the so-called *TFC-subtracted* histogram, which was depleted in ^{11}C using the TFC technique (see Sec. 3), and the *TFC-tagged* one, enriched in ^{11}C.

The two resulting histograms will be separately fitted in the multivariate analysis, as will be described in Sec. 4.6. Examples of reconstructed energy spectra for pseudo-datasets employed for the sensitivity analysis (black curves), assuming one year of data-taking, are shown in Fig. 4.5. The contributions of neutrinos and backgrounds are drawn in other colors. The TFC-subtracted and TFC-tagged datasets

---

[1] It's worth emphasizing that, in place of a Monte Carlo procedure, an analytical fit would avoid the smoothing step: in fact, the PDFs would be produced starting from the energy response function of the detector, derived analytically.

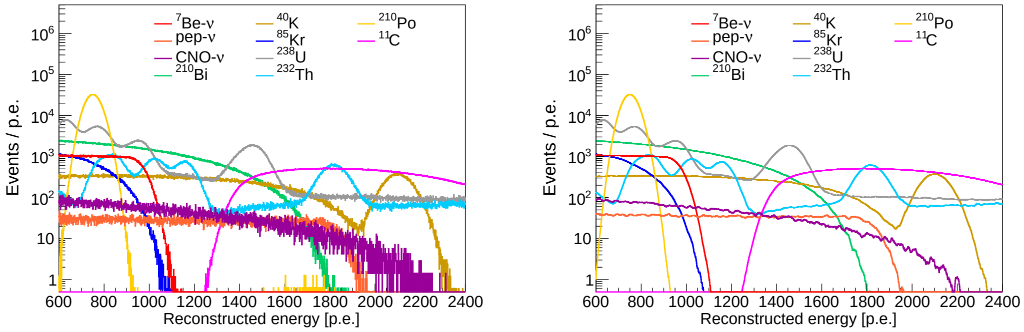

(a) *Before smoothing application*

(b) *After smoothing application*

Figure 4.4: The reconstructed energy PDFs before (left panel) and after (right panel) the smoothing process according to the SG algorithm, scaled for the respective expected number of events for 1 year data taking. The baseline scenario is assumed for internal background rates.

are reported in the left and right columns respectively; top panels, central panels and bottom panels refer to IBD, baseline, and ideal internal radioactivity scenarios respectively.

In order to highlight some important features of the datasets, as an example, we will focus now on the bottom panel of Fig. 4.5, representing the Borexino-like scenario. First of all, we want to underline the differences between the TFC-subtracted (left panel) and the TFC-tagged datasets (right panel).

The ^{11}C bump is more relevant in the former than in the latter, as expected thanks to the TFC action. The impact of other cosmogenic isotopes – ^{10}C and ^{6}He – can be neglected in the TFC-subtracted spectrum since their contribution is extremely low.

For what concern the properties of a single dataset, moving from the lower energy to the higher one, we find the features described below. At $\approx$ 1000 p.e.[2] we find the peculiar ^{7}Be Compton edge which superimposes one of the multiple ^{238}U chain α-peaks. The ^{232}Th chain exhibits various α-peaks as well, all along the energy range of interest. At $\approx$ 750 p.e. we have the well-recognizable ^{210}Po α-peak. The identification of these peaks can be further improved thanks to particle identification techniques [74]. Moreover, with an endpoint at $\approx$ 1100 p.e., we find the ^{85}Kr anonymous shape, with no specific details helping the fit to recognize it.

At higher energy, the spectrum is widely dominated by the ^{11}C background, whose energy spectrum starts at $\approx$ 1200 p.e.. All along the energy region of interest, we find the *pep*-ν and the CNO-ν spectra as well as the similar ^{210}Bi background spectrum shape. Finally, we have the ^{40}K contribution, whose γ emission peak at $\approx$ 2100 p.e. helps the fit to distinguish its spectrum from the other pure β spectra.

On the other hand, for what concerns the differences between the disparate radiopurity scenarios, by moving from the bottom panels to the centrals and top

---

[2] Reminding that 1000 p.e. $\approx$ 860 keV.

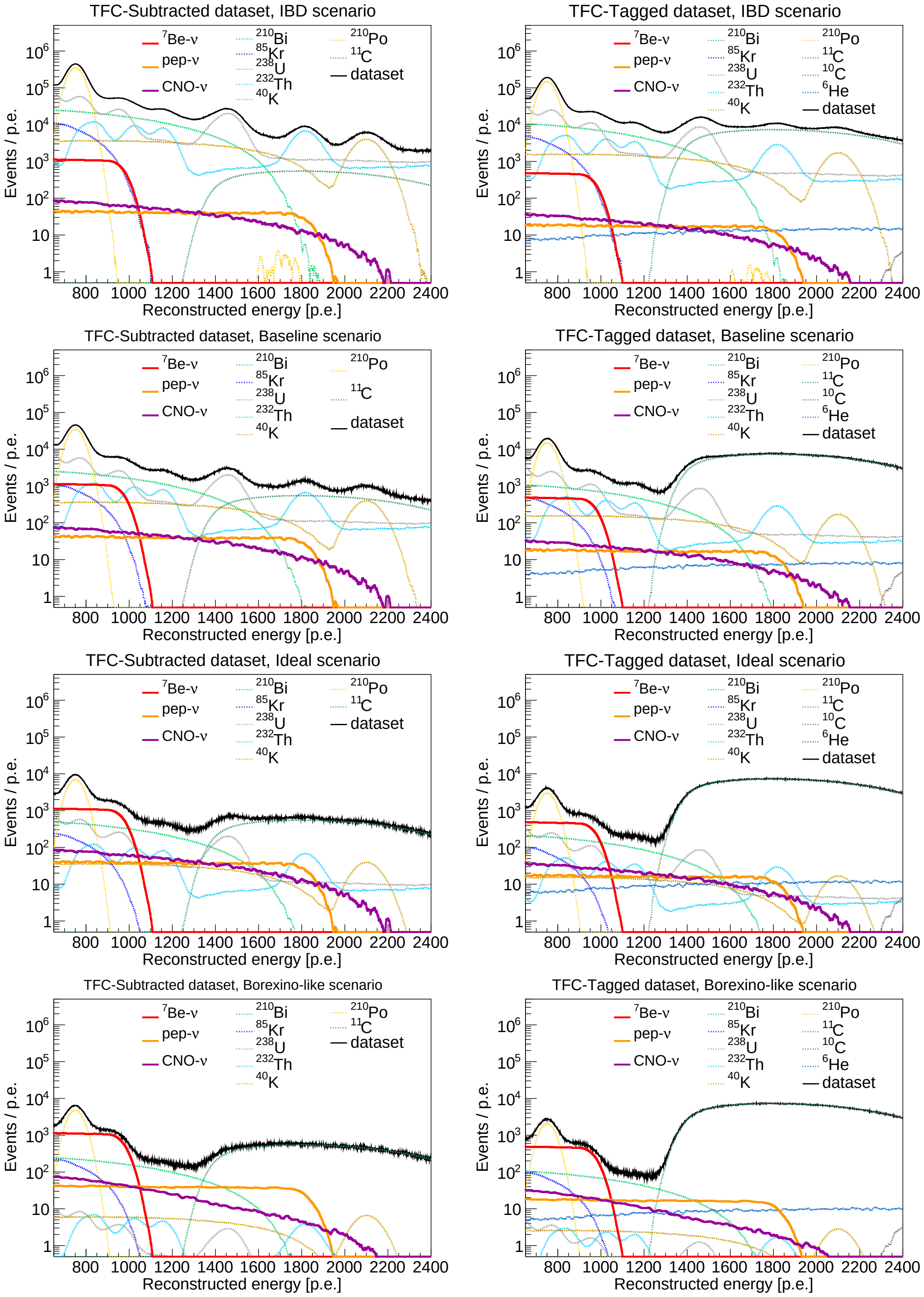

TFC-Subtracted dataset, IBD scenario

TFC-Tagged dataset, IBD scenario

TFC-Subtracted dataset, Baseline scenario

TFC-Tagged dataset, Baseline scenario

TFC-Subtracted dataset, Ideal scenario

TFC-Tagged dataset, Ideal scenario

TFC-Subtracted dataset, Borexino-like scenario

TFC-Tagged dataset, Borexino-like scenario

Figure 4.5: Example of reconstructed energy spectra for pseudo-datasets employed for the sensitivity analysis (black curves) and the isolated contributions of neutrinos and backgrounds (other colors), assuming one year of data-taking. The TFC-subtracted and TFC-tagged datasets are reported in the left and right columns respectively; top panels, top-central panels, bottom-central panels and bottom panels refer to IBD, baseline, ideal and Borexino-like internal radioactivity scenario respectively. The TFC algorithm parameters are TP = 0.90 and SE = 0.70.

ones, i.e. from the Borexino-like to ideal, baseline and IBD scenario, one can observe an increase in the internal backgrounds levels, while neutrinos and ^{11}C amounts are unchanged.

4.6 Spectral fit: MUST and JUST

The spectral fit, which returns the reconstructed rates for all the neutrino and background species, represents the last step of this analysis strategy. In order to enhance the robustness of our results, I have performed the fit with two independent software tools (MUST and JUST), based on the same fitting principles (see Sec. 4.6.1). The fitters validation and the compatibility of the results will be extensively discussed in Chapter 5.

Historically, MUST [75] (Milano nUsol Sensitivity Tool) was the first of the two tools developed thanks to the efforts of the Milano research group. The MUST fitting procedure has been validated against GooStats, the official Borexino multivariate fitting framework [76]; the relative errors of the species rates are equivalent at the $0.1\% - 1\%$ level [77].

On the back of enthusiasm given by MUST, the Jülich research group decided to develop its own tool as a way to cross-check the results given by the Milano software. That was how JUST [78] (Jülich nUsol Sensitivity Tool) came to light, as suggested by the affinity of the names. During my thesis experience, I have spent some months hosted by the Jülich group as an Erasmus student, giving a contribution to the JUST development. Due to it, in the following of this work I will dedicate some part to its description. Particularly, in Chapter 5 I will give an overview of JUST structure, while a detailed exposition will be given in Appendix A.

4.6.1 Fitting approach

In this Section, the details of the multivariate binned likelihood fit used in the sensitivity analysis are outlined. The fitting strategy relies on the PDFs produced as discussed in 4.3 and 4.4: they are exploited to create the pseudo-datasets, as described in Sec. 4.5, and they are also considered as the model for the fit.

Practically, each dataset is a histogram with k energy bins, labelled with $i = 1, \ldots, k$, where each bin contains n_i events. The likelihood is a standard Poisson binned likelihood function:

$$\mathcal{L}(\vec{n}|\vec{\lambda}(\vec{N})) = \prod_{i=1}^{k} \frac{e^{-\lambda_i}\lambda_i^{n_i}}{n_i!} \tag{4.4}$$

where λ_i is the total expected number of events in the i-th energy bin. λ_i depends on the number of events for each species $\vec{N} = (N_1, \ldots, N_{sp})$:

$$\lambda_i = \sum_{m=1}^{N_{sp}} N_m f_{m,i} \tag{4.5}$$

where N_{sp} is the total number of species and $f_{m,i}$ is the fraction of events in the i-th energy bin for the species m. The numbers of events N_m for each species, both for neutrinos and for backgrounds, are the fit parameters to be determined during the likelihood optimization. These numbers can be converted into reconstructed rates, returned by the fitters output assuming no threshold efficiency, through $R_m = N_m/\mathcal{E}$, where $\mathcal{E}$ is the exposure.

The two TFC-subtracted and TFC-tagged datasets are simultaneously fitted. Consequently, the likelihood involved is given by the product of the *Subtracted* and *Tagged* likelihoods, $\mathcal{L} = \mathcal{L}_{\text{Sub}} \cdot \mathcal{L}_{\text{Tag}}$, both described by eq. 4.4, effectively reducing the problem to a simple binned likelihood fit. More specifically, we minimize the negative log-likelihood to allow for an easy addition of potential Gaussian constraints on nuisance parameters, as showed in eq. 4.6:

$$\mathcal{L} \rightarrow -2\ln\mathcal{L} + \left(\frac{N-\overline{N}}{\sigma_N}\right)^2 \tag{4.6}$$

where $\overline{N} \pm \sigma_N$ is the value we want to constraint a specific parameter. This procedure represents an intermediate way between fixing and letting a parameter free to vary, allowing to include in the fit the information coming from an independent measurement.

Fitting the two mentioned sub-datasets simultaneously is decisive to improve the sensitivity on solar neutrinos. Let's report here a brief example. I have performed 500 fits in the fit configuration where CNO-ν has been constrained to the HZ-SSM value and I have assumed the baseline radiopurity scenario. The improvements on ^{7}Be-ν and *pep*-ν uncertainties are respectively ≈ 10 % and ≈ 4 % when fitting both the TFC-Subtracted and the TFC-Tagged datasets with respect to fit only the TFC-Subtracted one. Since the ^{7}Be-ν spectrum doesn't overlap the ^{11}C one, its improvement is only due to the increase in statistics. On the other hand, the *pep*-ν spectrum widely superimposes on ^{11}C one. The improvement on *pep*-ν sensitivity is therefore less pronounced due to the smaller signal over background ratio with respect to the ^{7}Be-ν energy spectrum region.

Let's now discuss more in detail the fit parameters. The TFC-subtracted and TFC-tagged datasets are statistically independent, but share many fit parameters: the neutrino (^{7}Be-ν, *pep*-ν, CNO-ν) and internal radioactivity (^{210}Bi, ^{210}Po, ^{85}Kr, ^{40}K, ^{238}U chain, ^{232}Th chain) number of events. The ^{11}C is present in both the datasets, but with two different rates since the TFC algorithm is applied. In order to properly take this into account, two independent parameters are included in the likelihood: a ^{11}C rate for the TFC-subtracted dataset (named $^{11}\text{C}_{\text{sub}}$), and a ^{11}C rate for the TFC-tagged dataset (named $^{11}\text{C}_{\text{tag}}$).

Being $\mathcal{E}_{\text{sub}} = \mathcal{E} \cdot \text{SE}$ and $\mathcal{E}_{\text{tag}} = \mathcal{E} \cdot (1 - \text{SE})$ the exposures relative to the TFC-subtracted and TFC-tagged datasets, respectively, considering TFC performances equal to SE = 0.70 and TP = 0.90, the two different ^{11}C rates can be calculated as follows[3]. We set the conservation of the number of events, i.e.

$$\mathcal{N}^i = \mathcal{N}^i_{\text{sub}} + \mathcal{N}^i_{\text{tag}} \tag{4.7}$$

where $\mathcal{N}^i$ is the total number of events for the i-th species, while $\mathcal{N}^i_{\text{sub}}$ and $\mathcal{N}^i_{\text{tag}}$ are the number of events for the i-th species in the TFC-subtracted and TFC-tagged datasets, respectively. We notice that eq. 4.7 can be written as:

$$\mathcal{R}^i \cdot \mathcal{E} = \mathcal{R}^i_{\text{sub}} \cdot \mathcal{E}_{\text{sub}} + \mathcal{R}^i_{\text{tag}} \cdot \mathcal{E}_{\text{tag}} \tag{4.8}$$

where $\mathcal{R}^i$ is the rate associated to the whole exposure, while $\mathcal{R}^i_{\text{sub}}$ and $\mathcal{R}^i_{\text{tag}}$ are the rates in the TFC-subtracted and TFC-tagged datasets, respectively. Therefore, for the $^{11}\text{C}_{\text{sub}}$ and $^{11}\text{C}_{\text{tag}}$ rates we obtain:

$$\mathcal{R}^{^{11}\text{C}}_{\text{sub}} = \mathcal{R}^{^{11}\text{C}} \cdot (1 - \text{TP}) \qquad \text{and} \qquad \mathcal{R}^{^{11}\text{C}}_{\text{tag}} = \frac{\mathcal{R}^{^{11}\text{C}} \cdot \mathcal{E} - \mathcal{R}^{^{11}\text{C}}_{\text{sub}} \cdot \mathcal{E}_{\text{sub}}}{\mathcal{E}_{\text{tag}}} \tag{4.9}$$

In this way, since the two parameters are independent, we do not assume to know *a priori* the TFC performances when fitting; conversely, once we will have real datasets, we will extract them from the fit results.

The importance of other cosmogenic isotopes is suppressed thanks to their low fluxes and to the detector veto after each muon crossing (see Chapter 3). For this reason, only the other two most abundant isotopes ^{10}C and ^{6}He are taken into account, sampling their spectrum only for the TFC-Tagged datasets and including their rates as free parameters.

---

[3] As a reminder, let's reiterate that SE is the TFC Subtracted Exposure, while TP the TFC Tagging Power. See Section 3.2.3 for more details.

CHAPTER 5

Software tools for solar neutrinos analysis and sensitivity

The sensitivity analysis for intermediate energy solar neutrinos is based on a multivariate spectral fit, which returns as output the neutrinos and backgrounds rates after the minimization of a negative log-likelihood.

As already mentioned in Chapter 4, the analysis has been carried out by means of two different software tools. They are called MUST (Milano nUsol Sensitivity Tool) and JUST (Jülich nUsol Sensitivity Tool) and, as the names suggest, they have been implemented independently by the two research groups of Milano and Jülich. These tools accomplish two goals: the generation of the pseudo-datasets necessary to perform the sensitivity studies and the fit on a dataset, real or Monte Carlo. MUST and JUST share the basic fitting principles even if the codes are organized in completely different structures. Having two separate tools is fundamental to validate the analysis reported in this work thus enhancing the reliability of the results.

This Chapter is organized as follows. In Section 5.1 I will present a general overview of JUST, including its architecture and usage. Then, to test the compatibility of the results provided by MUST and JUST, in Section 5.2 I will give a proof of their equivalence. Particularly, in Section 5.2.1 the toy generation validation is addressed, while in Section 5.2.2 the fitting procedure.

5.1 JUST: a look under the hood

The Jülich nUsol Sensitivity Tool [78] (JUST) is a fit software developed for JUNO solar neutrinos analysis and sensitivity. The main goal of JUST is to perform a binned likelihood fit on an arbitrary number of histograms. It is designed to be as flexible as possible during any sensitivity studies. It is written in c++ using the c++14 standard. JUST can be used either to do a real-data analysis by fitting an existing dataset or to perform massive sensitivity studies. In this latter case, the implemented procedure is divided into two steps. First of all, JUST takes care of the toy dataset generation by randomly sampling the number of events for each species and then poissonianly fluctuating it. After repeating this process for an enough number of times, the sum of all these sampled events will then assemble the histogram to fit. The outputs from each individual fit are then saved for later sensitivity studies, both in a text file format and a ROOT file.

The architecture of JUST is fully modular, meaning that any module can in principle be removed and replaced if needed, making testing and development seamless. Its structure consists in six modules, all of them called by the *Main.cpp*, acting as an organiser. A schematic depiction of it is given in Fig. 5.1.

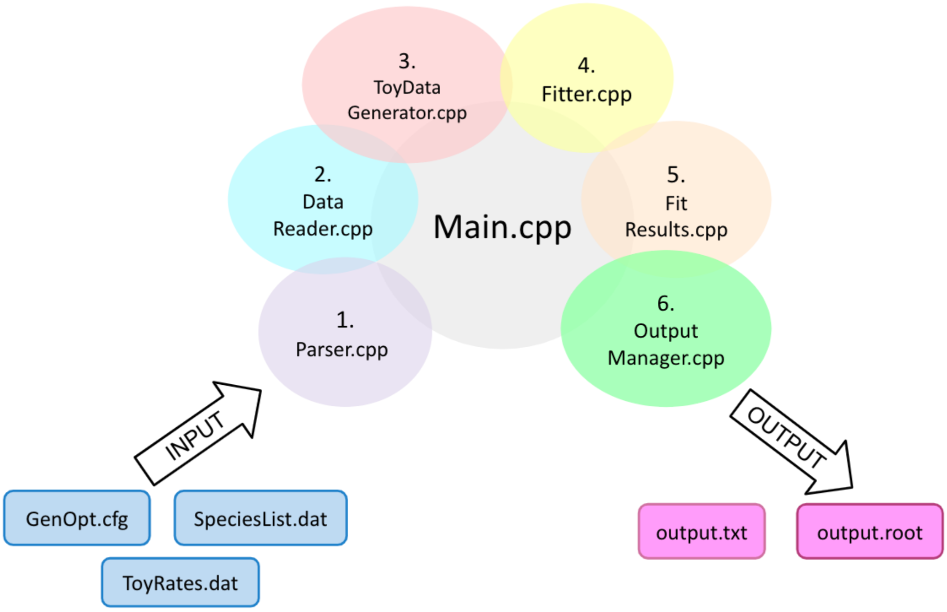

Figure 5.1: Schematic depiction of JUST architecture, together with the input and output files needed.

The modules are called in the following order:

1. *Parser* reads the configuration files and the command line arguments; then it arranges all the information to be readable for the successive modules;
2. *DataReader* opens different ROOT files – for PDFs and data – and analyze them. To gain speed of ≈ 3.5 times in the fitting procedure, it also converts ROOT histograms into c++ vectors;
3. *ToyDataGenerator* creates a generator for pseudo-data to be used in the fitter, by poissonianly sampling the numbers of events that will create the pseudo-datasets. This step is repeated N times, being N the number of toy-fits the user wants to perform;
4. *Fitter* either carries out a fit on data or iteratively fits each newly obtained pseudo-dataset through the minimization of the negative log-likelihood $-2\ln\mathcal{L}$;
5. *FitResults* extracts the results from the fits, only keeps the relevant parameters (the number of reconstructed events and their uncertainties, the χ^2/NDF, etc.)

and converts them to more physically interpretable results, e.g. it converts the results from counts to cpd/kton;

6. *OutputManager* finally takes the *FitResult* objects to create plots and write all necessary on the output files. JUST gives as output both a text file, containing for each of the N fits the results – e.g. rates in counts and cpd/kton, χ^2/NDF, the correlation and the covariance matrices – and some inputs of interest – e.g. the exposure and the fitting range – and a ROOT file, including all the relevant information organized in TTrees.

For what concerns the software usage, JUST is launched as a simple c++ executable with different configuration files whose paths must be specified as command line arguments.

The first configuration file, commonly referred to as "general options", contains the details needed related to the fit configuraion. These include for example the paths of the data and PDFs files, the fit range, the exposure, the number of toy-data fits to perform, and the names of the histograms in the ROOT files.

The second, the so-called "species list", contains information about all of the PDFs used to fit the histograms, including the initial guesses for the fitter. For each PDF, the user must specify a parameter name and a histogram in which this PDF or parameter should be considered. It is also possible to use "species list" to indicate whether a parameter is free, fixed or constrained in the fit with a Gaussian pull-term (see eq. 4.6).

Finally, the third configuration file – "toy rates" – includes information concerning the creation of the toy-data spectra, including all of the species, their corresponding interaction rates and the PDFs names. These can be different from the "species list" ones thus allowing to fit the same data under different model assumption, and vice-versa.

5.2 Validation procedure between MUST and JUST

To be confident that the sensitivity results we performed with MUST and JUST are compatible within a certain level of agreement, a careful sequence of cross-checks is fundamental.

Particularly, the validation procedure has been divided into two steps described in the next sections: the toy generation and the fitting procedure validations.

5.2.1 Toy generator validation

To validate the generation of the pseudo-datasets, I looked at the distributions of the rates (or equivalently, the number of events) of the generated events. For each species, I have run 10^4 simulations and, starting from the injected rates given as inputs, the fitters then converted internally the mentioned rates into counts and fluctuate them gaussianly or poissonianly. I have repeated this procedure with both MUST and JUST, considering the same input injected rates.

The results for ^{7}Be-ν, *pep*-ν and CNO-ν are shown in Fig. 5.2. The top part of each plot illustrates the distributions of the fluctuated rate for both MUST (green histograms) and JUST (blue histograms) together with a red vertical line representing the value of the injected rate. On the other hand, the bottom part of each plot shows the histogram of the entries difference between MUST and JUST, bin per bin. By looking at the results, we can immediately notice that, for each species, the distributions are approximately centered on the injected rate for both MUST and JUST. The JUST distributions appear systematically $\lesssim 10$ % broader with respect to the MUST ones. This fact could be ascribed to the different approach in the fluctuation of the events. In particular, MUST extracts the number of events from a gaussian distribution with mean equal the "injected" N_{events} and standard deviation equal to $\sqrt{N_{\text{events}}}$; oppositely, JUST extracts it from a poissonian distribution with mean equal to N_{events}.

5.2.2 Fitter validation

Besides the toy generator validation, the next step is the evaluation of the fitting procedure itself.

To achieve this goal, I have compared the results given by MUST and JUST when fitting separately 2000 pseudo-datasets. First of all, I have generated the pseudo-datasets independently from the two tools: then MUST and, sequentially, JUST fitted them one by one. The fit configuration chosen to perform these studies considers one year of data-taking and a fiducial volume radius of 14 m. Furthermore, the internal backgrounds rates have been treated according to the ideal radiopurity scenario (see Chapter 3), while the neutrinos rates are based on the HZ-SSM predictions. All the parameters have been left free to vary but the *pep*-ν rate, which was constrained to the value based on the HZ-SSM.

As last step, both the MUST and JUST output reconstructed rates and their uncertainties have been saved for a comparison. Particularly, to compare the results for each dataset i and for each species j two quantities have been calculated. Firstly, the bias on the reconstructed rates between MUST and JUST, whose formula is expressed in equation 5.1:

$$B_{ij}\,[\%] = 100 \cdot \frac{R_{ij}^{M} - R_{ij}^{J}}{R_{ij}^{M} + R_{ij}^{J}} \cdot 2 \tag{5.1}$$

where R_{ij}^{M} is the reconstructed rate given by MUST for the species j and the dataset i and R_{ij}^{J} is the analogous for JUST. Ideally, to have an optimal level of agreement between the two fitters, B_{ij} should be compatible to zero for every i, j. The second quantity evaluated is the relative error difference on the reconstructed rates between MUST and JUST, given by the equation 5.2:

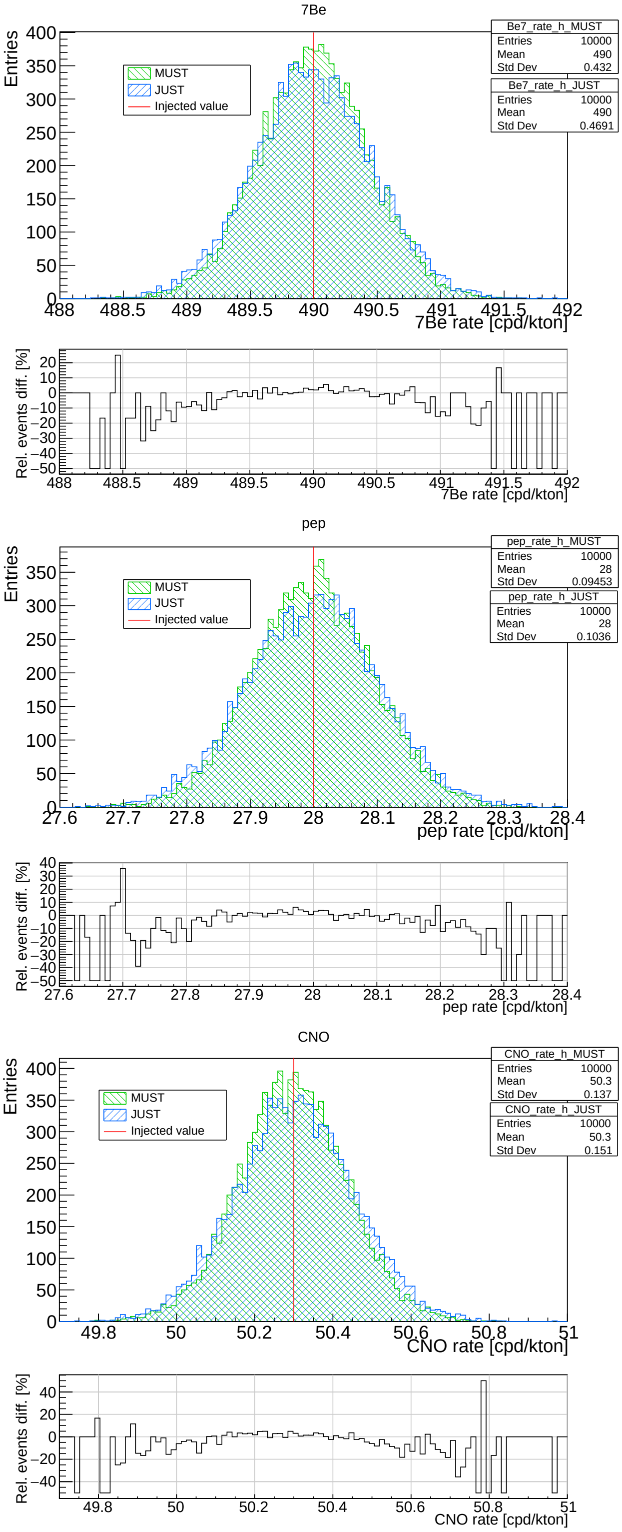

Figure 5.2: ^{7}Be$-\nu$ (top panel), *pep*$-\nu$ (central panel) and CNO$-\nu$ (bottom panel) toy generation results. For each panel, the top part shows the toy distributions for both MUST (green) and JUST (blue) for 10^4 simulations performed. The red vertical line is the value of the injected rate. The bottom part represents the relative entries difference between MUST and JUST.

$$E_{ij}\,[\%] = 100 \cdot \left(\frac{\sigma_{ij}^{M}}{R_{ij}^{M}} - \frac{\sigma_{ij}^{J}}{R_{ij}^{J}} \right) \tag{5.2}$$

where σ_{ij}^{M} and σ_{ij}^{J} are the standard deviations of the reconstructed rates for the species j and the dataset i, for MUST and JUST respectively. Also in this case we expect E_{ij} to be compatible to zero for every i, j.

For ^{7}Be-ν, *pep*-ν and CNO-ν the distributions of the results concerning both the reconstructed rates and the standard deviations are shown in Fig. 5.3, respectively in the left and right panels. Conversely, the results for every species are summarized in Table 5.1.

Species	$\overline{B}$ [%]	$\overline{E}$ [%]
^{7}Be-ν	$2.4 \cdot 10^{-4}$	$-3.6 \cdot 10^{-4}$
pep-ν	$5.7 \cdot 10^{-5}$	$2.3 \cdot 10^{-3}$
CNO-ν	$1.5 \cdot 10^{-3}$	$8.9 \cdot 10^{-2}$
^{210}Bi	$2.8 \cdot 10^{-5}$	$1.2 \cdot 10^{-2}$
^{210}Po	$-1.4 \cdot 10^{-4}$	$-4.3 \cdot 10^{-4}$
^{40}K	$3.7 \cdot 10^{-4}$	$6.0 \cdot 10^{-3}$
^{85}Kr	$-1.1 \cdot 10^{-3}$	$-1.4 \cdot 10^{-2}$
^{238}U	$-3.7 \cdot 10^{-5}$	$-1.1 \cdot 10^{-3}$
^{232}Th	$9.9 \cdot 10^{-6}$	$2.3 \cdot 10^{-3}$
^{11}C$_{sub}$	$-6.9 \cdot 10^{-5}$	$4.7 \cdot 10^{-4}$
^{11}C$_{tag}$	$-7.9 \cdot 10^{-5}$	$1.5 \cdot 10^{-5}$

Table 5.1: The percentage bias on the reconstructed rates between MUST and JUST (second column) and the percentage error difference on the reconstructed rates between MUST and JUST (third column) for every species. Both of them are extracted as the mean of the corresponding distributions, whose examples for ^{7}Be$-\nu$, *pep*$-\nu$ and CNO$-\nu$ are shown in Fig. 5.3.

As we can see from the Table 5.1, an excellent level of agreement between the two fitter has been achieved: particularly, both the $\overline{B}$ and $\overline{E}$ values are compatible to zero for every species.

Therefore, we can conclude that MUST and JUST can be considered equivalent and appropriate for the solar neutrinos sensitivity analysis, leading to independent and compatible results.

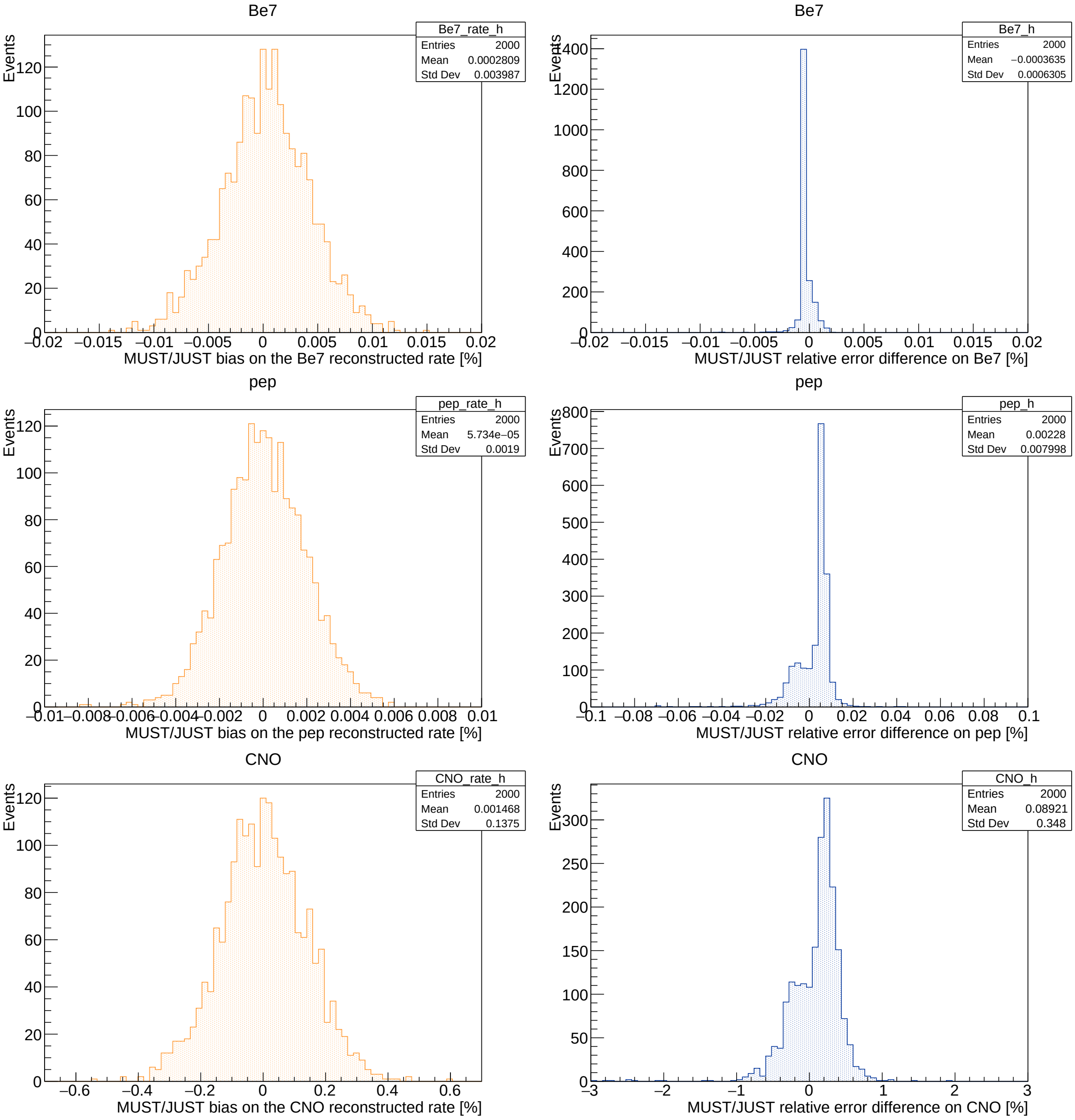

Figure 5.3: ^{7}Be$-\nu$ (top panel), *pep*$-\nu$ (central panel) and CNO$-\nu$ (bottom panel) fitter validation results. For each panel, the left part shows the distribution of the bias on the reconstructed rates between MUST and JUST, while the right panel shows the distribution of the relative error difference on the reconstructed rates between MUST and JUST.

CHAPTER 6

Results on ^{7}Be, *pep* and CNO neutrinos sensitivity

The following Chapter is devoted to the description on the sensitivity results to ^{7}Be, *pep* and CNO solar neutrinos. The achievable precision to intermediate energy neutrinos fluxes is strongly related to the overall detector exposure and to the signal over background ratio, which in turn depends on the scintillator radiopurity levels. The sensitivity analysis has been performed as a function of different exposures and different background rates, thus allowing us to optimize the methods and foresee the most crucial aspects impacting the analysis before the beginning of the data-taking. Because of that, a set of four plausible radiopurity scenarios has been considered for this analysis (see Chapter 3). Moreover, the impact of possible variations from the starting conditions of background contaminations has also been addressed.

The Chapter is structured as follows. In Sec. 6.2 and 6.3, I will present the results concerning the sensitivity on ^{7}Be and *pep* neutrinos, respectively. The results on CNO neutrinos sensitivity will be described in Sec. 6.4, while the case in which the ^{13}N and ^{15}O contributions are separately treated is discussed in Sec. 6.4.4.

6.1 Standard fit configuration

To quantitatively evaluate the JUNO sensitivity to intermediate energy solar neutrinos, the analysis procedure has been carefully described in Chapter 4. Here we remind that the multivariate fit has been performed on a large number of pseudo-datasets ($\gtrsim 10^4$), assessing the average extracted rates for signal and background and the corresponding average uncertainty. It's worth to point out that all the studies presented in this work considers only the statistical uncertainties on the neutrino rates and not the systematic ones. This means that the backgrounds spectral shapes are assumed to be known with high precision, such that the systematic error related to the shapes knowledge is kept under control.

The standard fit configuration employed, unless otherwise stated, consists in all the signal and background rates left free to vary. The default fiducial volume is a $r_{FV} < 14$ m radius sphere; the selected fit range is 650 p.e. $< \mathrm{m_{NQE}} <$ 2400 p.e., roughly corresponding to a scattered e^- kinetic energy range 0.45 MeV $< E_{\mathrm{vis}} <$

1.7 MeV; the TFC performances parameters considered are TP = 0.90 and SE = 0.70, respectively.

An exemplary sensitivity outcome can be obtained by analyzing the correlation plots shown in Fig. 6.1, referred to the baseline radiopurity scenario. The red histograms display the distributions of the extracted rates for each of the species, in cpd/kton units. The distributions are gaussians and centered on the injected values (black vertical lines) without showing any significant biases with respect to the rates used as simulation inputs: this confirms the feasibility of a solar neutrino measurement with JUNO. For each component, the statistical error is given by the distributions width. On the other side, the non-diagonal 2D distributions show the correlation plots among the different species. We notice a strong correlation between *pep*-ν and ^{210}Bi, while CNO-ν are highly anti-correlated with *pep*-ν and ^{210}Bi. These behaviours originate from the similar spectral shapes *pep*-ν, CNO-ν and ^{210}Bi share, as discussed more in detail in Sec. 6.4.

6.2 Sensitivity results on ^{7}Be neutrinos

The sensitivity on ^{7}Be solar neutrinos is mainly driven by two factors: the collected statistics and the signal over background ratio, which in turns depends on the radiopurity levels.

Due to the overlap of the energy spectra showed in Fig. 6.2, the ^{7}Be-ν precision can be influenced especially by ^{85}Kr, ^{210}Po and ^{226}Ra backgrounds levels.

The fit configuration for the ^{7}Be-ν sensitivity results is now described. The datasets are built injecting the neutrino rates according to the HZ-SSM predicted values (see Table 1.2), while the internal background rates are selected according to one of the four radiopurity scenarios defined in Sec. 3.2.1 (IBD, baseline, ideal and Borexino-like).

6.2.1 Impact of the exposure on ^{7}Be-ν sensitivity

As previously written, the sensitivity to solar neutrinos depends on the collected statistics, thus on the data-taking duration. Because of that, it's interesting to show the relative uncertainty trend as time goes by.

In particular, the relative uncertainty of ^{7}Be neutrino rates as a function of data-taking time (bottom scale) and exposure (top scale) is shown in Fig. 6.3 for the four radiopurity scenarios. Borexino-like, ideal, baseline and IBD radiopurity scenario trends are displayed respectively in orange, green, light blue and blue dotted lines. The dot markers represent the simulated points. The best Borexino result is reported as the black dashed horizontal line.

The relative error trends approximately follow the power law relation:

$$\frac{\sigma_R}{R} = a + b\mathcal{E}^{-1/2} \tag{6.1}$$

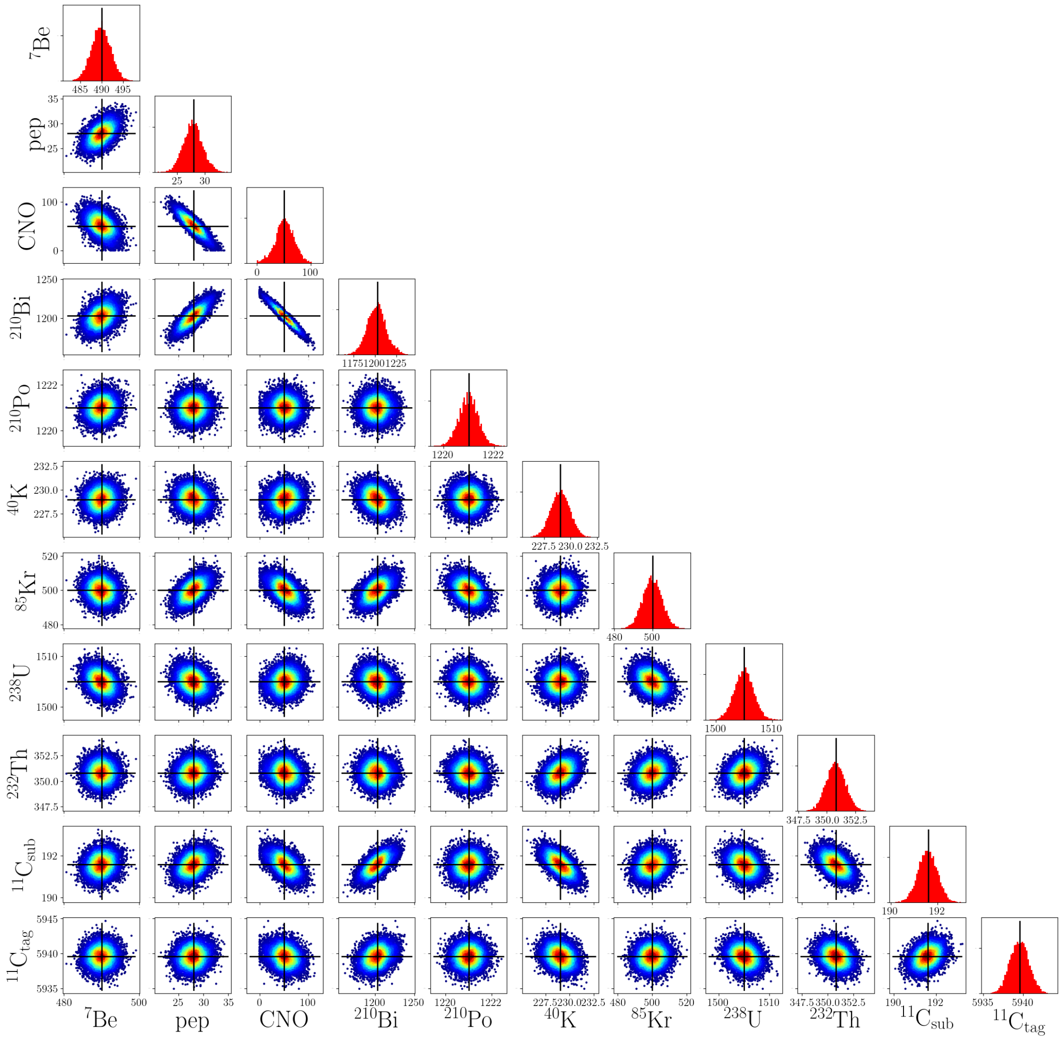

Figure 6.1: Correlation plots for an exemplary sensitivity study, performing 10^4 fits in the baseline scenario. The red histograms display the distributions of the extracted rates, expressed in cpd/kton units. The non-diagonal 2D distributions are the correlation plots among the different species.

where $\mathcal{E}$ is the dataset exposure, while a and b are coefficients depending on the neutrino species and on the selected radiopurity scenario. This power law exponent is due to the increasing statistics, for which one can poissonianly assume that $\sigma_R \sim \sqrt{\mathcal{E}}$. The curves depicted in Fig. 6.3 represent the fitted curves on the data points. For each radiopurity scenario, the a and b parameters extracted from the fit are summarized in Table 6.1, together with the χ^2/NDF values. One can see that the simulated points are in good agreement with the power law relation showed in eq. 6.1: this is also proved by the low χ^2/NDF values equal to $\approx 10^{-5} - 10^{-4}$.

From the results illustrated in Fig. 6.3, we resolve that JUNO will reach competitive uncertainties on ^{7}Be-ν even after 1 year of data-taking in all the radiopurity

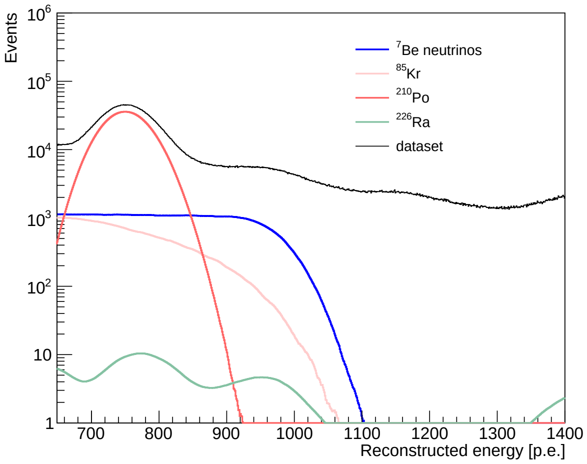

Figure 6.2: ^{7}Be-ν, ^{85}Kr, ^{210}Po and ^{226}Ra reconstructed energy spectra, expressed in photoelectrons. The black line represents the dataset assuming the baseline scenario. It is clear that all these energy shapes overlap significantly.

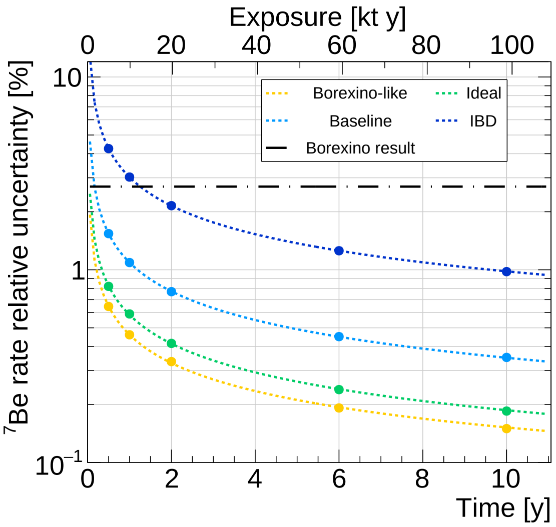

Figure 6.3: The relative uncertainty of ^{7}Be neutrino rates as a function of exposure. Borexino-like, ideal, baseline and IBD radiopurity scenario trends are shown respectively in orange, green, light blue and blue dotted lines. The dot markers represent the simulated points. The Borexino best result is reported as the black dashed horizontal line.

scenarios: $\approx$ 3 % (IBD), $\approx$ 1 % (baseline), $\approx$ 0.5 % (ideal) and $\approx$ 0.3 % (Borexino-like). In all the radiopurity scenarios but the IBD one, after 2 years of data-taking we are significantly confident that JUNO will measure the ^{7}Be-ν rate better than what previously done by Borexino. Finally, after 6 years of data-taking, in all the scenarios but the IBD one, ^{7}Be neutrinos can be detected with a statistical uncer-

	$a \pm \sigma_a$	$b \pm \sigma_b$ [(kton $\cdot$ days)$^{1/2}$]	χ^2/NDF
Borexino-like	$(9.7 \pm 3.7) \cdot 10^{-3}$	$(4.50 \pm 0.04) \cdot 10^{-1}$	$1 \cdot 10^{-5}$
Ideal	$(-5.7 \pm 5.9) \cdot 10^{-3}$	$(5.9 \pm 0.1) \cdot 10^{-1}$	$4 \cdot 10^{-5}$
Baseline	$(2.8 \pm 2.5) \cdot 10^{-2}$	1.06 ± 0.03	$7 \cdot 10^{-4}$
IBD	$(4.4 \pm 2.7) \cdot 10^{-2}$	2.94 ± 0.03	$8 \cdot 10^{-4}$

Table 6.1: Results of the parameters extracted from the fit on ^{7}Be-ν uncertainty over the time with the power law eq. 6.1. The first, second and third columns show a, b and the χ^2/NDF, respectively.

tainty $\lesssim 1$ %.

6.2.2 Impact of ^{85}Kr background on ^{7}Be-ν sensitivity

As described in Chapter 3, the ^{85}Kr isotope is a β-emitter whose spectral shape is very similar to the electron recoil spectrum due to ^{7}Be neutrinos. Previous neutrino experiments reports how ^{85}Kr could be absorbed by the acrylic surface during its construction due to air exposures, and then it could be emanated into the scintillator after the detector filling. The ^{85}Kr rate present in the scintillator strongly depends on the diffusion coefficient through acrylic, which is still not known precisely. Consequently, this section aims to study the ^{85}Kr rate impact on the ^{7}Be-ν sensitivity.

This has been done by scaling the ^{85}Kr rate for the four radiopurity scenarios, starting from the default value, up to three orders of magnitude more. The results are shown in Fig. 6.4.

As expected, the ^{85}Kr rate increase impacts on the ^{7}Be-ν statistical uncertainty. In particular, for the Borexino-like, ideal and baseline scenarios it is almost quadrupled going from the standard ^{85}Kr value to the 10^3 times case. In case of IBD scenario, when the ^{85}Kr rate is increased of a factor 500, the fit is no more able to accurately determine the ^{7}Be-ν rate, due to the tiny signal over background ratio.

6.2.3 Impact of ^{210}Po background on ^{7}Be-ν sensitivity

As outlined in Chapter 3, ^{210}Po is an α-emitter whose spectral shape consists in a gaussian peak, shifted in the analysis ROI because of the quenching effects happening in the liquid scintillator. More specifically, the peak is expected near 700 p.e. and can be clearly seen to the left of the characteristic ^{7}Be-ν shoulder (see for example Fig. 6.2). In Table 3.2 we assumed that the ^{210}Po in the detector is coming solely from the ^{210}Pb and ^{238}U decay chains. However, as reported by the Borexino experiment [61], the scintillator could be contaminated with ^{210}Po supported neither by the ^{210}Pb nor by the ^{223}U chains, which could be washed out from the

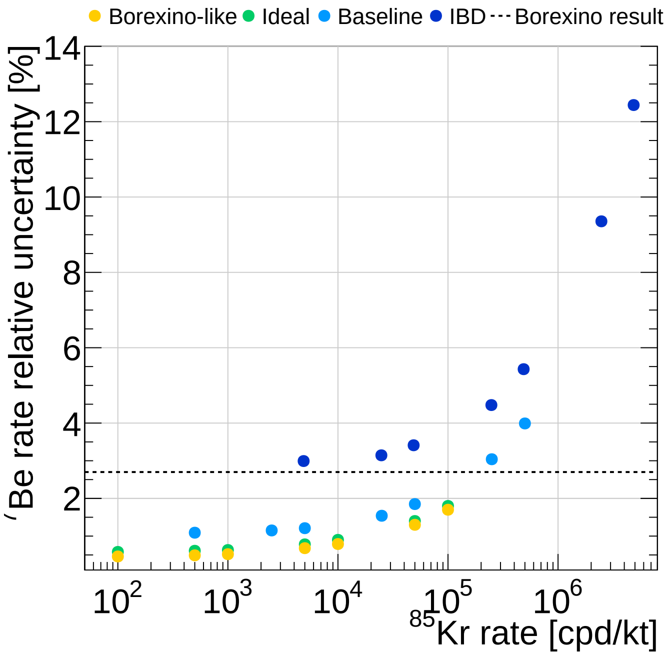

Figure 6.4: The relative uncertainty of ^{7}Be neutrino rates as a function of of the rate of ^{85}Kr for 1 year of data-taking. Borexino-like, ideal, baseline and IBD radiopurity scenarios are shown respectively in orange, green, light blue and blue.

surface of the pipes used to fill the detector.

Because of these reasons, we have studied the effect of potentially large amounts of *unsupported* ^{210}Po on the sensitivity of ^{7}Be solar neutrinos. Therefore, starting from the four standard radiopurity scenarios, we injected an increasing rate of ^{210}Po: from 0 cpd/kton to $8 \cdot 10^6$ cpd/kton. It's worth to emphasize that ^{210}Po has a mean lifetime of $\approx$ 138 days: therefore, by waiting for a sufficient amount of time, it would naturally decay and its rate would decrease. The results of this study are illustrated in Fig. 6.5. However, when considering the Borexino-like, ideal and baseline scenarios, the sensitivity on ^{7}Be-ν is still better than the Borexino best result ($\approx$ 2.7 %) until a ^{210}Po rate equal to $4 \cdot 10^6$ cpd/kton. On the other hand, in the IBD scenario, going from an *unsupported* ^{210}Po rate of 10^4 cpd/kton (i.e. the standard IBD scenario) to $8 \cdot 10^6$ cpd/kton, the ^{7}Be-ν relative uncertainty goes from $\approx$ 3 % to $\approx$ 6.5 %.

6.2.4 Impact of out-of-equilibrium ^{226}Ra background on ^{7}Be-ν sensitivity

The ^{226}Ra isotope is part of the ^{238}U chain and it is usually assumed to be in equilibrium within the chain. Nonetheless, an extra out-of-equilibrium ^{226}Ra contamination, may be present in the water or in the scintillator because of the detector

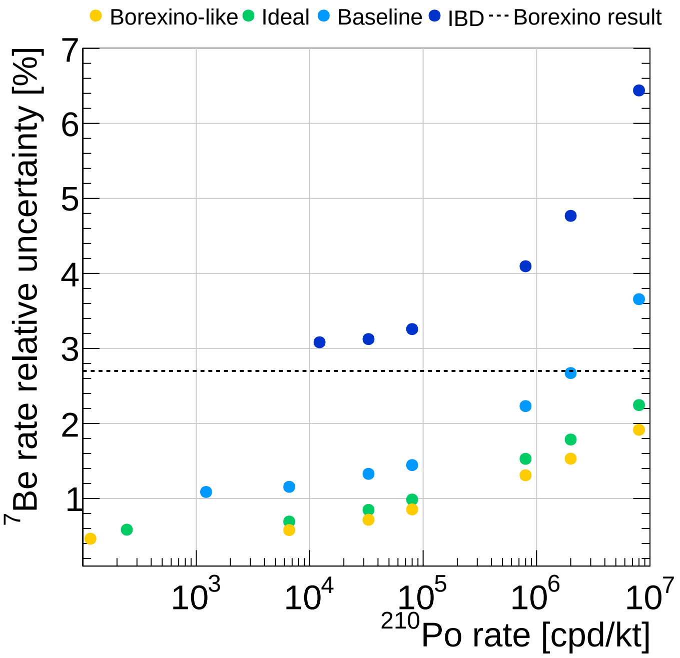

Figure 6.5: The relative uncertainty of ^{7}Be neutrino rates as a function of of the amount of *unsupported* ^{210}Po for 1 year of data-taking. Borexino-like, ideal, baseline and IBD radiopurity scenarios are shown respectively in orange, green, light blue and blue.

filling operations. This ^{226}Ra additional contamination, whose spectrum identification is eased by the prominent α peaks, does not introduce new features in the reconstructed energy spectrum. The results are displayed in Fig. 6.6. Taking into account that the JUNO detector requirements foresee the ^{226}Ra rate to be $\lesssim$ 1.42 cpd/kton, we have performed this study moving from a ^{226}Ra rate of 0 cpd/kton to 142 cpd/ton, i.e. 10 times the design requirements. The ^{7}Be-ν relative statistical uncertainties almost double for all the radiopurity scenarios, reaching $\approx$ 1 % (Borexino-like scenario), $\approx$ 1.5 % (ideal scenario), $\approx$ 2.2 % (baseline scenario) and $\approx$ 5.3 % (IBD scenario). We can thus conclude that an out-of-equilibrium ^{226}Ra contribution can be easily identified by the multivariate fit and does not spoil the analysis, although it has some impact on the overall uncertainty of the ^{7}Be-ν measurement.

6.3 Sensitivity results on *pep* neutrinos

The sensitivity on *pep* neutrinos is strongly influenced by the signal over background ratio. Consequently it's extremely important to reduce as possible the background levels, especially the ^{210}Bi and the ^{11}C, whose identification is helped by the TFC algorithm (see Chapter 3). Moreover, the similarity between the *pep*-ν and

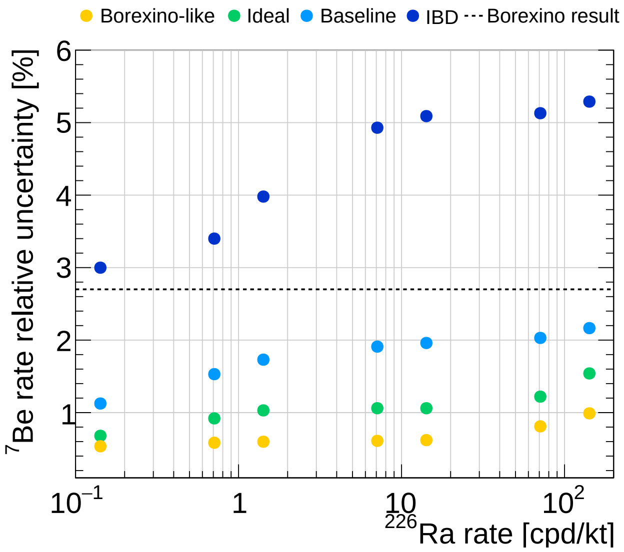

Figure 6.6: The relative uncertainty of ^{7}Be neutrino rates as a function of of the ^{226}Ra rate for 1 year of data-taking. Borexino-like, ideal, baseline and IBD radiopurity scenarios are shown respectively in orange, green, light blue and blue.

CNO-ν spectral shapes further complicates the *pep*-ν measurement. Fig. 6.7 shows *pep*-ν, CNO-ν, ^{210}Bi and ^{11}C spectra, highlighting the overlapping of the mentioned spectral shapes. The fit configuration employed for the *pep*-ν sensitivity is the same used for ^{7}Be-ν sensitivity and illustrated in Sec. 6.2.

6.3.1 Impact of the exposure on *pep*-ν sensitivity

First of all, we have studied the impact of the exposure on the *pep*-ν sensitivity. The relative uncertainty of *pep*-ν rates as a function of data-taking time (bottom scale) and exposure (top scale) is shown in Fig. 6.8.

As described in Sec. 6.2.1, the curves plotted in Fig. 6.8 have been obtained through a power law fit according to eq. 6.1, from which the parameters a, b and the χ^2/NDF values are extracted and reported in Table 6.2. Also in this case, the simulated points are in good agreement with eq. 6.1.

From the results illustrated in Fig. 6.8, we can conclude that in the IBD scenario JUNO will be sensitive to *pep*-ν only after 2 years, due to the too large amount of backgrounds. Nonetheless, in all the other radiopurity scenarios (baseline, ideal and Borexino-like) JUNO will achieve competitive results, better than the Borexino best result even only after 1 year ($\approx$ 15 % baseline, $\approx$ 9 % ideal and $\approx$ 8 % Borexino-like). After 10 years, JUNO can achieve a *pep*-ν sensitivity of $\approx$ 5 %, $\approx$ 3 % and $\approx$ 2.5 % in baseline, ideal and Borexino-like scenarios, respectively.

In the fit configuration we considered so far, where all the species are left free to vary, JUNO does not always have the good enough sensitivity to identify the

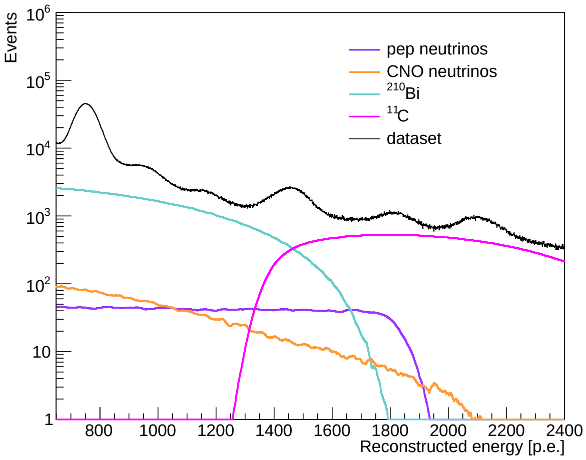

Figure 6.7: *pep-ν*, CNO-*ν*, ^{210}Bi and ^{11}C reconstructed energy spectra, expressed in photoelectrons. The black line represents the dataset assuming the baseline scenario. It is clear that all these energy shapes overlap significantly.

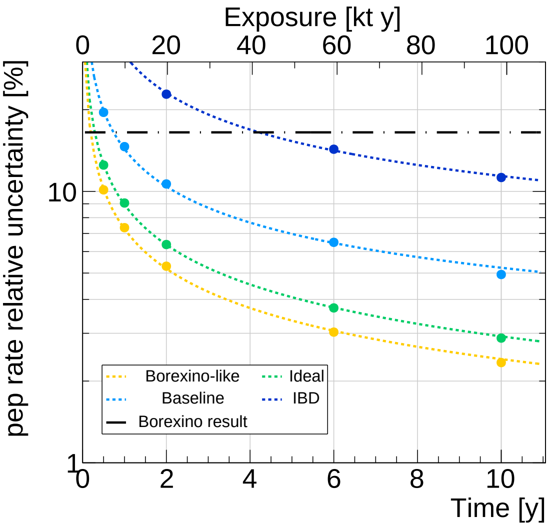

Figure 6.8: The relative uncertainty of *pep* neutrino rates as a function of exposure. Borexino-like, ideal, baseline and IBD radiopurity scenario trends are shown respectively in orange, green, light blue and blue dotted lines. The dot markers represent the simulated points. The Borexino best result is reported as the black dashed horizontal line.

pep neutrinos, as for example in the IBD scenario. Because of this fact, it could be useful to help the fit by imposing a constraint on some rate species problematic for the *pep-ν* rate determination. In this regard, the most suitable species candidates for this role are the CNO-*ν* or ^{210}Bi. Indeed, as one can see in Fig. 6.9, the *pep-ν* rate is strongly anti-correlated to the CNO-*ν* rate and correlated to ^{210}Bi rate, due to the

	$a \pm \sigma_a$	$b \pm \sigma_b$ [(kton · days)$^{1/2}$]	χ^2/NDF
Borexino-like	$1.3 \cdot 10^{-1} \pm 8 \cdot 10^{-2}$	7.29 ± 0.09	$7 \cdot 10^{-3}$
Ideal	$2.4 \cdot 10^{-1} \pm 1.2 \cdot 10^{-1}$	8.7 ± 0.1	$2 \cdot 10^{-2}$
Baseline	$8.7 \cdot 10^{-1} \pm 2.8 \cdot 10^{-1}$	13.7 ± 0.3	$8 \cdot 10^{-2}$
IBD	$1.3 \cdot 10^{-1} \pm 7.8 \cdot 10^{-2}$	7.29 ± 0.09	$6.6 \cdot 10^{-3}$

Table 6.2: Results of the parameters extracted from the fit on *pep*-ν uncertainty over the time with the power law eq. 6.1. The first, second and third columns show a, b and the χ^2/NDF, respectively.

overlapping of the energy spectra.

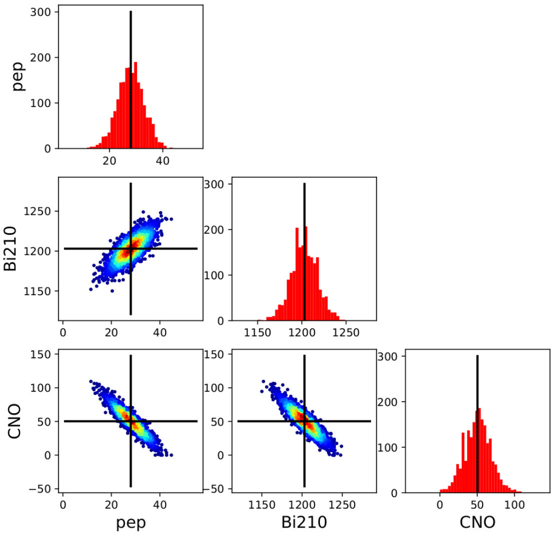

Figure 6.9: Results of the multivariate fits of 10^4 Monte Carlo pseudo-experiments for the two components expected to influence the most the sensitivity to *pep*-ν signal (CNO neutrinos and ^{210}Bi). The red histograms represent the extracted rate of the species, and are distributed around the injected value (the black lines). The non-diagonal frames show the species correlation plots.

6.3.2 Impact of a ^{210}Bi constraint on *pep*-ν sensitivity

The isotope ^{210}Bi is a β-emitter with a short lifetime of $\approx$ 7 days. The similarity between *pep* neutrinos and ^{210}Bi energy spectra gives rise to the strong correlation shown in Fig. 6.9. Because of that, it might be interesting to investigate the effects on a constraint on the ^{210}Bi rate, which may help the fit to more easily identify the *pep*-ν rate. Nevertheless, finding a proper constraint for the ^{210}Bi rate is anything but trivial. An option could be to exploit the α particles from the ^{210}Po decay as tracers of ^{210}Bi, selected event-by-event by means of the pulse-shape discrimination technique, like previously done in the Borexino experiment [37]. To improve the ^{7}Be-ν relative uncertainty with respect to the fit configuration where no constraints are included, it is necessary to constrain the ^{210}Bi rate with a precision $\lesssim$ 1%. However, such a level of precision is presumably extremely hard to achieve, especially due to possible convective motions inside the liquid scintillator. Therefore, we can conclude that a constraint on the ^{210}Bi rate would not be meaningful in this case.

6.3.3 Impact of ^{11}C background on *pep*-ν sensitivity

The ^{11}C isotope is the most abundant cosmogenic nuclide present in the analysis ROI. Since the spectral shape of *pep* neutrinos is partially *shadowed* by the ^{11}C energy spectrum, as depicted in Fig. 6.7, we expect the ^{11}C to affect the uncertainty on *pep*-ν. Therefore, an efficient identification of ^{11}C through the TFC algorithm (see Chapter 3) is important in order to keep this annoying background under control.

We thus evaluated the impact of the TFC-parameters, i.e. Tagging Power (TP) and Subtracted Exposure (SE), on the *pep* neutrinos sensitivity. Ideally, TP and SE should be as high as possible, in order to enhance the *pep* signal over background ratio: an ideal ^{11}C tagging technique should identify all the ^{11}C events (TP $=$ 1) without losing any exposure in the TFC-Subtracted dataset (SE $=$ 1).

To perform this study, we ran the multivariate fit 5000 times for each TP vs. SE configuration, considering 6 years of data-taking, in the Borexino-like, ideal, baseline and IBD scenarios. Particularly, we consider $0.60 \leqslant \mathrm{TP} \leqslant 0.95$ and $0.60 \leqslant \mathrm{SE} \leqslant 0.95$, omitting the case TP $=$ 1 and SE $=$ 1 since not realistically achievable. The results for *pep*-ν precision in the four radiopurity scenarios are shown in top left, top right, bottom left and bottom right panels of Fig. 6.10, respectively. The color scale represents the *pep* neutrinos uncertainties relative to the values obtained when TP $=$ 0.9 and SE $=$ 0.7.

As expected, the TFC-parameters notably impact the *pep*-ν sensitivity. The *pep*-ν rate uncertainties show different behaviours depending on the scenario we are considering. As we can see in Fig. 6.10, moving from the Borexino-like to IBD scenarios, the impact of the TFC-parameters decrease as we can notice from the smoothing of the color gradient. This can be explained by considering that the internal backgrounds reach such a high level of contamination that the signal over background ratio is not influenced by the TFC anymore. Indeed, in this case, the ^{11}C isotope does not represent the dominant source of background in this energetic region.

Moreover, the TP impact is always much larger with respect to the SE one: in fact, the *pep*-ν rate precision is almost doubled from TP $=$ 0.60 to TP $=$ 0.95. This means that the ability of identifying the ^{11}C that is to have a ^{11}C-depleted dataset, is more relevant than the fraction of events included in the TFC-Subtracted spectrum.

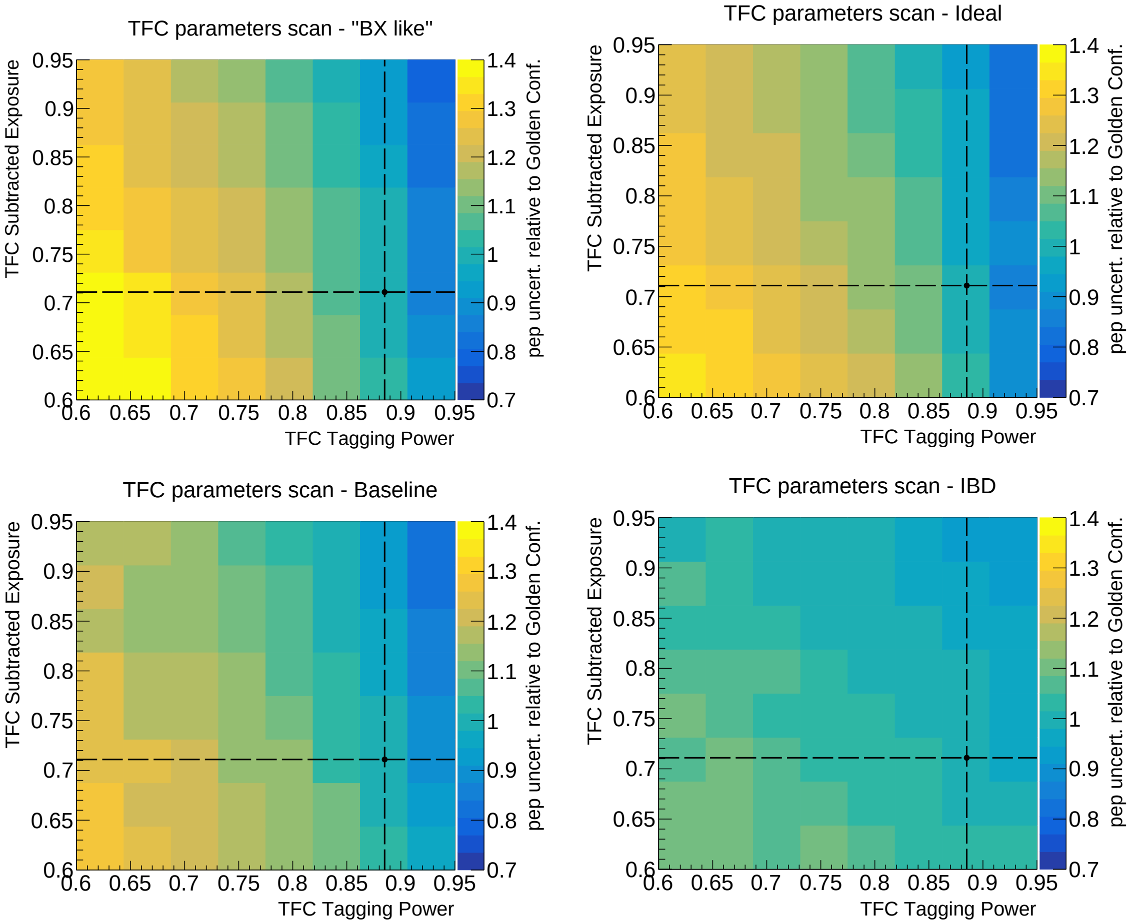

Figure 6.10: The *pep* neutrinos rate uncertainties (color scale) as a function of TP (x-axis) and SE (y-axis), after 6 years of data-taking. The z-axis (color scale) represents the *pep* neutrinos uncertainties relative to *pep* uncertainty when TP = 0.9 and SE = 0.7 (here named *Golden Configuration* for convenience). Borexino-like, ideal, baseline and IBD scenarios are respectively shown in top left, top right, bottom left and bottom right panels.

6.4 Sensitivity results on CNO neutrinos

As depicted in Fig. 6.7, CNO neutrinos energy spectrum lies in the same energy range of *pep* neutrinos, ^{210}Bi and ^{11}C. Therefore, the determination of the CNO-ν rate is made more difficult given the correlations show in Fig. 6.9.

The strategy to investigate the CNO-ν sensitivity is the following. Firstly, we started by performing 10^4 multivariate fits in the configuration where all the species are left free to vary. In this case, we have studied the CNO-ν uncertainty over the exposure and the impact of the ^{11}C (see Sec. 6.4.1 and Sec. 6.4.2). Then, to enhance the CNO-ν sensitivity we put a constraint on the *pep*-ν rate based on the HZ-SSM predictions (see Sec. 6.4.3). In this case, to confine the rate on one of the two SSM predictions − HZ-SSM or LZ-SSM − is not so problematic since the difference between the two predicted values of *pep*-ν rate is $\approx$ 1.4 %. Finally, we have performed some studies assuming separately the ^{15}O-ν and the ^{13}N-ν, instead of treat the CNO neutrinos as a single species (see Sec. 6.4.4).

6.4.1 Impact of the exposure on CNO-ν sensitivity

The relative uncertainties of CNO-ν rates as a function of data-taking time (bottom scale) and exposure (top scale) are shown in Fig. 6.11.

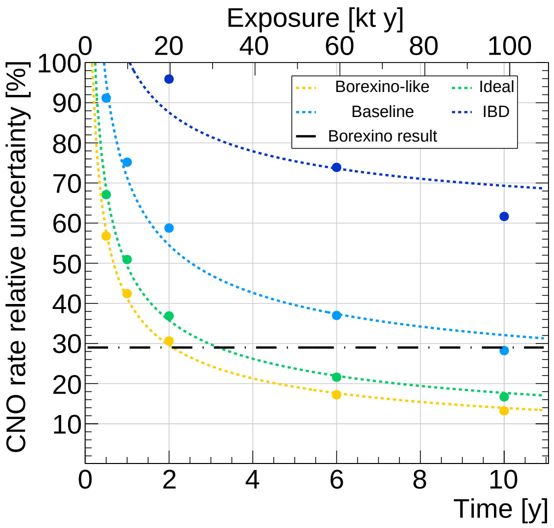

Figure 6.11: *Fit configuration: all species free to vary.* The relative uncertainty of CNO neutrino rate as a function of exposure. Borexino-like, ideal and baseline radiopurity scenario trends are shown respectively in orange, green and light blue dotted lines. The dot markers represent the simulated points. The Borexino best result is reported as the black dashed horizontal line.

In the IBD scenario, being the CNO-ν relative uncertainty always above $\approx$ 60%, we can state that JUNO will not be sensitive to CNO neutrinos. For what concerns the baseline scenario, JUNO will reach a relative uncertainty of $\approx$ 30 % after 10 years of data-taking, though not being able to improve the Borexino best results of ≈ 29 %. On the other hand, in the ideal and Borexino-like scenarios JUNO will match the Borexino best result after 3 years and 2 years of data-taking, respectively.

6.4.2 Impact of ^{11}C background on CNO-ν sensitivity

As for *pep*-ν measurement, the precision on CNO neutrino rate is expected to be strongly dependent on TFC performances. Indeed, as shown in Figure 6.7, the CNO spectrum is overlapped to the ^{11}C one: a high-performance TFC algorithm removes more efficiently the ^{11}C content from the TFC-Subtracted dataset, increasing the CNO signal over background ratio.

We have performed studies in the fit configuration where all the species have been left free to vary, assuming all the three radiopurity scenarios but the IBD one, for the reason clarified in Sec. 6.4.1. The results for CNO-ν precision in the Borexino-like, ideal and baseline scenarios are shown in the top, central and bottom panels of Fig. 6.12, respectively. The color scale represents the CNO neutrinos uncertainties relative to the values obtained when TP = 0.9 and SE = 0.7.

Similarly to what obtained in Sec. 6.3.3, in the Borexino-like and ideal scenarios the Tagging Power is more relevant than the Subtracted Exposure in increasing the ability of the fit to identify CNO neutrinos. Instead, as already found in Sec. 6.3.3, in the baseline scenario the ^{11}C discrimination is not so relevant anymore because of the large amount of other backgrounds present in the detector.

6.4.3 Impact of a *pep*-ν constraint on CNO-ν sensitivity

To enhance the sensitivity on CNO neutrinos, we can constrain the *pep*-ν rate to the value based on the HZ-SSM predictions, i.e. 28.0 ± 0.4 cpd/kton. Since this value differs only of ≈ 1.4 % from the LZ-SSM value, we can safely assume we are not introducing a relevant systematic on the CNO neutrinos rate uncertainty.

The results concerning the CNO-ν relative uncertainty versus the exposure are shown in Fig. 6.13.

In the IBD scenario, JUNO will reach a ≈ 30% precision on CNO neutrinos after 10 years of data-taking, thus not being able to detect them. In the baseline, ideal and Borexino-like scenarios JUNO will achieve the Borexino best results after ≈ 2 years, ≈ 1.1 years and ≈ 1 year of data-taking, respectively. Conversely, after 10 years it will be able to improve the Borexino results, reaching a ≈ 14 %, ≈ 10 % and ≈ 9 % CNO-ν relative uncertainty for baseline, ideal and Borexino-like scenarios, respectively.

6.4.4 Sensitivity results on ^{15}O and ^{13}N neutrinos

Up to now, we have considered the CNO neutrinos as a single species being the sum of the different contributions. As described in Chapter 1 and illustrated in Fig. 1.6, what we refer to as CNO neutrinos is actually the sum of the neutrinos

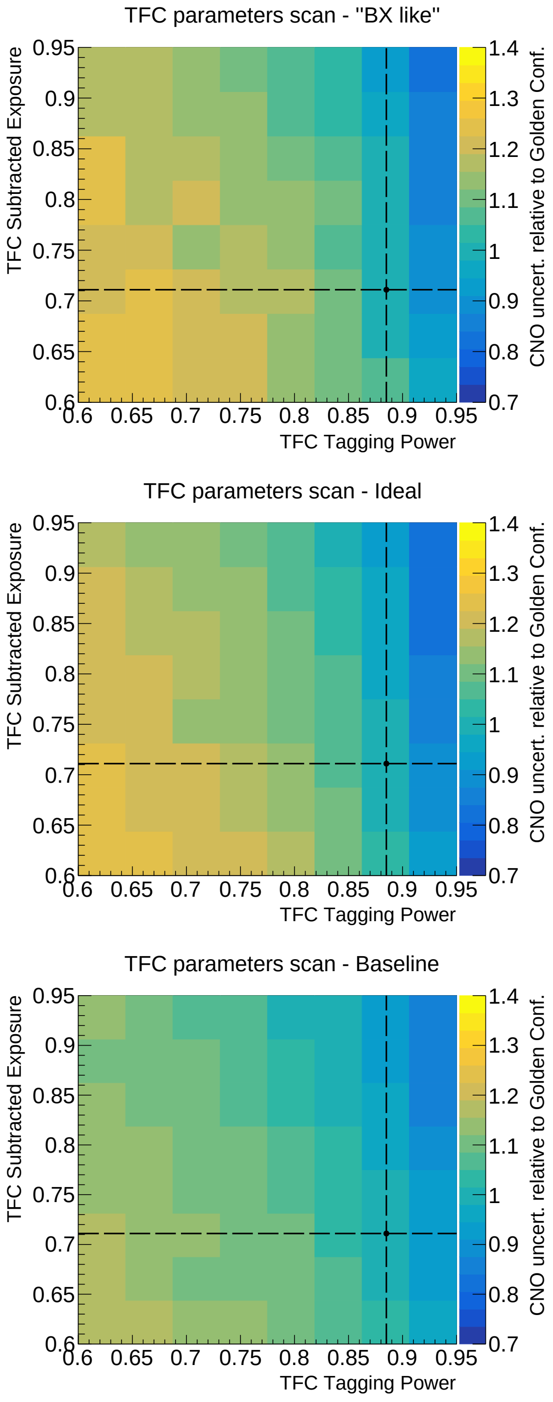

Figure 6.12: The CNO neutrinos rate uncertainties (color scale) as a function of TP (x-axis) and SE (y-axis) after 6 years of data-taking. The z-axis (color scale) represents the CNO neutrinos uncertainties relative to CNO uncertainty when TP = 0.9 and SE = 0.7 (here named *Golden Configuration* for convenience). Borexino-like, ideal and baseline scenarios are respectively shown in top, central and bottom panels.

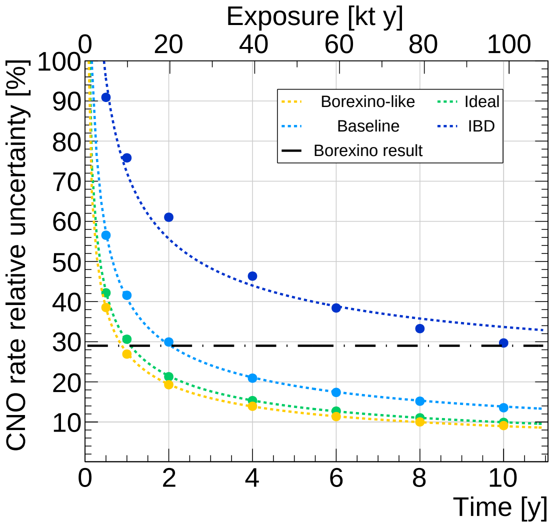

Figure 6.13: *Fit configuration: pep-ν rate constrained to the HZ-SSM value.* The relative uncertainty of CNO neutrino rate as a function of exposure when *pep*-ν rate is constrained in the fit. Borexino-like, ideal, baseline and IBD radiopurity scenario trends are shown respectively in orange, green, light blue and blue dotted lines. The dot markers represent the simulated points. The Borexino best result is reported as the black dashed horizontal line.

coming from ^{13}N, ^{15}O and ^{17}F fusion reactions (see eq. 1.47a, 1.47b, 1.47c). A first measurement of these separate neutrinos fluxes would be important both to have a further test to clear up the solar metallicity problem and to evaluate the nitrogen and oxygen amounts in the core of the Sun.

The goal of this Section is to evaluate the sensitivity on ^{13}N-ν and ^{15}O-ν separately. We have therefore simulated the PDFs of ^{13}N-ν and ^{15}O-ν, neglecting the ^{17}F-ν for two reasons: firstly, it constitutes only the 1 % of the neutrinos coming from the CNO cycle and secondly its energy spectrum is degenerated with the ^{15}O-ν. The ^{13}N-ν and ^{15}O-ν reconstructed energy spectra in the JUNO detecor are pictured in Fig. 6.14 ,together with the full *pep* spectral shape as a comparison.

First of all, we considered the fit configuration where all the species have been left free to vary. The results concerning the ^{13}N-ν and ^{15}O-ν relative uncertainty versus the exposure are shown in Fig. 6.15.

We conclude that after 10 years of data-taking, JUNO will reach a ^{13}N-ν sensitivity of $\approx$ 36 %, $\approx$ 21 % and $\approx$ 17 % in the baseline, ideal and Borexino-like scenarios, respectively. On the other side, in the IBD scenario, being the uncertainty $\gtrsim$ 70% even after 10 years, JUNO will not be able to measure CNO-ν flux. Conversely, for what concerns ^{15}O neutrinos the relative uncertainty achieved will be $\approx$ 34 %, $\approx$ 23 % and $\approx$ 20 % for baseline, ideal and Borexino-like scenarios after a data-taking lasting 10 years. Once again, in the IBD scenario, since the uncertainty is always $\gtrsim$ 60%, JUNO will not be sensitive to a CNO-ν flux measurement.

We have also evaluated the ^{13}N and ^{15}O neutrinos sensitivity when putting a

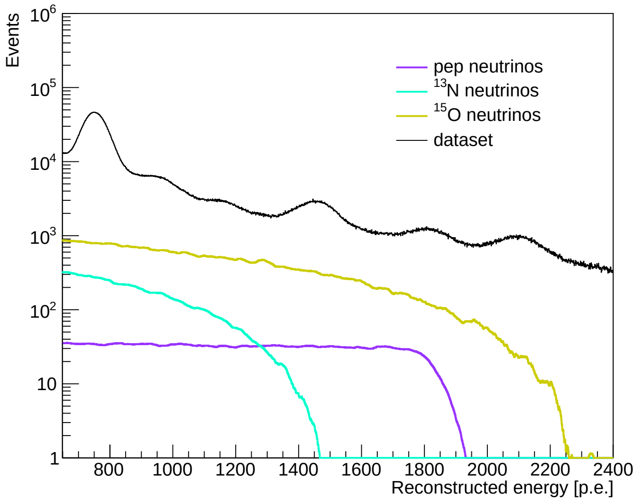

Figure 6.14: ^{13}N-ν, ^{15}O-ν and *pep*-ν reconstructed energy spectra, expressed in photoelectrons. The black line represents the dataset assuming the baseline scenario.

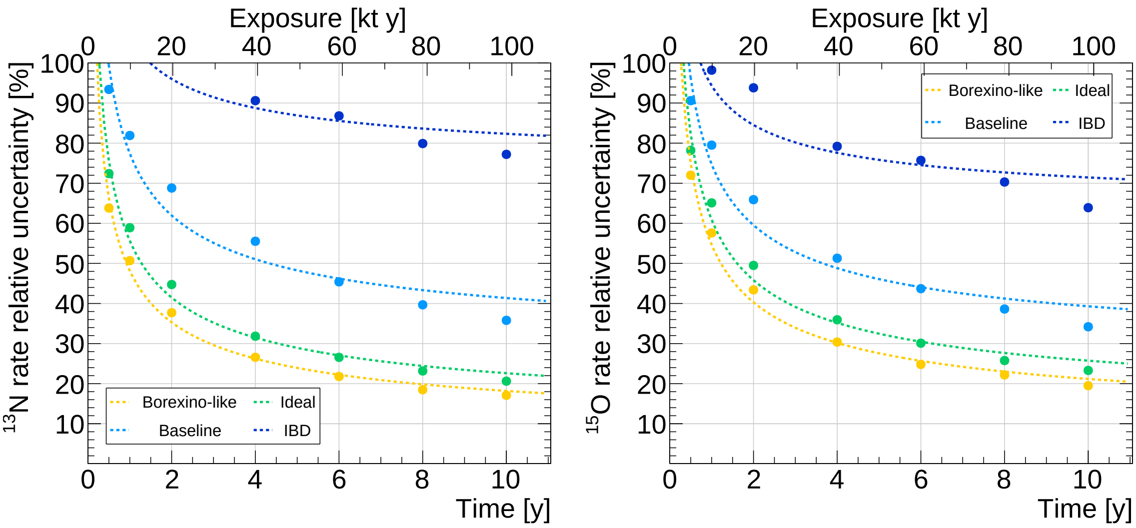

Figure 6.15: *Fit configuration: all species free to vary.* The relative uncertainty of ^{13}N (left panel) and ^{15}O (right panel) neutrino rates as a function of exposure. Borexino-like, ideal and baseline radiopurity scenario trends are shown respectively in orange, green and light blue dotted lines. The dot markers represent the simulated points. The IBD scenario is not displayed since in this case JUNO is not sensitive to ^{13}N and ^{15}O neutrino rates. The uncertainty bands show the uncertainties on the relative uncertainties.

constraint on the *pep*-ν rate. As Fig. 6.14 shows, due to their similar endpoints and spectral shapes, we expect ^{15}O-ν to be more affected by the *pep*-ν constraint than ^{13}N-ν, that have a lower endpoint and an energy spectrum with no peculiar features. This fact is also supported by the correlation plots depicted in Fig. 6.16.

We notice that ^{15}O-ν and *pep*-ν are strongly anti-correlated, while between ^{13}N-ν and *pep*-ν there is no correlation.

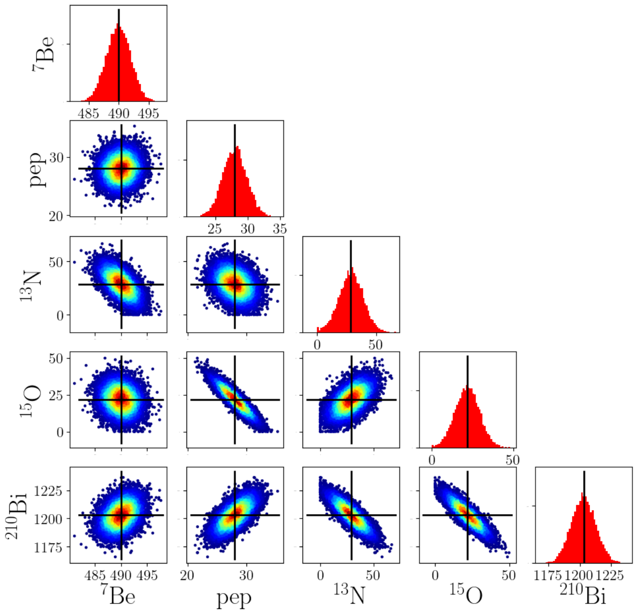

Figure 6.16: Results of the multivariate fits of 10^4 Monte Carlo pseudo-experiments for ^{13}N-ν, ^{15}O-ν, *pep*-ν and ^{210}Bi. The red histograms represent the extracted rate of the species, and are distributed around the injected value (the black lines). The non-diagonal frames show the species correlation plots.

We have thus performed multivariate fits, constraining the *pep*-ν rate to the value 28.0 ± 0.4 cpd/kton (HZ-SSM) and we have evaluated the ^{13}N-ν and ^{15}O-ν sensitivity as a function of the exposure. The results concerning the ^{13}N-ν and ^{15}O-ν relative uncertainty versus the exposure are shown in Fig. 6.17.

By looking at the results, we can conclude that ^{15}O-ν relative uncertainty take more advantage of this constraint than ^{13}N-ν, as expected. In particular, while the ^{13}N-ν results remain almost unchanged with respect to the previous fit configuration, the ^{15}O-ν ones reach $\approx$ 30%, $\approx$ 14%, $\approx$ 10% and $\approx$ 9.5% in the IBD, baseline, ideal and Borexino-like scenarios, respectively, after 10 years of data-taking.

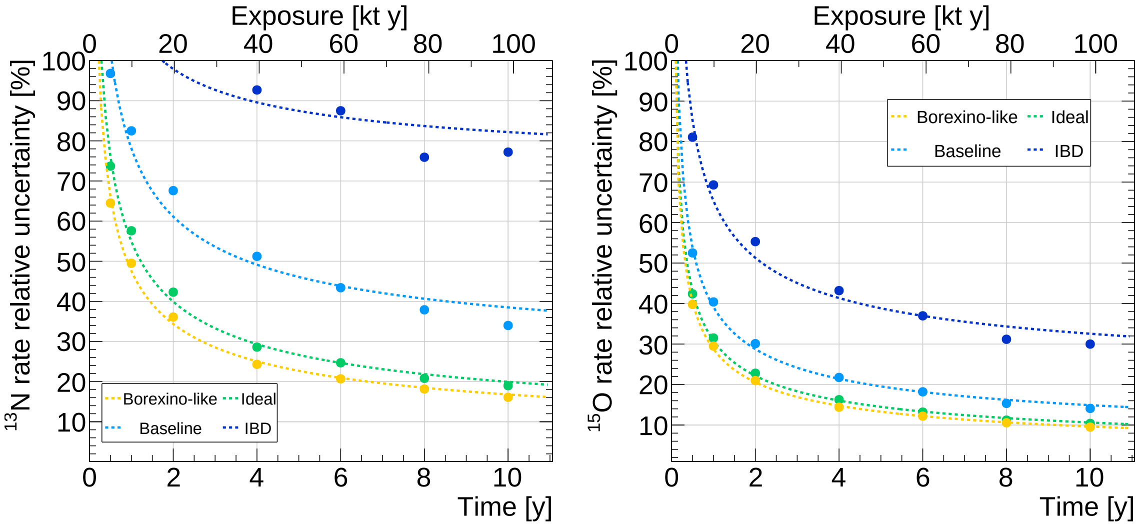

Figure 6.17: *Fit configuration: pep-ν rate constrained to the HZ-SSM value.* The relative uncertainty of ^{13}N (left panel) and ^{15}O (right panel) neutrino rates as a function of exposure. Borexino-like, ideal and baseline radiopurity scenario trends are shown respectively in orange, green and light blue dotted lines. The dot markers represent the simulated points. The IBD scenario is not displayed since in this case JUNO is not sensitive to ^{13}N and ^{15}O neutrino rates.

Conclusions

My thesis work is focused on the solar neutrinos detection with the JUNO experiment. By combining its large volume and high light yield, JUNO has the potential to reach unprecedented levels of precision in the solar neutrinos flux measurement. Before the beginning of the data-taking, a big effort is currently ongoing about sensitivity studies of the ^{7}Be, *pep* and CNO solar neutrinos. This allows us to optimize the methods and to foresee the most crucial aspects impacting the analysis before examining the JUNO data.

During my thesis experience, carried out between Milano and Jülich, I had the opportunity to contribute to many aspects of the analysis. In particular, the first part of my work was devoted to the development of JUST (Jülich nUsol Sensitivity Tool), a software tool for solar neutrino analysis, born in the context of the Jülich research group. It fulfills the dual role to both generate the JUNO toy-datasets and to fit them relying on the optimization of a binned poisson likelihood. Afterwards, I validated JUST against its already existing counterpart developed in Milano, the so-called MUST (Milano nUsol Sensitivity Tool). I performed the validation procedure in two steps. Firstly, I compared the distributions of the events generated for each parameter – both neutrinos and backgrounds – involved in the analysis. Then, I examined the fitter validation by making the two tools fit the same toy-dataset in exactly the same fitting conditions. The results show that the choice of the software tool introduces an irrelevant bias of $\approx 10^{-5}$% on the reconstructed rates, concluding that MUST and JUST are equivalent and appropriate for the solar neutrinos sensitivity analysis.

The second part of my thesis work was devoted to the estimation of the JUNO sensitivity to ^{7}Be, *pep* and CNO neutrinos. The neutrino reconstructed spectral shapes share the energy range with many other sources of background, both internal and cosmogenic. Since the JUNO detector is still under construction, we cannot know the actual radioactive background contamination. Therefore, we have hypothesized a set of four plausible radiopurity scenarios, carrying on the analysis in each of these situations. I have obtained the results by simulating $\approx 10^4$ Monte Carlo toy-datasets and then analyzing the distributions of the neutrino reconstructed rates.

We found that JUNO will be able to measure solar neutrino rates with an uncertainty improved with respect to the current state-of-the-art in the solar neutrino field. Provided that the systematic error will be kept under control, we found that in all the radiopurity scenarios considered, except for the most pessimistic one, the expected uncertainty on ^{7}Be, *pep* and CNO neutrinos will improve the results established by other experiments.

In particular, ^{7}Be neutrinos will be detected with a precision $\lesssim$ 3% even after only 1 year of data-taking in all the radiopurity scenarios. After 6 years, their flux can be measured with a precision $\lesssim$ 0.5% in every radiopurity situation but the worst one.

For what concerns *pep* neutrinos, in the less favorable radiopurity scenario, after 6 years of data-taking, JUNO will improve the current best experimental value ($\approx$ 11%), while this will be improved in all the other scenarios even after only 1 year.

Finally, a competitive CNO neutrinos measurement can be achieved after 6 years, but only in the two most radiopure scenarios. However, due to the strong anti-correlation between *pep* and CNO neutrinos energy spectra, the results can be improved by inserting in the multivariate fit a constraint on *pep* neutrinos rate, based on the Solar Standard Model predictions. Thereby, after 6 years of data-taking, JUNO will improve the existing experimental result, achieving relative uncertainties below $\approx$ 11% in all the radiopurity scenario but the worst one. Furthermore, JUNO will be the first experiment being able to measure separately the neutrino fluxes from the ^{13}N and the ^{15}O fusion reactions, opening new horizons in the understanding of how our Sun's core burns.

In conclusion, the studies I have performed show that the sensitivity to ^{7}Be, *pep* and CNO solar neutrinos fluxes is highly influenced by the radiopurity contamination levels. While the ^{7}Be flux measurement will not be particularly affected by reasonable variations of internal background, keeping the radioactivity levels under control will be crucial for the determination of *pep* and CNO neutrinos fluxes. Nonetheless, from the results of my studies we can safely assume that JUNO plays a leading role in the next generation of solar neutrinos spectroscopy detectors.

Appendices

APPENDIX A

JUST: Jülich nUsol Sensitivity Tool

JUST (Jülich nUsol Sensitivity Tool) is a software tool developed for JUNO solar neutrinos analysis [78].

The philosophy behind JUST led to the development of a highly modular and customizable tool for easy integration of prospective features. The analysis strategy is based on Monte Carlo PDFs which are used both to generate the pseudo-datasets and to fit them. It is also based on a binned poisson likelihood optimization of two independent histogram representing two different datasets. More in detail, considering a histogram with k bins labelled with $i = 1, ..., k$, where each bin contains n_i events, the likelihood is given by

$$\mathcal{L}(\vec{n}|\vec{\lambda}) = \prod_{i=1}^{k} \frac{e^{-\lambda_i}\lambda_i^{n_i}}{n_i!} \tag{A.1}$$

where λ_i is the number of events expected in the i-th bin. In the current version, two independent histograms (*Subtracted* and *Tagged*) are simultaneously fitted, so the likelihood involved is given by the product of the two likelihoods $\mathcal{L} = \mathcal{L}_{\text{Sub}} \cdot \mathcal{L}_{\text{Tag}}$. More details about the solar neutrino analysis can be found in Chapter 4.

A.1 JUST architecture

The architecture of JUST is fully modular, meaning that any module can in principle be removed and replaced if needed, making testing and development seamless. All modules are called by *Main.cpp* that acts as an organiser. The modules are called in the following order:

1. *Parser.cpp* that reads the configuration files and the command line arguments;
2. *DataReader.cpp* that opens the different ROOT files to process data and PDFs;
3. *ToyDataGenerator.cpp* that creates a generator for pseudo-data to be used in the fitter;
4. *Fitter.cpp* that either carries out a fit on data, or iteratively calls the ToyDataGenerator and then fits each newly obtained dataset by using TMinuit;

5. *FitResults.cpp* that processes the results by extracting the quantities of interest: the reconstructed rates, the covariance and correlation matrices, the χ^2/NDF, etc.;
6. *OutputManager.cpp* that finally create plots and write all necessary output. An example of the JUST output plots is given in Fig. A.1.

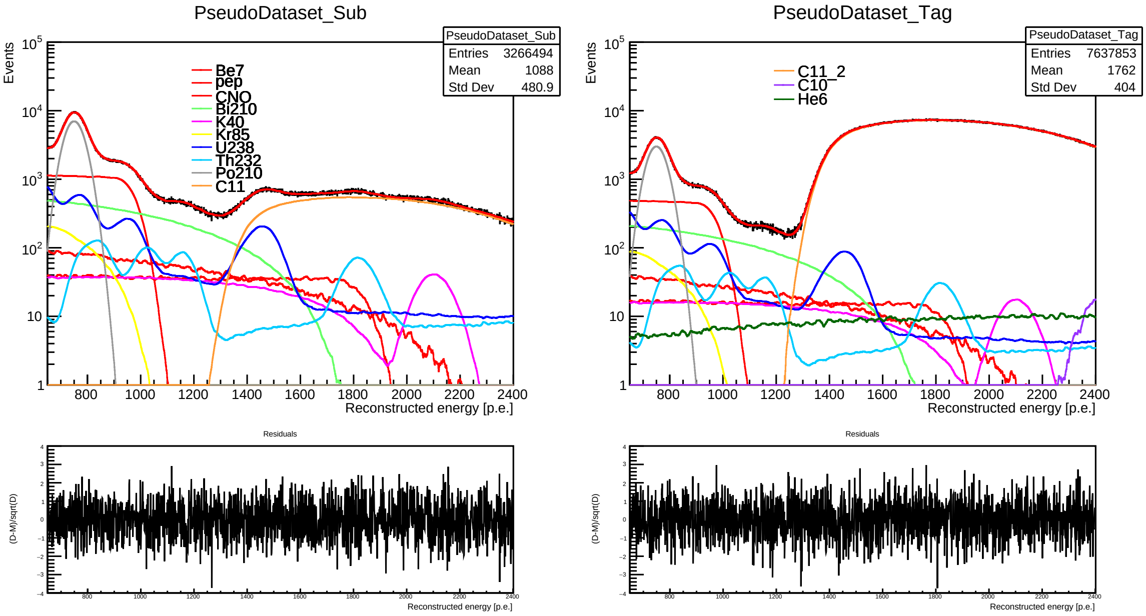

Figure A.1: Example of the output of JUST for a multivariate fit on a pseudo-dataset generated in the ideal radiopurity condition. The TFC-subtracted (left) and the TFC-tagged (right) energy spectra are shown together with residuals. The sum of the individual components from the fit (red line) is superimposed on the data (black points). The residuals are calculated as the difference between the data bin content and the fit result for each bin, divided by the square root of the data bin content.

As mentioned above, the *Main.cpp* organizer only contains the core of the procedure and it calls some functions belonging to other modules. Its frame can be summarized as following.

A *NuFitConfig* object, responsible for managing all the details coming from the configuration files, is created. The PDFs are then read and analyzed by a *NuFit-PDFs* object. After these preliminary actions have been fulfilled, two different and exclusive way can be covered. If toy fits have been requested through the configuration files, the pseudo-data are sampled and fitted. On the contrary, if a real data fit has been chosen, then an analogous function is called only to fit the input data. In both cases, a *NuFitResults* object with all the needed results is finally created.

Before moving on to the following sections containing more details about each one of the modules, it's worth pointing out some key peculiarities of JUST. This software has been thought to be as customizable as possible, so that in principle it could be used to fit as many histograms as the user wants. One useful way to

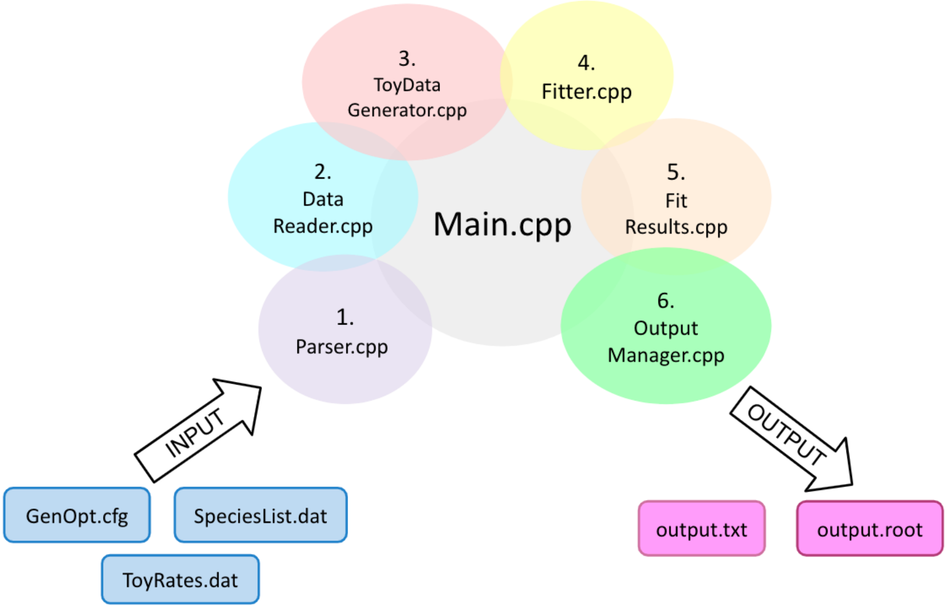

Figure A.2: Schematic depiction of JUST architecture, together with the input and output files needed.

achieve this goal consists in exploiting std::vector variables to store lists of quantities available in each of the histograms. By doing so, it's easy and natural to extend the code the let it fit N histograms. Furthermore, using std::vector variables leads to a speed-up of about a factor three in the fitting process.

A.2 How to install and run JUST

JUST is written with the C++14 programming language, so the compilers and ROOT must be recent enough to reflect this. The minimum requirements needed are gcc 9.3.0, cmake 3.4.1 and ROOT 6.22. After carefully checking to fulfill all the requirements, JUST can be downloaded writing the following command in a new terminal window:

```
git clone https://jugit.fz-juelich.de/a.goettel/nu-solar-fitter.git
```

After that, it's necessary to move to the proper branch through the command:

```
git checkout BranchName
```

Finally, after moving to the folder `nu-solar-fitter`, JUST can be easily installed with the command:

```
./RebuildAndInstall_sh.sh
```

Once the JUST installation has been successfully completed, the executable file is located at the `nu-solar-fitter/install/bin` folder. With the commands

`./NuSolarFit --help` or `./NuSolarFit -h` it's possible to have an overview about all the options needed or available to run it. For convenience, they are also briefly reported here.

- `--general-options` or `-g`, followed by the path to the text file containing all the fit general options (the so-called `gen_opt.cfg`, see Section A.3);
- `--species-list` or `-s`, followed by the path to the text file containing the list of the parameters with which to fit the dataset (the so-called `species_list.dat`, see Section A.3);
- `--toy-rates` or `-t`, followed by the path to the text file containing the information for the toy Monte Carlo generation (the so-called `toy_rates.dat`, see Section A.3). In this case, as toy Monte Carlo generation we mean the production of the two pseudo-datasets to be fitted;
- `--output` or `-o`, followed by the path to the output files, *without* the file extension since by default both the text and the ROOT [70] files will be created.

Depending on the dataset to be fitted – real or Monte Carlo – JUST can be run in two different ways, reported below as an example. In fact, when Monte Carlo studies want to be performed, JUST takes also care of the toy generation.

- *Real dataset fit*: only three arguments are needed.

```
./NuSolarFitter -g gen_opt.cfg -s species_list.dat -o output
```

- *Pseudo-dataset fit*: in addition to the previous case, the configuration file for the toy generation has to be added. When performing Monte Carlo sensitivity studies, N simulations must be run in order to look at the results' distributions obtained. The information about N is included in the `gen_opt.cfg`, as we will see in Sec. A.3.1, and not parsed through the command line.

```
./NuSolarFitter -g gen_opt.cfg -s species_list.dat -t toy_rates.dat -o output
```

A.3 Configuration files

In order to successfully run JUST, three different configuration files have been designed: `gen_opt.cfg`, `species_list.dat` and `toy_rates.dat`.

In all these files, comments are allowed: they can be simply added by inserting the # character at the beginning of the commented line.

A.3.1 `gen_opt.cfg`

The `gen_opt.cfg` configuration file has the structure depicted in Fig. A.3. The first column contains the labels representing some specific information needed to run the fit, the order of them doesn't matter. The second column contains the values of the parameters specified on the left. There are both mandatory labels and optional ones. Let's focus now on the mandatory ones.

- PDFsRootfile, which contains the path to the ROOT file including the PDFs, both those to fit and those to sample the dataset if Monte Carlo fits are done (of course with different names if they are different).
- DataRootfile, which contains the path to the ROOT file including the dataset. If Monte Carlo pseudo-datasets are generated, this line can still be included but JUST will ignore it.
- HistOne and HistTwo, i.e. the names of the two histograms simultaneously fitted. When a dataset is given as an input these names have to be the same as the ones in the dataset ROOT file.
- Lifetime, i.e. is the data-taking interval expressed in days.
- TargetMass, i.e. the fiducial volume mass expressed in kton. Please note that instead of this flag it is possible to insert separately the density of the liquid scintillator and the radius (respectively, LSDensity_g/mL and Radius_m) so that the mass is then internally calculate in the software. In the latter case, the TargetMass line must be commented. If all these three labels are included in the file, then only the value after the label TargetMass is considered.
- emin and emax, which are respectively the fitting range starting point and endpoint in *number of photoelectrons*.
- ToyData, which is an integer variable related to the toy data generation: the user must write 0 if a real dataset will be fitted or an integer N it N toy data fits are going to be performed. E.g, if ToyData is 100, then 100 Monte Carlo simulations are run.
- Hesse and Minos, which are both boolean variables ($0 = $ no and $1 = $ yes) related to some TMinuit [79] functionalites. Particularly, Hesse is used to perform a full calculation of the Hessian matrix for error calculation, while Minos to calculate parameter errors taking into account both parameter correlations and non-linearities.
- Likelihood, which contains the name of the likelihood we want to do the fit with: up to now, only the *poisson* one is implemented.

```
PDFsRootfile        PDFs.root
DataRootfile        dataset.root
HistOne             PseudoDataset_Sub
HistTwo             PseudoDataset_Tag
Lifetime            365
TargetMass          9.87338
emin                650
emax                3000
ToyData             100
Hesse               0
Minos               0
Likelihood          poisson
#optional
LSDensity_g/mL      0.859
Radius_m            14
seed                1111
DAQTime             0.75
```

Figure A.3: Configuration files: `gen_opt.cfg`

Finally, for what concerns the the optional labels, the seed and the DAQTime ones give the user the possibility to respectively choose a specific seed for the toy generation and to select a suitable DAQ time window. If they are not included, the seed is randomly chosen by JUST and the DAQ time is by default set to 1.

A.3.2 `species_list.dat`

The `species_list.dat` configuration file contains all the information necessary to the fitting procedure itself: the list of the species involved and other important parameters linked to them, like the initial guesses or the possibility to let them free to vary or fix in the fit. An example of the `species_list.dat` is given in Fig. A.4. This file is structured in two horizontal blocks (#TFC_Sub params and #TFC_Tag params), each one of them associated to one of the histograms to be fitted. In the following I will make a list of all the labels present in this file.

- pdf contains the names of the PDFs exploited to perform the fit;
- param represents the names of the parameters involved, which can be different from the names of the PDFs. As a clarifying example, we mention the ^{11}C case. The names of the PDFs are both “C11”, since both the histograms

```
#pdf            param   guess   lower   upper     step  fixed  hist_id  eff
#TFC_Sub params
Be7             Be7     490     0       4.9e+03   10    0      1        5.1177e-01
pep             pep     28      0       2.8e+02   10    0      1        6.0328e-01
CNO             CNO     50.3    0       5.0e+02   8     2      1        5.5376e-01
Bi210           Bi210   241     0       2.4e+03   10    0      1        5.5769e-01
K40             K40     22.9    0       2.3e+02   10    0      1        6.4434e-01
Kr85            Kr85    100     0       1.0e+03   10    0      1        4.7537e-01
U238            U238    150.5   0       1.5e+03   10    0      1        5.7733e-01
Th232           Th232   35.08   0       3.5e+02   10    0      1        6.3320e-01
Po210           Po210   244.2   0       2.4e+03   10    0      1        7.0544e-01
C11             C11     1916    0       1.9e+04   10    0      1        6.9474e-02
#TFC_Tag params
Be7             Be7     490     0       4.9e+03   10    0      2        2.1933e-01
pep             pep     28      0       2.8e+02   10    0      2        2.5855e-01
CNO             CNO     50.3    0       5.0e+02   8     2      2        2.3732e-01
Bi210           Bi210   241     0       2.4e+03   10    0      2        2.3901e-01
K40             K40     22.9    0       2.3e+02   10    0      2        2.7615e-01
Kr85            Kr85    100     0       1.0e+03   10    0      2        2.0373e-01
U238            U238    150.5   0       1.5e+03   10    0      2        2.4743e-01
Th232           Th232   35.08   0       3.5e+02   10    0      2        2.7137e-01
Po210           Po210   244.2   0       2.4e+03   10    0      2        3.0233e-01
C11             C11_2   1916    0       1.9e+04   10    0      2        9.2301e-01
C10             C10     37.1    0       3.7e+02   10    0      2        2.9966e-01
He6             He6     27.8    0       2.8e+02   10    0      2        2.9772e-01
```

Figure A.4: Configuration files: `species_list.dat`. Example for solar neutrino analysis according to Ref. [60].

use the same PDF. However, the parameters' names are different ("C11" and "C11_2"): that's why they are considered as independent parameters.

- guess is the initial guess, also called injected rate, in cpd/kton. It represents the starting value for the fit from which then search for the best rate.
- lower and upper define the boundary rates (in cpd/kton) allowed for each species.
- step is the starting step size in cpd/kton.
- fixed is an integer value telling the fitter if the parameter is left free to vary (0), fixed (1) or constrained (2). In the latter case, the parameter is confined to a gaussian with mean equal to the initial guess and standard deviation equal to the step.
- hist_id indicates which histogram the parameter belongs to.
- eff is a number including the information related to the integral of the PDF and the TFC parameters (Tagging Power TP and Subtracted Exposure SE). To be more accurate, eff is calculated differently according to the histogram considered (*Sub* or *Tag*), thus leading to have the following two formulas:

$$\mathsf{eff}_{\text{sub}} = \text{Integral of the PDF} \cdot \text{SE} \tag{A.2a}$$
$$\mathsf{eff}_{\text{tag}} = \text{Integral of the PDF} \cdot (1 - \text{SE}) \tag{A.2b}$$

It's important to notice that eqs. A.3a and A.3b apply to every species but ^{11}C due to the fact that ^{11}C is also linked to the TP. Therefore, we have:

$$\mathsf{eff}^{11\text{C}}_{\text{sub}} = \text{Integral of the PDF} \cdot \text{SE} \cdot (1 - \text{TP}) \tag{A.3a}$$
$$\mathsf{eff}^{11\text{C}}_{\text{tag}} = \text{Integral of the PDF} \cdot (1 - \text{SE} \cdot (1 - \text{TP})) \tag{A.3b}$$

This is a temporary solution: another way to deal with this is currently on work. The idea is to have clearly specified somewhere the values of SE and TP, and not hidden in the eff values.

A.3.3 `toy_rates.dat`

The `toy_rates.dat` configuration file needs to be added only if the user wants to perform fits on toy datasets. In fact, it contains all the details to generate the pseudo-datasets. A `toy_rates.dat` example is reported in Fig. A.5. This file contains some of the columns already present in the `species_list.dat`: the ones not related to the fitting process. Having these two separate configuration files allows to fit the same data under different model assumptions, and vice-versa.

```
#pdf              guess      hist_id    eff
#TFC_Sub params
Be7               490        1          5.1177e-01
pep               28         1          6.0328e-01
CNO               50.3       1          5.5376e-01
Bi210             241        1          5.5769e-01
K40               22.9       1          6.4434e-01
Kr85              100        1          4.7537e-01
U238              150.5      1          5.7733e-01
Th232             35.08      1          6.3320e-01
Po210             244.2      1          7.0544e-01
C11               1916       1          6.9474e-02
#TFC_Tag params
Be7               490        2          2.1933e-01
pep               28         2          2.5855e-01
CNO               50.3       2          2.3732e-01
Bi210             241        2          2.3901e-01
K40               22.9       2          2.7615e-01
Kr85              100        2          2.0373e-01
U238              150.5      2          2.4743e-01
Th232             35.08      2          2.7137e-01
Po210             244.2      2          3.0233e-01
C11               1916       2          9.2301e-01
C10               37.1       2          2.9966e-01
He6               27.8       2          2.9772e-01
```

Figure A.5: Configuration files: `toy_rates.dat`. Example for solar neutrino analysis according to Ref. [60].

A.4 JUST modules

A.4.1 Parser

The *Parser* module is responsible for reading the arguments parsed in the command line and storing the configuration files' contents. It is divided into two blocks, each one characterized by the relative class and described below.

The *NuFitCmdlArgs* class is responsible for the command line arguments analysis. It contains variables where the files' names written in the command line are saved through the function CMDLParser::Parse.

On the other hand, the *NuFitConfig* class contains all the variables needed to store the quantities included in the configuration files, other than three specific functions able to read and analyze those quantities (ParseGenOpts, ParseSpeciesList and ParseToyRates). All these functions are called while invoking the constructor for *NuFitConfig*. While doing this, a careful error handling is carried out by assuring that the configuration files quantities are given in the correct format (i.e. TargetMass has to be positive, etc.).

If toy fits are requested, this module takes also care of part of the pseudo-datasets generation. By using the generator provided in the TRandom ROOT class, it gaussianly samples the number of events for each of the species involved in the histograms. Then, it saves these values in a std::vector⟨std::vector⟨unsigned int⟩⟩ variable. This variable can be seen as a $n \times m$ matrix, where n is the number of the pseudo-datasets, while m the total number of the species included in all the histograms (e.g. if there are two histograms and both of them include the same species, then this is counted twice). Fig. A.6 illustrates a sketch of this std::vector⟨std::vector⟨unsigned int⟩⟩ variable. This will be used later on in the *ToyDataGenerator.cpp* module for the next steps of the toy generation.

Then, a *paramVector_toy* object is created to better re-arrange the species information with respect to how it was stored previously. A *paramVector_toy* object is a std::vector⟨std::vector⟨NuFitter::paramData⟩⟩ variable, where NuFitter::paramData is a struct which includes two unsigned int, variables representing the PDF and the histogram indexes. Ultimately, a *paramVector_toy* will be a $s \times p$ matrix, where s is the number of the histograms to be fitted and p is an integer representing how many different PDFs are involved. As an example, given a `species_list.dat` structured as the one in Fig. A.4, *paramVector_toy* would be like the one sketched in Figure A.7. The *paramVector_toy* object will be very useful to loop over some quantities in the next steps of the toy data generation (see Section A.4.3).

The last goal of this module is to extract the number of bins either from the input dataset – if a real data fit is done – or from the PDFs, if Monte Carlo fits are chosen. This number is needed later by both *DataReader.cpp* and *ToyDataGenerator.cpp* modules to convert histograms into std::vector.

Finally, thanks to the *Parser*, JUST is able to warn you if the input files contain a wrong number of arguments, as well as notify you if issues in opening or reading them happen. This latter action is a matter for the NuFitter::ErrorReading function,

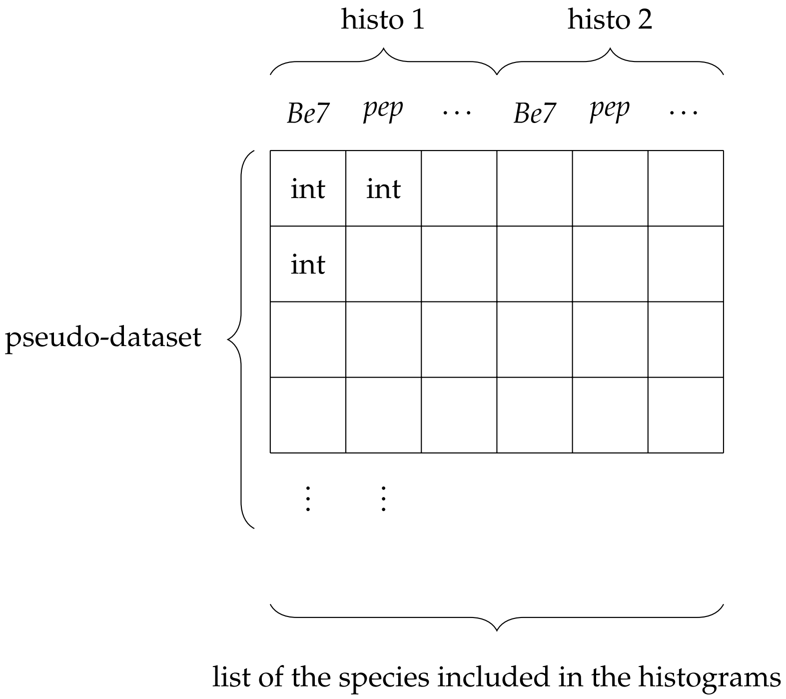

Figure A.6: A sketch of the std::vector⟨std::vector⟨unsigned int⟩⟩ variable. Here, *int* is an abbreviation used for *unsigned int*.

which also includes a NuFitter::HelpMessage function, easily referrable to with the flags `--help` or `-h` (see Section A.2), giving you useful information about how to run the software.

A.4.2 DataReader

The *DataReader* module reads the input ROOT files with the PDFs and the data, and save them in suitable variables. Furthermore, it is responsible for the conversion of all the histograms into std::vector objects. Since many variables previously stored are now actually used, it also includes *Parser.h*.

It is divided into two classes: *NuFitPDFs* and *NuFitData*, which respectively take care of data and PDFs, as suggested by the names. *NuFitPDFs* includes the members listed below, needed to properly save all the information from the input file. Therefore, we have:

- *pdf_histograms*, a std::vector⟨TH1D* ⟩ variable, whose size is equal to the total number of the PDFs, where each entry contains the ROOT TH1D histogram of the PDF.

- *pdfs* is a std::vector⟨std::vector⟨double⟩⟩ variable implemented to deal with PDFs. More in detail, the function NuFitPDFs::Read reads the PDFs from the input file and guarantees that they are properly normalised to 1. Then, it fills the

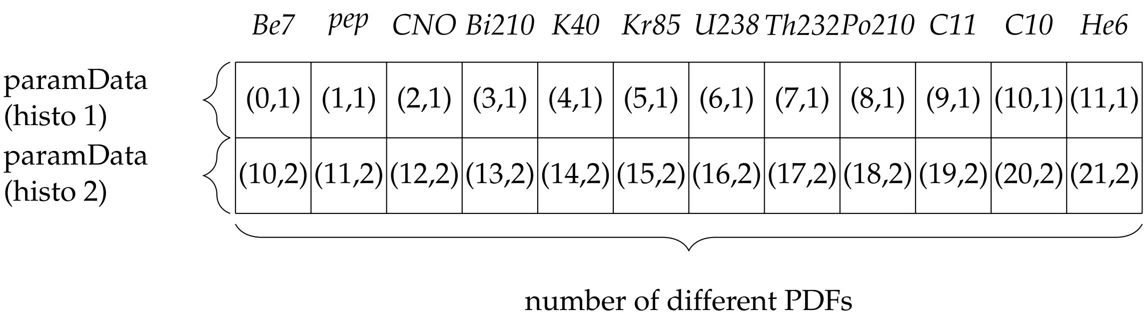

	Be7	pep	CNO	Bi210	K40	Kr85	U238	Th232	Po210	C11	C10	He6
paramData (histo 1)	(0,1)	(1,1)	(2,1)	(3,1)	(4,1)	(5,1)	(6,1)	(7,1)	(8,1)	(9,1)	(10,1)	(11,1)
paramData (histo 2)	(10,2)	(11,2)	(12,2)	(13,2)	(14,2)	(15,2)	(16,2)	(17,2)	(18,2)	(19,2)	(20,2)	(21,2)

Figure A.7: A sketch of a *paramVector_toy* object. Each cell contains a paramData variable. A paramData variable is a pair of integers (a, b), where a is the index of the PDF (referring to the `species_list.dat` in Fig.A.4, this index is incremented every time a new entry in the first column is read) and b is the index of the histogram (1 or 2).

variable *pdfs* which represents the PDFs already converted into std::vector. This can be seen as a matrix $e \times f$, where e is the total number of PDFs and f is the number of bins own by all the PDFs. As an example, the cell 1×1 contains the number of events included in the first bin of the first read PDF, the cell 1×2 is referred to the second bin of the first read PDF and so on.

- *bin_edges* is another std::vector⟨std::vector⟨double⟩⟩ variable. It can be seen as a matrix $g \times h$, where again g is the total number of PDFs, but now h is equal to the number of bins plus one[1]. The edges are obtained with a suitable function called NuFitter::getBinEdges. This variable will be exploit a lot in the *Fitter.cpp*.

The second class of *DataReader.cpp* is called *NuFitData* and its structure is very similar to *NuFitPDFs*. Analogously to what already written, it has *data_histograms*, *data* and *bin_edges* members, which carry out the same purpose of the ones in *NuFitPDFs*, but using the data histograms instead of the PDFs. Furthermore, this class has an extra std::vector⟨unsigned int⟩ variable called *hist_ids*, where the histograms' indexes are stored, starting from 1. A NuFitData::Read function is also included to read and analyze the dataset and properly fill all the variables mentioned before.

A.4.3 ToyDataGenerator

The *ToyDataGenerator* module, invoked only if toy fits are requested, is devoted to fulfill the main steps of the toy Monte Carlo generation, already begun in *Parser.cpp*.

The toy steps are carried out by the class *NuFitToyData*. By calling its constructor, all the members are filled. Particularly, the std::vector⟨TH1D*⟩ variable is filled with empty TH1D histograms, properly named and binned. Then, also *bin_edges* and *hist_ids* are analogously treated according to what already described in Section A.4.2.

---

[1] It contains the low edges of each bin plus the up edge of the last bin.

Anyway, the core of the *ToyDataGenerator* is the `NuFitToyData::loadDataset` function, a `void` type function taking as unique argument the index of the pseudo-dataset generated in *Parser.cpp*. This function serves the purpose to fill the histograms with the number of events sampled earlier in *Parser.cpp*. Then, the TH1D histograms included in the `std::vector⟨TH1D*⟩` variable are randomly filled, by using the contents of the existing PDFs, for an amount of times equal to the number of events sampled previously in *Parser.cpp*. After that, in order to speed up the fitting procedure, these histograms are converted into `std::vector` variables, as already done in *DataReader.cpp*.

Nevertheless, the `NuFitToyData::loadDataset` function is not invoked in the *ToyGenerator.cpp*, but in the *Fitter.cpp*. This is due to the fact that the pseudo-datasets are produced on the fly, immediately fitted, and then destroyed in order to save memory. After each of the N calls, a `std::vector⟨std::vector⟨double⟩⟩` variable containing the datasets is created. This is essentially a $m \times n$ matrix, where m is the number of independent histograms (in most of our cases, *Sub* and *Tag*) and n is the number of bins. For the sake of transparency, let's give an example. The first cell $-\ 1 \times 1\ -$) will contain the total number of entries - i.e. the sum of the number of events from all the PDFs in the first bin - of the first bin of the *Sub* histogram, i.e. histogram number 1.

A.4.4 Fitter

The *Fitter* module represents the core of JUST and it deals with the fitting procedure. It includes all the previous modules, as well as *FitResults.h*, which is thoroughly described in Section A.4.5. The fit is performed by using TMinuit and a double negative log-likelihood, described in a separate `fcn` function, is minimized.

This module includes two classes:

- *NuFitContainer* contains all the ingredients – both variables and functions – invoked in the next class, the *MinuitManager* indeed.
- *MinuitManager* supervises all the steps of the fitting procedure

Besides these two classes, we also find two `Fit` functions – one for real data and one for the toy Monte Carlo fits – and the `fcn` function, used by TMinuit to sample the likelihood.

Let's now briefly report how the *Fitter.cpp* works. At the beginning, two useful functions are declared: `MultiplyVectorByScalar`, which multiplies by a scalar all the entries of a vector, and `getIndexOf`, which returns the index of a vector element. To make them as flexible as possible, they have been implemented as template functions.

Then, we have the *NuFitContainer* implementation. Some preliminary functions are included and now concisely commented:

- NuFitContainer::InFitRange is a boolean function that assures whether the two arguments are smaller or greater than emax and emin, respectively. This is helpful to be sure that we are fitting precisely the range requested by the user.
- NuFitContainer::setData and NuFitContainer::convertToVec[2] are responsible for converting the region of the histograms included in the fitting range into C++ vectors.

Afterwards, the NuFitContainer constructor takes care of the creation of new PDFs objects, with applied fit range cuts. Moreover, to make the fit more stable during the error matrix calculation, this constructor separates the contributions of the free and the fixed parameters, by creating an index map. In fact, in Minuit, when a FIX command is used, the calculation of this matrix is performed as follows[79]: Minuit creates a preliminary error matrix, then inverts it, removes the fixed parameters and inverts it back. To avoid this process which may cause some issues, we introduced an index map between all the parameters and the Minuit fit parameters. By doing so, Minuit sees only the free parameters. Then, the map is used to add the fixed parameters directly to the fit function, without going through Minuit itself. Afterwards, Minuit calculates the error matrix of all the free parameters without doing the double inversion and add the corresponding lines later on.

The core of the NuFitContainer class is composed of the following functions:

- NuFitContainer::fitFunction calculates the fit function for a set of parameters and returns as output a std::vector⟨std::vector⟨double⟩⟩ variable containing the values of the fit function. Fixed parameters – if any – are added in the end.
- NuFitContainer::getChiSquare calculates the χ^2/NDF for a given set of parameters.
- NuFitContainer::NLL represents a container for the likelihood calculation, called then in the fcn function (see later in this Section). To let the NLL function take as input any type function, it has been thought to be a template⟨typename L⟩ function. Its implementation is based on [80]. Particularly, by looping over the data, it evaluates the input template function by using the output of the already mentioned fitFunction and the data.
- NuFitContainer::NLL_poisson is the function where the Poisson formula is explicitly written.

Before moving on to the description of the *MinuitManager* class, it is worthwhile to illustrate how the fcn function works. This function is mandatory to call Minuit and it represents the function to be minimized. In JUST, it makes use of a *NuFitContainer* pointer object called fitCtnr and declared at the beginning of this module.

---

[2] NuFitContainer::setData simply calls NuFitContainer::convertToVec.

Through it, we call the NLL function and we pass it a lambda expression as the first argument. Lambda expressions have been introduced in C++11 to allow the developers to write an in-line function, which can be used for short snippets of code that are not going to be re-use and not worth naming. In our case, these have been thought to be functions which call NLL_poisson or other likelihoods that could be introduced in the future. In case of parameter constraints, the fcn function takes care of the addition of Gaussian pull-terms.

Let's focus now on the *MinuitManager* class implementation. Besides the trivial constructor and destructor, we have the following functions:

- MinuitManager::initMinuit creates a new Minuit instance and set the fcn function. Then it parses the parameter information to Minuit through the Minuit function mnparm, which as inputs requires the following information: the parameter number, the parameter name, the fitting starting value and step size (or uncertainty) and the lower and upper bounds on the parameter value itself.

- MinuitManager::resetMinuit simply resets the fit results to prepare for a new fit.

- MinuitManager::callMinuit starts the minimization process by executing the Minuit commands. Firstly, it calls MIGRAD (plus SIMPLEX if MIGRAD fails). Furthermore, there are two more options only activated if specified in the `gen_opt.dat` configuration files: HESSE and MINOS, for exact non-linear errors calculation.

- MinuitManager::getResults converts the fit results into vectors and stores them into member variables, giving as output a *NuFitResults* object. Among the variables stored, we find the best values given by the fit, the covariance matrix and the χ^2/NDF.

Finally, the last part of the *Fitter* module is made up of two pairs of the functions doFit and Fit. The first pair deals with real dataset fits and both of the functions return NuFitResults objects. More in detail, the Fit function simply represents a container for the doFit function. The latter one includes the instructions necessary to actually perform the fit: updating the data used for the fit, preparing Minuit, starting the minimization and finally returning the results.

The second pair of these functions is associated to the multiple toy data fits. Particularly, instead of returning NuFitResults objects, they return std::vector⟨NuFitResults*⟩ objects, where each entry is devoted to a particular toy data fit. To achieve this goal, doFit loops over the number of pseudo-datasets, each time invoking the loadDataset function.

A.4.5 FitResults

The aim of the *NuFitResults* module is to process the results returned by the fit to extract the quantities of interest, handled afterwards by the *OutputManager*, the last module. After the constructor and destructor definitions, we have the three functions briefly described hereafter:

- NuFitResults::combineParamVectors gives as output a std::vector⟨std::vector⟨paramData⟩⟩ object, i.e. a *paramVector*, where also fixed and constrained parameters are included. This function is called in the constructor to build a comprehensive *paramVector* object.
- NuFitResults::getUncertainties returns the uncertainties calculated as the square roots of the covariance matrix eigenvalues.
- NuFitResults::getCorrMatrix calculates the correlation matrix starting from the covariance matrix.

A.4.6 OutputManager

The *OutputManager* is the last module invoked by JUST and it deals with the creation of plots and the transcription of all the necessary results on output files.

JUST gives as output a text file and a ROOT file. The first one contains many useful information about the fit performances: its status (success or fail), the fit results both in counts and in cpd/kton, the covariance and the correlation matrices, the χ^2/NDF and finally some relevant input parameters, including the exposure and the fitting range. If multiple toy data fits are requested, then the text file will contain all these details for each single simulation performed.

On the other hand, in the output ROOT file we have the following elements. First of all, two TTrees: the *FitResults*, containing the χ^2/NDF distribution and the distributions of the results returned by the fit (both in counts and in cpd/kton)[3], and the *ToyGeneration*[4], which contains the distributions of the generated events, species by species (both in counts and in cpd/kton).

We then have the *parameters* folder which includes the *Parameters* and *Config* TTrees. The *Parameters* TTree has a branch for each species with six leaves each, representing some useful input details, such as the injected rate (in counts and cpd/kton), the step size, the lower and upper limits, and finally a variable telling if the species has been fixed, constrained or let free to vary. Conversely, the *Config* TTree has four leaves representing the following quantities: the exposure, the starting and endpoint fitting limits and the seed chosen for the toy generation (if not explicitly specified in the configuration files, this is randomly picked up).

---

[3] If a single dataset if fitted, of course we will not have the results' distributions but the single fit best values with their uncertainties.

[4] The *ToyGeneration* TTree is present only if toy fits are done.

Finally, the output ROOT file includes two canvas. The *Plot* canvas, shown in Fig. A.1 and representing the fitted spectra (*Sub* and *Tag*) in number of events versus the reconstructed energy with the residuals. In this case, if multiple toy fits are done, then only the plot related to the last fit is stored to save disk memory. The second canvas is the so-called *PDFs*, which contains two sub-canvas referring to the PDFs used as the model (if toy fits are requested) and the ones used to fit the data.

An example of the JUST output ROOT file, showing the distribution of ^{7}Be neutrinos reconstructed rates is depicted in Fig. A.8, together with a sketch of the elements belonging to the output file itself, here named *fit.root*.

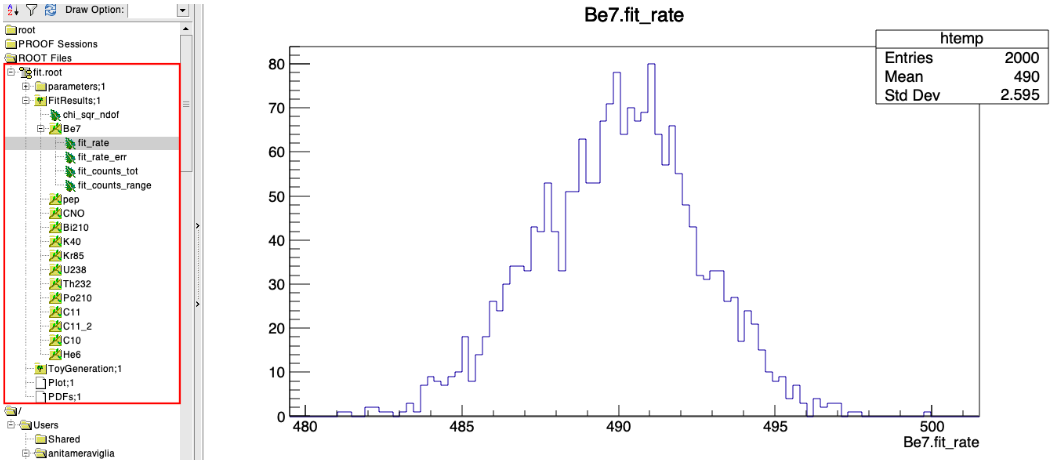

Figure A.8: Overview of the JUST output ROOT file named *fit.root* (left, red box) and the ^{7}Be neutrinos *fit_rate* leaf (right), representing the distribution of the reconstructed rates for 2000 pseudo-datasets generated.

Let's now focus more in detail about the code structure of the *OutputManager* module. At the beginning we find three structs – Values, ValuesToy and ValuesParam – containing the output values to be later inserted in the proper ROOT TTree branches. Furthermore, as preliminary useful functions we have the template function vec2array, which converts a std::vector into an array and toCpdPerkton, broadly exploited in the following, which converts a results parameter vector from counts into cpd/kton.

Besides the trivial *OutputManager* constructor and destructor, the core of this module is formed by the functions described hereafter:

- OutputManager::initRootFile opens the ROOT file to be used to write the results in.
- OutputManager::closeRootFile closes the above-mentioned ROOT file.
- OutputManager::makePDFsSum initialises and fill the PDFsSum object, i.e. a std::vector⟨TH1D*⟩ variable to store the fit results, calculated as the sum bin per bin of all the PDFs, properly scaled by the fit.

- OutputManager::writeParamTree creates, fills and writes the *Parameters* and *Config* TTrees in the *parameters* folder.
- OutputManager::writeFitTree creates, fills and writes the *FitResults* TTree.
- OutputManager::writeToyTree creates, fills and writes the *ToyGeneration* TTree.
- OutputManager::fitToFile writes the output of one single fit to a text file.
- OutputManager::plotToFile writes the *Plot* canvas on the ROOT file.
- OutputManager::drawPDFs write the *PDFs* canvas where both the PDFs used for model and for data are plotted for comparison.

Lastly, we have the two similar functions ProcessResults, one to plot the results for one single fit while the second one dedicated to toy data fits. They distinguish from each other since the first one involves NuFitResults variables, while the second one the more complicated std::vector⟨NuFitResults⟩ ones. At the same time, they have a lot in common. Both of them simply call the functions mentioned above to create the output ROOT file, fill it with TTrees and plots, and create at the end the output text file.

Bibliography

[1] W. Pauli. *Letter to the "radioactives" in Tübingen, December 1930*. Cambridge Monogr. Part. Phys. Cosmol., 14:1, 2000.

[2] E. Fermi. "Versuch einer Theorie der β-Strahlen. I. (German) [Attempt at a theory of β-rays. I]". In: 88.3–4 (1934), pp. 161–177.

[3] J. Chadwick. "Possible Existence of a Neutron". In: *Nature* 129 (1932), p. 312. DOI: 10.1038/129312a0.

[4] B. Pontecorvo. "Neutrino Experiments and the Problem of Conservation of Leptonic Charge". In: *Zh. Eksp. Teor. Fiz.* 53 (1967), pp. 1717–1725.

[5] Steve Boyd. "Lecture notes on Neutrino Oscillations". In: (November 2020).

[6] Guido Fantini, Andrea Gallo Rosso, Francesco Vissani, and Vanessa Zema. *The formalism of neutrino oscillations: an introduction*. 2020. arXiv: 1802.05781 [hep-ph].

[7] P.A. Zyla et al. "Particle Data Group". In: *Prog. Theor. Exp. Phys. 2020* 083C01 (2020).

[8] L. Wolfenstein. "Neutrino oscillations in matter". In: *Phys. Rev. D* (May 1978). DOI: 10.1103/PhysRevD.17.2369.

[9] Christian Spiering. "Towards high-energy neutrino astronomy". In: *The European Physical Journal H* 37.3 (July 2012), pp. 515–565. ISSN: 2102-6467. DOI: 10.1140/epjh/e2012-30014-2. URL: http://dx.doi.org/10.1140/epjh/e2012-30014-2.

[10] M.G. Betti et al. "Neutrino physics with the PTOLEMY project: active neutrino properties and the light sterile case". In: *Journal of Cosmology and Astroparticle Physics* 2019.07 (July 2019). ISSN: 1475-7516. DOI: 10.1088/1475-7516/2019/07/047.

[11] A. A. Hahn, K. Schreckenbach, G. Colvin, B. Krusche, W. Gelletly, and F. Von Feilitzsch. "Anti-neutrino Spectra From ^{241}Pu and ^{239}Pu Thermal Neutron Fission Products". In: *Phys. Lett. B* 218 (1989), pp. 365–368. DOI: 10.1016/0370-2693(89)91598-0.

[12] F. Von Feilitzsch, A. A. Hahn, and K. Schreckenbach. "EXPERIMENTAL BETA SPECTRA FROM PU-239 AND U-235 THERMAL NEUTRON FISSION PRODUCTS AND THEIR CORRELATED ANTI-NEUTRINOS SPECTRA". In: *Phys. Lett. B* 118 (1982), pp. 162–166. DOI: 10.1016/0370-2693(82)90622-0.

[13] C. L. Cowan, F. Reines, F. B. Harrison, H. W. Kruse, and A. D. McGuire. "Detection of the free neutrino: A Confirmation". In: *Science* 124 (1956), pp. 103–104. DOI: 10.1126/science.124.3212.103.

[14] John N. Bahcall. *NEUTRINO ASTROPHYSICS*. 1989. ISBN: 978-0-521-37975-5.

[15] Aldo Serenelli. "Alive and well: A short review about standard solar models". In: *The European Physical Journal A* 52.4 (Apr. 2016). ISSN: 1434-601X. DOI: 10.1140/epja/i2016-16078-1. URL: http://dx.doi.org/10.1140/epja/i2016-16078-1.

[16] Núria Vinyoles, Aldo M. Serenelli, Francesco L. Villante, Sarbani Basu, Johannes Bergström, M. C. Gonzalez-Garcia, Michele Maltoni, Carlos Peña-Garay, and Ningqiang Song. "A New Generation of Standard Solar Models". In: *The Astrophysical Journal* 835.2 (Jan. 2017), p. 202. ISSN: 1538-4357. DOI: 10.3847/1538-4357/835/2/202.

[17] Aldo M. Serenelli, W. C. Haxton, and Carlos Peña-Garay. "SOLAR MODELS WITH ACCRETION. I. APPLICATION TO THE SOLAR ABUNDANCE PROBLEM". In: *The Astrophysical Journal* 743.1 (Nov. 2011), p. 24. ISSN: 1538-4357. DOI: 10.1088/0004-637x/743/1/24. URL: http://dx.doi.org/10.1088/0004-637X/743/1/24.

[18] W.C. Haxton, R.G. Hamish Robertson, and Aldo M. Serenelli. "Solar Neutrinos: Status and Prospects". In: *Annual Review of Astronomy and Astrophysics* 51.1 (Aug. 2013), pp. 21–61. ISSN: 1545-4282. DOI: 10.1146/annurev-astro-081811-125539.

[19] Sarbani Basu and H.M. Antia. "Helioseismology and solar abundances". In: *Physics Reports* 457.5–6 (Mar. 2008), pp. 217–283. ISSN: 0370-1573. DOI: 10.1016/j.physrep.2007.12.002. URL: http://dx.doi.org/10.1016/j.physrep.2007.12.002.

[20] Nicolas Grevesse and A. Jacques Sauval. "Standard Solar Composition". In: *Space Science Reviews* 85 (1998), pp. 161–174.

[21] Martin Asplund, Nicolas Grevesse, A. Jacques Sauval, and Pat Scott. "The Chemical Composition of the Sun". In: *Annual Review of Astronomy and Astrophysics* 47.1 (Sept. 2009), pp. 481–522. ISSN: 1545-4282. DOI: 10.1146/annurev.astro.46.060407.145222.

[22] H. A. Bethe. "Energy Production in Stars". In: *Phys. Rev.* 55 (5 Mar. 1939), pp. 434–456. DOI: 10.1103/PhysRev.55.434.

[23] Eric G. Adelberger et al. "Solar fusion cross sections". In: *Reviews of Modern Physics* 70.4 (Oct. 1998), pp. 1265–1291. ISSN: 1539-0756. DOI: 10.1103/revmodphys.70.1265.

[24] John N. Bahcall. "The luminosity constraint on solar neutrino fluxes". In: *Physical Review C* 65.2 (Jan. 2002). ISSN: 1089-490X. DOI: 10.1103/physrevc.65.025801.

[25] Raymond Davis, Don S. Harmer, and Kenneth C. Hoffman. "Search for Neutrinos from the Sun". In: *Phys. Rev. Lett.* 20 (21 May 1968), pp. 1205–1209. DOI: `10.1103/PhysRevLett.20.1205`.

[26] J. N. Abdurashitov et al. "Solar neutrino flux measurements by the Soviet-American Gallium Experiment (SAGE) for half the 22 year solar cycle". In: *J. Exp. Theor. Phys.* 95 (2002), pp. 181–193. DOI: `10.1134/1.1506424`. arXiv: `astro-ph/0204245`.

[27] W. Hampel et al. "GALLEX solar neutrino observations: Results for GALLEX IV". In: *Phys. Lett. B* 447 (1999), pp. 127–133. DOI: `10.1016/S0370-2693(98)01579-2`.

[28] M. Altmann et al. "GNO solar neutrino observations: results for GNO I". In: *Physics Letters B* 490.1-2 (Sept. 2000), pp. 16–26. ISSN: 0370-2693. DOI: `10.1016/s0370-2693(00)00915-1`.

[29] M. Altmann et al. "Complete results for five years of GNO solar neutrino observations". In: *Phys. Lett. B* 616 (2005), pp. 174–190. DOI: `10.1016/j.physletb.2005.04.068`. arXiv: `hep-ex/0504037`.

[30] Y. Fukuda et al. "Measurements of the Solar Neutrino Flux from Super-Kamiokande's First 300 Days". In: *Physical Review Letters* 81.6 (Aug. 1998), pp. 1158–1162. ISSN: 1079-7114. DOI: `10.1103/physrevlett.81.1158`.

[31] KS Hirata et al. "Real-time, directional measurement of 8B solar neutrinos in the Kamiokande II detector." In: *Physical review D: Particles and fields* 44 (Nov. 1991), pp. 2241–2260.

[32] Abe et al. "Measurement of θ_{13} in Double Chooz using neutron captures on hydrogen with novel background rejection techniques". In: *Journal of High Energy Physics* (Jan. 2016). ISSN: 1029-8479. DOI: `10.1007/jhep01(2016)163`.

[33] A. Bellerive, J.R. Klein, A.B. McDonald, A.J. Noble, and A.W.P. Poon. "The Sudbury Neutrino Observatory". In: *Nuclear Physics B* 908 (2016). Neutrino Oscillations: Celebrating the Nobel Prize in Physics 2015, pp. 30–51. ISSN: 0550-3213. DOI: `https://doi.org/10.1016/j.nuclphysb.2016.04.035`.

[34] Q. R. Ahmad et al. "Direct Evidence for Neutrino Flavor Transformation from Neutral-Current Interactions in the Sudbury Neutrino Observatory". In: *Phys. Rev. Lett.* 89 (1 June 2002), p. 011301. DOI: `10.1103/PhysRevLett.89.011301`.

[35] G. Alimonti et al. "The Borexino detector at the Laboratori Nazionali del Gran Sasso". In: *Nuclear Instruments and Methods in Physics Research Section A: Accelerators, Spectrometers, Detectors and Associated Equipment* 600.3 (Mar. 2009), pp. 568–593. ISSN: 0168-9002. DOI: `10.1016/j.nima.2008.11.076`.

[36] M. Agostini et al. "Comprehensive measurement of *pp*-chain solar neutrinos". In: *Nature* 562.7728 (2018), pp. 505–510. DOI: `10.1038/s41586-018-0624-y`.

[37] M. Agostini et al. "Experimental evidence of neutrinos produced in the CNO fusion cycle in the Sun". In: *Nature* 587.7835 (Nov. 2020), pp. 577–582. ISSN: 1476-4687. DOI: 10.1038/s41586-020-2934-0.

[38] Fengpeng An et al. "Neutrino physics with JUNO". In: *Journal of Physics G: Nuclear and Particle Physics* 43.3 (Feb. 2016), p. 030401. ISSN: 1361-6471. DOI: 10.1088/0954-3899/43/3/030401.

[39] "JUNO physics and detector". In: *Progress in Particle and Nuclear Physics* 123 (2022), p. 103927. ISSN: 0146-6410. DOI: https://doi.org/10.1016/j.ppnp.2021.103927.

[40] JUNO collaboration et al. "Feasibility and physics potential of detecting ^{8}B solar neutrinos at JUNO". In: (2020). arXiv: 2006.11760 [hep-ex].

[41] A. Gando et al. "Reactor on-off antineutrino measurement with KamLAND". In: *Phys. Rev. D* 88 (3 Aug. 2013), p. 033001. DOI: 10.1103/PhysRevD.88.033001.

[42] A. Gando et al. "Partial radiogenic heat model for Earth revealed by geoneutrino measurements". In: *Nature Geoscience* 4 (Aug. 2011), pp. 647–651. DOI: 10.1038/ngeo1205.

[43] T. Araki et al. "Experimental investigation of geologically produced antineutrinos with KamLAND". In: *Nature* 436 (2005), pp. 499–503. DOI: 10.1038/nature03980.

[44] G. Bellini et al. "Observation of geo-neutrinos". In: *Physics Letters B* 687.4 (2010), pp. 299–304. ISSN: 0370-2693. DOI: https://doi.org/10.1016/j.physletb.2010.03.051.

[45] G. Bellini et al. "Measurement of geo-neutrinos from 1353 days of Borexino". In: *Physics Letters B* 722.4 (2013), pp. 295–300. ISSN: 0370-2693. DOI: https://doi.org/10.1016/j.physletb.2013.04.030.

[46] M. Agostini et al. "Spectroscopy of geoneutrinos from 2056 days of Borexino data". In: *Phys. Rev. D* 92 (3 Aug. 2015), p. 031101. DOI: 10.1103/PhysRevD.92.031101. URL: https://link.aps.org/doi/10.1103/PhysRevD.92.031101.

[47] M. Agostini et al. "Comprehensive geoneutrino analysis with Borexino". In: *Phys. Rev. D* 101 (1 Jan. 2020), p. 012009. DOI: 10.1103/PhysRevD.101.012009. URL: https://link.aps.org/doi/10.1103/PhysRevD.101.012009.

[48] Jia-Shu Lu, Yu-Feng Li, and Shun Zhou. "Getting the most from the detection of Galactic supernova neutrinos in future large liquid-scintillator detectors". In: *Phys. Rev. D* 94 (2 July 2016), p. 023006. DOI: 10.1103/PhysRevD.94.023006.

[49] F.P. An et al. "The muon system of the Daya Bay Reactor antineutrino experiment". In: *Nuclear Instruments and Methods in Physics Research Section A: Accelerators, Spectrometers, Detectors and Associated Equipment* 773 (Feb. 2015), pp. 8–20. ISSN: 0168-9002. DOI: `10.1016/j.nima.2014.09.070`. URL: `http://dx.doi.org/10.1016/j.nima.2014.09.070`.

[50] N. Agafonova et al. "Final results on neutrino oscillation parameters from the OPERA experiment in the CNGS beam". In: *Physical Review D* 100.5 (Sept. 2019). ISSN: 2470-0029. DOI: `10.1103/physrevd.100.051301`. URL: `http://dx.doi.org/10.1103/PhysRevD.100.051301`.

[51] Hamamatsu Photonics K.K. *Photomultiplier tubes: Basics and applications*. 2007. URL: `https://www.hamamatsu.com/resources/pdf/etd/PMT_handbook_v3aE.pdf`.

[52] *Hamamatsu Photonics web page*. URL: `https://www.hamamatsu.com/`.

[53] Yifang Wang et al. "A new design of large area MCP-PMT for the next generation neutrino experiment". In: *Nucl. Instrum. Meth. A* 695 (2012). Ed. by Philippe Bourgeois, Bertrand Cordier, Agnès Dominjon, Houmani El Mamouni, Olivier Limousin, Patrick Nedelec, Stephane Normand, Antoine Penquer, Veronique Puill, and Jean-Charles Vanel, pp. 113–117. DOI: `10.1016/j.nima.2011.12.085`.

[54] *HZC Photonics web page*. URL: `http://www.hzcphotonics.com/`.

[55] Glenn F. Knoll. *Radiation Detection and Measurement, 3rd ed.* 3rd edition. New York: John Wiley and Sons, 2000. ISBN: 978-0-471-07338-3, 978-0-471-07338-3.

[56] Daya Bay et al. *Optimization of the JUNO liquid scintillator composition using a Daya Bay antineutrino detector*. 2020. arXiv: `2007.00314 [physics.ins-det]`.

[57] P. Lombardi et al. "Distillation and stripping pilot plants for the JUNO neutrino detector: Design, operations and reliability". In: *Nuclear Instruments and Methods in Physics Research Section A: Accelerators, Spectrometers, Detectors and Associated Equipment* 925 (May 2019), pp. 6–17. ISSN: 0168-9002. DOI: `10.1016/j.nima.2019.01.071`. URL: `http://dx.doi.org/10.1016/j.nima.2019.01.071`.

[58] G. von Bünau. "J. B. Birks: Photophysics of Aromatic Molecules. Wiley-Interscience, London 1970. 704 Seiten. Preis: 210s". In: 1970.

[59] Angel Abusleme et al. "Radioactivity control strategy for the JUNO detector". In: *JHEP* 11 (2021), p. 102. DOI: `10.1007/JHEP11(2021)102`. arXiv: `2107.03669 [physics.ins-det]`.

[60] D. Basilico, Ferraro F. B. Caccianiga, Meraviglia A., Re A., Goettel A., Ludhova L., Singhal A., Pelicci L., and Settanta G. *JUNO sensitivity to intermediate energy solar neutrinos, ^{7}Be,* pep, *and CNO: results of the two independent analysis performed by Milano and Juelich.* JUNO internal note.

[61] G. Bellini et al. “Final results of Borexino Phase-I on low-energy solar neutrino spectroscopy”. In: *Physical Review D* 89.11 (June 2014). ISSN: 1550-2368. DOI: `10.1103/physrevd.89.112007`.

[62] S. Abe et al. “Production of radioactive isotopes through cosmic muon spallation in KamLAND”. In: *Physical Review C* 81.2 (Feb. 2010). ISSN: 1089-490X. DOI: `10.1103/physrevc.81.025807`. URL: `http://dx.doi.org/10.1103/PhysRevC.81.025807`.

[63] G Bellini et al. “Cosmogenic Backgrounds in Borexino at 3800 m water-equivalent depth”. In: *Journal of Cosmology and Astroparticle Physics* 2013.08 (Aug. 2013), pp. 049–049. ISSN: 1475-7516. DOI: `10.1088/1475-7516/2013/08/049`. URL: `http://dx.doi.org/10.1088/1475-7516/2013/08/049`.

[64] M. Agostini et al. “Improved measurement of B8 solar neutrinos with 1.5kty of Borexino exposure”. In: *Physical Review D* 101.6 (Mar. 2020). ISSN: 2470-0029. DOI: `10.1103/physrevd.101.062001`. URL: `http://dx.doi.org/10.1103/PhysRevD.101.062001`.

[65] M. Agostini et al. “Identification of the cosmogenic ^{11}C background in large volumes of liquid scintillators with Borexino”. In: *The European Physical Journal C* 81.12 (Dec. 2021). ISSN: 1434-6052. DOI: `10.1140/epjc/s10052-021-09799-x`. URL: `http://dx.doi.org/10.1140/epjc/s10052-021-09799-x`.

[66] V. I. Kopeikin. “Flux and spectrum of reactor antineutrinos”. In: *Physics of Atomic Nuclei* 75.2 (Feb. 2012), pp. 143–152. DOI: `10.1134/S1063778812020123`.

[67] A. Savitzky and M. J. E. Golay. “Smoothing and differentiation of data by simplified least squares procedures”. In: *Analytical Chemistry* 36 (Jan. 1964), pp. 1627–1639.

[68] J. Zou, Xiang-Jie Huang, W.D. Li, Tao Lin, T. Li, Kiki Zhang, Z. Deng, and G. Cao. “SNiPER: an offline software framework for non-collider physics experiments”. In: *Journal of Physics: Conference Series* 664 (Dec. 2015), p. 072053. DOI: `10.1088/1742-6596/664/7/072053`.

[69] S. Agostinelli et al. “Geant4—a simulation toolkit”. In: *Nuclear Instruments and Methods in Physics Research Section A: Accelerators, Spectrometers, Detectors and Associated Equipment* 506.3 (2003), pp. 250–303. ISSN: 0168-9002. DOI: `https://doi.org/10.1016/S0168-9002(03)01368-8`.

[70] Rene Brun and Fons Rademakers. “ROOT — An object oriented data analysis framework”. In: *Nuclear Instruments and Methods in Physics Research Section A: Accelerators, Spectrometers, Detectors and Associated Equipment* 389.1 (1997), pp. 81–86. ISSN: 0168-9002. DOI: `https://doi.org/10.1016/S0168-9002(97)00048-X`.

[71] W. Wu, M. He, X. Zhou, and H. Qiao. “A new method of energy reconstruction for large spherical liquid scintillator detectors”. In: *Journal of Instrumentation* 14.03 (Mar. 2019), P03009–P03009. ISSN: 1748-0221. DOI: `10.1088/1748-0221/14/03/p03009`. URL: `http://dx.doi.org/10.1088/1748-0221/14/03/P03009`.

[72] Y. Zhang, Z.Y. Yu, X.Y. Li, Z.Y. Deng, and L.J. Wen. “A complete optical model for liquid-scintillator detectors”. In: *Nuclear Instruments and Methods in Physics Research Section A: Accelerators, Spectrometers, Detectors and Associated Equipment* 967 (July 2020), p. 163860. ISSN: 0168-9002. DOI: `10.1016/j.nima.2020.163860`. URL: `http://dx.doi.org/10.1016/j.nima.2020.163860`.

[73] Q. Liu, M. He, X. Ding, W. Li, and H. Peng. “A vertex reconstruction algorithm in the central detector of JUNO”. In: *Journal of Instrumentation* 13.09 (Sept. 2018), T09005–T09005. ISSN: 1748-0221. DOI: `10.1088/1748-0221/13/09/t09005`. URL: `http://dx.doi.org/10.1088/1748-0221/13/09/T09005`.

[74] H. Rebber, L. Ludhova, B. Wonsak, and Y. Xu. “Particle identification at MeV energies in JUNO”. In: *Journal of Instrumentation* 16.01 (Jan. 2021), P01016–P01016. ISSN: 1748-0221. DOI: `10.1088/1748-0221/16/01/p01016`. URL: `http://dx.doi.org/10.1088/1748-0221/16/01/P01016`.

[75] URL: `https://github.com/davidebasilico/MUST`.

[76] X.F. Ding. “GooStats: A GPU-based framework for multi-variate analysis in particle physics”. In: *Journal of Instrumentation* 13.12 (Dec. 2018), P12018–P12018. ISSN: 1748-0221. DOI: `10.1088/1748-0221/13/12/p12018`. URL: `http://dx.doi.org/10.1088/1748-0221/13/12/P12018`.

[77] Davide Basilico. *JUNO sensitivity studies with MUST*. 2020. URL: `https://www.overleaf.com/project/5fd3a4c6664c0172488eb742`.

[78] A. Göttel, L. Ludhova, A. Meraviglia, L. Pelicci, and G. Settanta. “JUST: A neutrino fit software for JUNO’s solar analysis and sensitivity”. In: Bologna: Il Nuovo Cimento, SIF, 2021.

[79] Fred James and Matthias Winkler. *MINUIT User’s Guide*. June 2004.

[80] Steve Baker and Robert D. Cousins. “Clarification of the Use of Chi Square and Likelihood Functions in Fits to Histograms”. In: *Nucl. Instrum. Meth.* 221 (1984), pp. 437–442. DOI: `10.1016/0167-5087(84)90016-4`.

Acknowledgments

Generally, I have some allergies to public announcements. However, at the same time, come to the end of this journey, I feel so grateful to the people I share it with, that I cannot skip this section.

First and foremost, my deepest thanks go to my supervisors Barbara, Ale and Davide for their irreplaceable guidance and contagious enthusiasm for science. In particular, I am indebted to Davide for his high level of patience in always answering even my silly questions, no matter the time. Staying on the Third Floor, I would also like to thank Fede and Marco, loyal deadlines' mate.

If the past year was exceptionally challenging and meaningful, this is also due to the months I spent in Germany. Therefore, I am grateful to my external supervisor Livia for warmly welcoming me in her group and further motivated me in my work. In this regard, a global thanks to all the Jülich people, especially the ones I worked with the most. So thanks to Alex for patiently taking care of my work, day-by-day; thanks to Apeksha for her kind helpfulness; thanks to Luca and Giulio for their constant support and their (car, dinner, beer)-sharing. Furthermore, a special thanks to Mariam for a unique friendship built on a single face-to-face meeting and tons of hilarious online conversations.

When thinking about these last few years, there are still some people I cannot omit. People I shared with my everyday life or *just* precious moments.

Thanks to Elena, a guiding light during most of my exams, and to Enrico for our lunchtime bickering at the Physics Dept.

Thanks to Mauro for our never-ending talks during our under-equipped hikings.

Thanks to my wild and swinger friends Ele and Natan for being an endless source of inspiration.

Thanks to Jorge for bringing mindfulness *chivitos* into my life and for all we shared in the North European rainy lands. Also, thank you for still being here.

Thanks to my dearest friend Susy, for always pushing me during my darkest times and for a thousand things I cannot exhaust in a few lines.

Finally, thanks to my family. In particular, to *nonna* for measuring love in calories, to my sister Irene, more than you imagine, and to my parents for having allowed me to make every step of this path.